Chapter 5
The Orbiters

William A. Imbriale, Mark S. Gatti, and Roberto Mizzoni

After planetary flybys, the next great quest in Solar System exploration was to put a spacecraft in orbit about each of the planets. The purpose of this effort was to enable long-term climatic studies and gravity-field and surface mapping. Mariner 9, the very first orbiter, arrived at Mars in November 1971. Magellan arrived at Venus in August 1990, Galileo at Jupiter in December 1995, and Cassini at Saturn in July 2004. This chapter describes these three non-Mars orbital missions. (Mars orbiters are discussed in Chapter 4.)

5.1 Magellan to Venus
William A. Imbriale

In the latter part of 1972, the Jet Propulsion Laboratory (JPL) began the concept studies of a radar-imaging mission to map the Venusian surface [1]. Due to uncertainty about funding in the Advanced Studies Program and the mission's role and rationale, a decision was made to conduct the study in two parts: a science and mission activity first, and a spacecraft system activity later. The project was named Venus Orbiting Imaging Radar (VOIR), and science investigators were selected in 1979.

Hughes Aircraft Company was selected to conduct the design development of the VOIR, scheduled to launch in 1983. However, complex cost estimates due to considerable science input from non-NASA, non-JPL scientists through consultants, informal work, and contractor science steering groups created an expensive complex spacecraft. Consequently, VOIR was deemed too costly and was cancelled in 1982.

However, in October 1983, the Venus mission was reinstated as a National Aeronautics and Space Administration (NASA) budgetary new start and named the Venus Radar Mapper (VRM). The new mission was a reduced undertaking that eliminated all experiments except the gravity-field experiment and the synthetic-aperture radar (SAR), which included imaging, altimetry, and radiometry. Also, to accommodate a reinstatement provision of reduced funding, the spacecraft would be built for about half the originally estimated cost. VRM used mission-proven technologies and spare components from other flight programs, such as Voyager, Galileo, and Ulysses. VRM was officially renamed Magellan in 1986, after the Sixteenth Century Portuguese explorer who first circumnavigated the Earth by sea.

Thus, with a scaled-down experiment package and with other compromises, such as the use of an elliptical orbit rather than the circular one planned for, the Venus mission was on track again, with a launch planned for May 1988. Magellan's simpler design also meant that some components had to perform more complex tasks than they had originally been designed for. For example, instead of using separate antennas for mapping and telemetry, the primary antenna would perform both of these functions.

The loss of the Space Shuttle Challenger in 1986 and the 32-month suspension of Shuttle missions delayed and reshuffled many planned space activities, including Magellan. One factor that influenced Magellan's launch date was the cancellation of the Centaur G-Prime booster as cargo on the Space Shuttle. (The Centaur had the most powerful upper stage ever designed. Its explosive liquid-oxygen and liquid-hydrogen propellants, however, were deemed too dangerous to carry along with humans into space). A second factor was the scheduled launch of the Galileo mission to Jupiter, set for October 1989—the date initially set for Magellan. A third factor was the alignment of the planets, which added a two-year delay to Magellan's launch date.

Therefore, the U.S. Air Force's less-powerful Inertial Upper Stage (IUS) replaced Centaur as the booster for Magellan; this required some modification of the spacecraft design and mission plans. The result for Magellan was that its earliest launch would be May 1989 with the use of a Type-IV trajectory. This meant that the spacecraft would spend 15 months traveling one-and-a-half times around the Sun before arriving at Venus. The original May 1988 launch date would have allowed Magellan to reach Venus in 4 months by traveling less than 180 degrees around the Sun on a Type-I trajectory.

The $551-million Magellan was the first planetary spacecraft to be launched by a Space Shuttle; the Atlantis carried it aloft from Kennedy Space Center in Florida on May 4, 1989. Atlantis took Magellan into low-Earth orbit, where it was released from the Shuttle's cargo bay. The solid-fuel IUS then fired, sending Magellan on a 15-month cruise before it arrived at Venus on August 10, 1990. A solid-fuel motor on Magellan then fired, placing the spacecraft in orbit around Venus. Magellan's initial orbit was highly elliptical,

taking it as close as 294 km (182 mi) from Venus and as far away as 8,543 km (5, 296 mi). The orbit was polar, meaning that the spacecraft moved from south to north or vice versa during each looping pass, flying over Venus' north and south poles. Magellan completed one orbit every 3 hours and 15 minutes.

During the part of its orbit closest to Venus, Magellan's radar mapper imaged a swath of the planet's surface approximately 17 to 28 km (10 to 17 mi) wide. At the end of each orbit, the spacecraft radioed back to Earth a map of a long, ribbon-like strip of the planet's surface captured on that orbit. Venus itself rotates once every 243 Earth days. As the planet rotated under the spacecraft, Magellan collected strip after strip of radar image data, eventually covering the entire globe at the end of the 243-day orbital cycle.

By the end of its first such 8-month orbital cycle between September 1990 and May 1991, Magellan had sent to Earth detailed images of 84 percent of the Venusian surface. The spacecraft then conducted radar mapping on two more 8-month cycles, from May 1991 to September 1992. This allowed it to capture detailed maps of 98 percent of the planet's surface. The follow-on cycles also allowed scientists to look for any changes in the surface from one year to the next. In addition, because the "look angle" of the radar was slightly different from one cycle to the next, scientists could construct three-dimensional views of the Venusian surface.

During Magellan's fourth 8-month orbital cycle at Venus from September 1992 to May 1993, the spacecraft collected data on the planet's gravity field. During this cycle, Magellan did not use its radar mapper but instead transmitted a constant radio signal to Earth. If it passed over an area of Venus with higher than normal gravity, the spacecraft would slightly speed up in its orbit. This would cause the frequency of Magellan's radio signal to change very slightly due to the Doppler effect—much like the pitch of a siren changes as an ambulance passes. Thanks to the ability of radio receivers in the NASA/JPL Deep Space Network (DSN) to measure frequencies extremely accurately, scientists were able to accumulate a detailed gravity map of Venus.

At the end of Magellan's fourth orbital cycle in May 1993, flight controllers lowered the spacecraft's orbit using a then-untried technique called aerobraking. This maneuver sent Magellan dipping into Venus's atmosphere once every orbit; the atmospheric drag on the spacecraft slowed down Magellan and lowered its orbit. After the aerobraking was completed between May 25 and August 3, 1993, Magellan's orbit then took it as close as 180 km (112 mi) from Venus and as far away as 541 km (336 mi). Magellan also circled Venus more quickly, completing an orbit once every 94 minutes. This new, more circularized orbit allowed Magellan to collect better gravity data in the higher northern and southern latitudes near the Venusian poles.

After the end of that fifth orbital cycle in April 1994, Magellan began a sixth and final orbital cycle, collecting more gravity data and conducting radar

and radio science experiments. By the end of the mission, Magellan captured high-resolution gravity data for about 95 percent of the planet's surface.

In September 1994, Magellan's orbit was lowered once more in another test called a "windmill experiment." In this test, the spacecraft's solar panels were turned to a configuration resembling the blades of a windmill, and Magellan's orbit was lowered into the thin outer reaches of Venus's dense atmosphere. Flight controllers then measured the amount of torque control required to maintain Magellan's orientation and keep it from spinning. This experiment gave scientists data on the behavior of molecules in the Venusian upper atmosphere, and lent engineers new information useful in designing spacecraft.

On October 11, 1994, Magellan's orbit was lowered a final time, causing the spacecraft to become caught in the atmosphere and plunge to the surface; contact was lost the following day. Although much of Magellan was believed to have vaporized, some sections probably hit the planet's surface intact.

5.1.1   The Magellan Spacecraft

Built partially with spare parts from other missions, the Magellan spacecraft was 4.6 m (15.4 ft) long, topped with a 3.7-m (12-ft) high-gain antenna (HGA) (see Fig. 5-1). Mated to its retrorocket and fully tanked with propellants, the spacecraft weighed a total of 3,460 kg (7,612 lb) at launch.

The HGA, used for both communication and radar imaging, was a spare from the Voyager mission to the outer planets, as were Magellan's 10-sided main structure and a set of thrusters. The command data computer system, attitude control computer, and power distribution units were spares from the Galileo mission to Jupiter. Martin Marietta Corporation was the primary subcontractor for the Magellan spacecraft, while Hughes Aircraft Company was
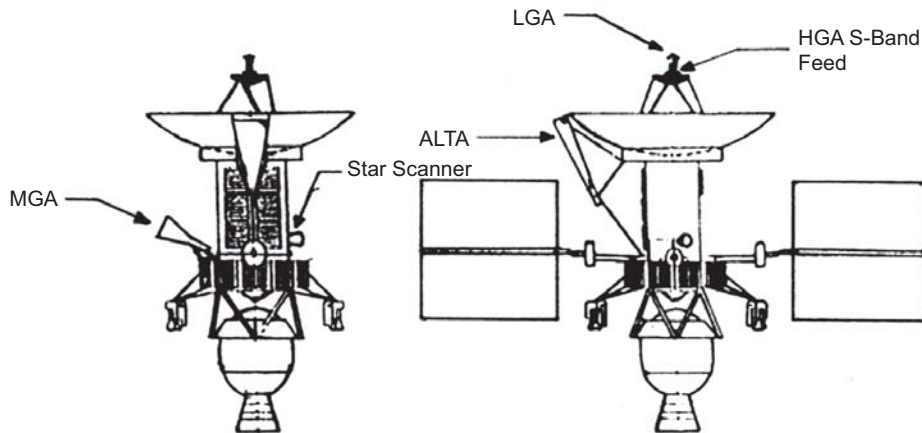

Fig. 5-1. Magellan spacecraft (ALTA = altimeter antenna, HGA = high-gain antenna, MGA = medium-gain antenna).

the primary subcontractor for the radar system. The altimeter antenna was designed and built by Hughes Aircraft Company and is described in detail in the following section.

Magellan was powered by two square solar panels, each measuring 2.5 m (8.2 ft) on a side; together they supplied 1,200 W of power. Over the course of the mission, the solar panels gradually degraded, as expected. By the end of the mission in the fall of 1994, it was necessary to manage power usage carefully to keep the spacecraft operating.

Because a dense, opaque atmosphere shrouds Venus, conventional optical cameras could not be used to image its surface. Instead, Magellan's imaging radar used bursts of microwave energy somewhat like a camera flash to illuminate the planet's surface.

Magellan's HGA sent out millions of pulses each second toward the planet; the antenna then collected the echoes returned to the spacecraft when the radar pulses bounced off the Venus surface. Because the radar pulses were not sent directly downward but rather at a slight angle to the side of the spacecraft, it was sometimes called "side-looking radar." In addition, special processing techniques were used on the radar data to result in higher resolution as if the radar had a larger antenna, or "aperture." The technique is known as synthetic aperture radar, or SAR [2].

NASA first used SAR on JPL's Seasat oceanographic satellite in 1978; it was later developed more extensively for the Spaceborne Imaging Radar (SIR) missions on the Space Shuttle in 1981, 1984, and 1994.

Besides imaging, Magellan's radar system was also used to collect altimetry data showing the elevations of various surface features. In this mode, pulses were sent directly downward (from the altimeter antenna), and Magellan measured the time required for a radar pulse to reach Venus and return in order to determine the distance between the spacecraft and the planet.

5.1.2   The High-Gain Antenna Subsystem

Magellan's HGA/low-gain antenna (LGA) was a spare from the Voyager spacecraft; it is described in detail in Chapter 3. However, the mounts for the S-band feed and the LGA were redesigned for radar and communications use. There was also some cabling redesign because of the higher power requirements for the radar [3].

In addition to transmitting 2298 megahertz (MHz) and receiving 2115 MHz, the S-band feed also needed to transmit and receive the 2385-MHz radar frequency. The polarization was linear. The S-band feed was essentially a 3.6-in. (9.1-cm) inner-diameter open-ended waveguide surrounded by an 8.8-in. diameter (22.4-cm) cup 4.05 in. (10.3 cm) deep, as shown in Fig. 5-2.

Fig. 5-2. Magellan S-band feed.

5.1.3   The Medium-Gain Antenna

The medium-gain antenna (MGA) [4] was required to transmit 2298 ±5 MHz, with a peak gain of 19.0 decibels referenced to an isotropic radiator (dBi) and receive 2116 ±5 MHz, with a peak gain of 18.5 dBi. The polarization was right-hand circular polarization (RHCP) with an axial ratio of less than 2 dB over the 3-dB beamwidth. The antenna was mounted on the spacecraft bus in the x–y plane and pointed nominally at 70 deg body cone angle and 270 deg body clock angle. It was decided to use the Mariner 9 spare MGA, which was a conical horn antenna. However, the Mariner 9 horn diameter was 14 in. (36 cm) while an approximately 18.5-in. (47-cm) diameter was required to meet the gain specification. Therefore, the Mariner 9 MGA was modified with a cone extension (see Fig. 5-3), and thereby met all the performance requirements.
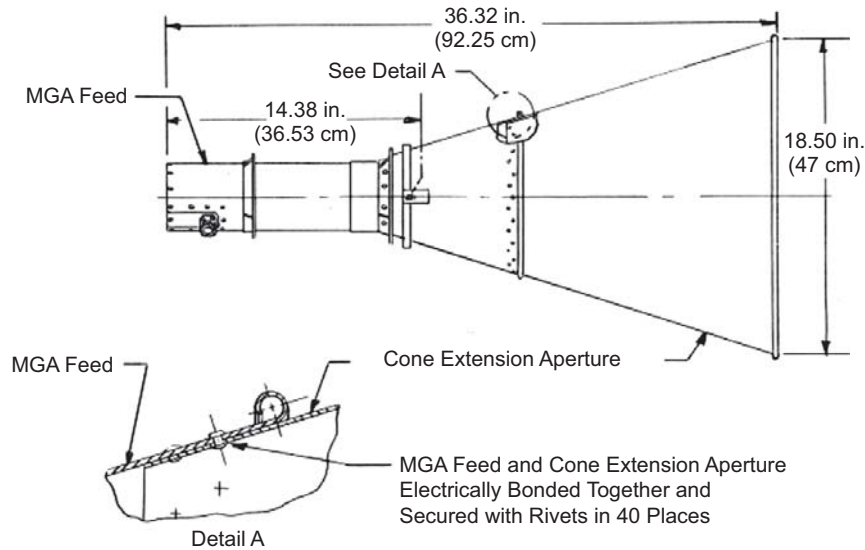
Fig. 5-3. Magellan medium-gain antenna.

5.1.4   The Magellan Altimeter Antenna

The altimeter antenna (ALTA) subsystem radiated the high-power-altimeter burst generated by the sensor subsystem transmitter. It also received the altimeter-burst echo and transmitted it to the sensor subsystem receiver [5].

The ALTA provided a peak gain of at least 18.5 dB and a 3-dB beamwidth of not less than 30 by 10 deg. The antenna was mounted alongside the HGA, as shown in Fig. 5-1. Its boresight was offset 25 deg relative to that of the HGA. The broad beamwidth of the ALTA radiation pattern was in the plane of the boresight axis of the HGA. During the sensor data collection portion of the mission, the ALTA was pointed to the approximate subsatellite point, while the HGA was looking toward the side of the planet to provide the synthetic aperture data processing capability.

The ALTA consisted of two basic elements: the horn and the waveguide transition. The horn provided the rectangular aperture that shaped the wavefront of the microwave signal and determined the directivity and beamwidths of the radiation pattern. The waveguide transition element transformed the microwave signal transmitted by a coaxial cable into a waveguide propagating waveform. It excited the waveguide in the appropriate mode to radiate a polarized signal in a plane parallel to the large dimension of the rectangular aperture. This plane contained the smallest beamwidth pattern.

The requirements for the ALTA, including expected performance, are summarized in Table 5-1. In all cases, the specified requirements were exceeded.

Table 5-1. Magellan altimeter antenna requirements summary.

Parameter	Required	Expected
Frequency	2385 MHz ±5 MHz	2385 MHz
Peak gain	18.5 dBi, absolute	19.6 dB (est losses)
Beamwidth, E-plane	10 deg min (3 dB)	11.0 deg (theoretical)
Beamwidth, H-plane	30 deg min (3 dB)	31.1 deg (theoretical)
Polarization	Linear—parallel to aperture large dimension	Linear
Cross polarization	–20 dB over 3 dB beamwidth	–24 dB (est)
Gain at 25 deg off boresight in H-plane	13 dBi max	11.5 dB (theoretical)
Input connection	TNC (female on antenna)	TNC
VSWR	1.2:1 max	1.2:1
Electrical-to-mechanical boresight error	±0.25 deg max	±0.10 deg (est)
Gain calibration error	≤0.3 dB relative, ≤0.5 dB absolute	≤0.3 dB relative, ≤0.5 dB absolute
Size	Less than 80 × 165 × 34 cm envelope	60.9 × 26.7 × 130.9 cm
Aperture cover	Not removed for flight	0.005-in. (0.01-cm) kapton with germanium coat
Power handling	320 W peak, 3.2 W average	≥4 dB above required

5.1.4.1 Electrical Design. Consideration of sidelobe levels in the E-plane of a standard horn design, particularly in an environment of potential excitation of an adjacent antenna, led to the selection of a trifurcated horn (Fig. 5-4). A trifurcated horn is one that divides the E-plane dimension of the aperture into three sections. This is done via conducting plates that convert the horn from a single large aperture to a central aperture and two adjacent radiating sections. These other sections are of the same H-plane dimensions as the central unit. The amplitude and phase of these outer radiating horn sections can be used to improve pattern shapes in the E-plane. Typically, a small percentage of the power is coupled from the input waveguide and throat geometry of the horn to the outer sections. Since in this case the "a" dimension of the horn is the same for all three-aperture illumination horn divisions, the phases for the three sections are nearly identical. A small phase difference of 6 deg was predicted in the ALTA design.

The gaps created near the throat of the horn controlled the percentage power split. The computed patterns assumed gaps that were adjusted to provide
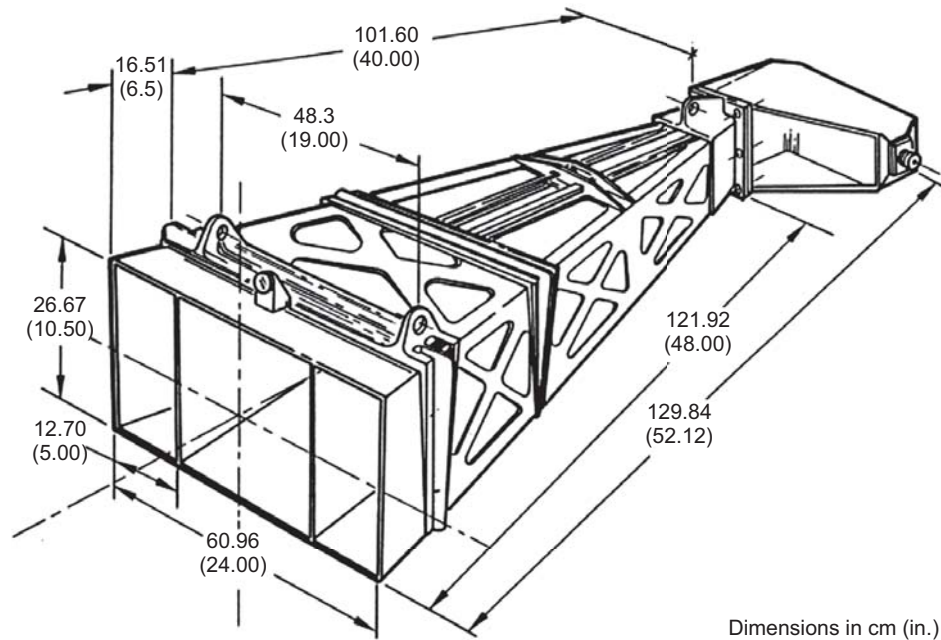
16.51
(6.5)

101.60
(40.00)

48.3
(19.00)

26.67
(10.50)

12.70
(5.00)

121.92
(48.00)

129.84
(52.12)

60.96
(24.00)

Dimensions in cm (in.)

Fig. 5-4. Magellan altimeter antenna (ALTA).

both outer sections of the horn at 16 percent power, leaving 68 percent power for the center. In addition to power and phase, the relative percent of the physical aperture assigned to the outer sections could be varied to optimize antenna pattern shape and gain.

An additional advantage of the trifurcated horn, as compared to standard horns of large size and area, is structural integrity. The septa dividing the horn into three sections provides inherent means of making the horn very strong and less susceptible to motion or distortion of the large areas of the horns.

Since very low sidelobes (i.e., larger than 20 dB below the peak of the beam) are not a specification requirement of this horn, there was considerable freedom in the selection of aperture dimensions, relative power and phase distributions, and horn length.

Figure 5-4 shows the dimensions of the Magellan trifurcated horn mode, which generated the gain and radiation patterns shown in Fig. 5-5 and cited in Table 5-1.

There are two types of coaxial line to waveguide probes: (a) capacitive and (b) inductive. There are advantages and disadvantages to each. The main advantage of the inductive type, which was selected for the ALTA, is the use of a probe that is rigidly attached to the broad wall of the transition waveguide assembly. This makes the unit a very structurally strong device. Also, the
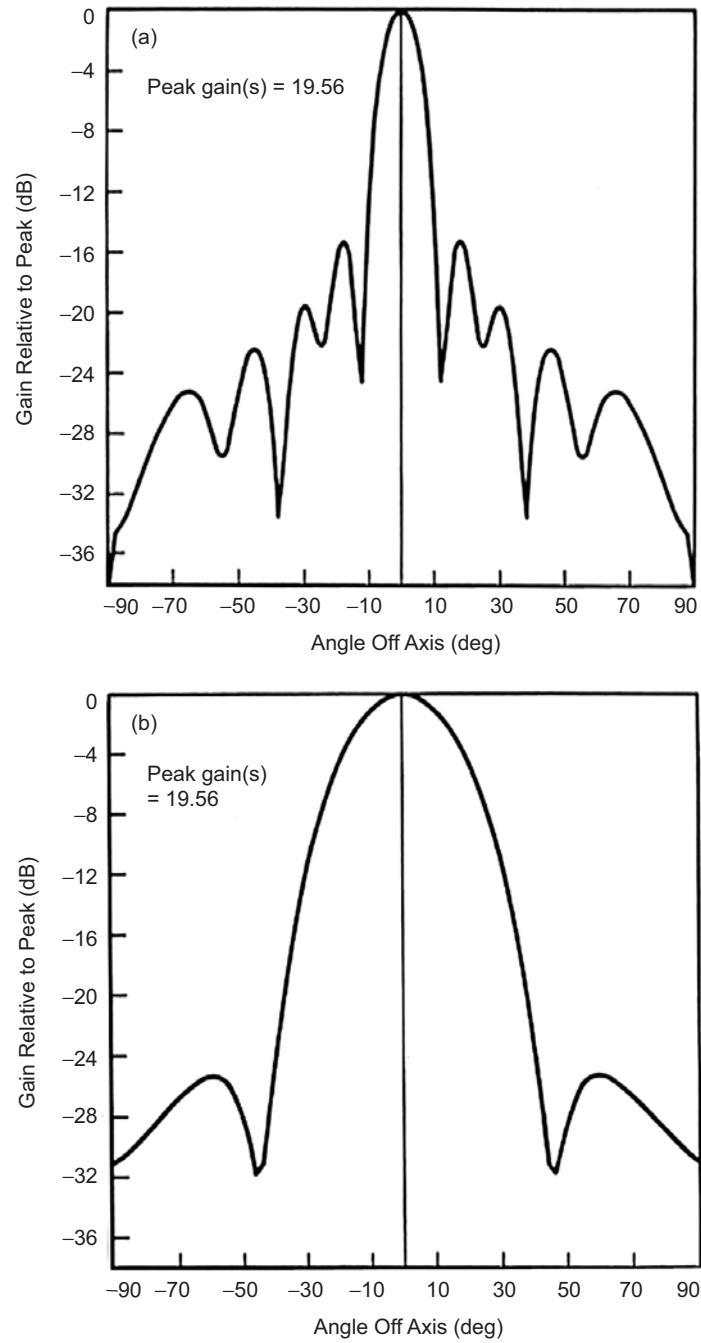
**Fig. 5-5. Magellan altimeter antenna radiation patterns
in (a) E-plane and (b) H-plane.**

inductive probe can use physical geometries that lead to low input voltage standing wave ratio (VSWR) without need for extensive tuning screws and/or encapsulating dielectric. Thus, it is easier to design for handling high power with low probability of multipactor breakdown. To set up the proper node excitation in the waveguide requires the inductive probe to be located in the back (i.e., short circuit) wall of the transition. Since mechanically it is more desirable to place the RF connector on the side of the horn, the transition incorporates a right angle. Careful attention was given to shape the transition so no sharp edges and tuning elements would compromise its power handling.

5.1.4.2 Mechanical Design. The ALTA (shown in Fig. 5-4) consisted of three major components: horn, transition, and connector. The transition and horn were aluminum, fabricated specifically for the mission, while the connector was an off-the-shelf item.

The transition section was made of a thin-walled aluminum housing and flange. Attached to the exterior was the threaded Neill-Concelman (TNC) connector. A dielectric disk was inserted between the conductor joining the connector and the inductive probe to avoid multipacting. The probe was machined aluminum, mounted inside the transition housing.

The horn consisted of four pieces of aluminum, plate cut and machined for the walls of the horn. Machining was required for weight savings. The thinner sections were 0.030 in. (0.8 mm) thick while the stiffeners were 0.055 in. (1.4 mm) thick. There were three mounting flanges, each containing a self-aligning bearing. This bearing design was rated for 8150-lb (3705-kg) radial and 700-lb (276-kg) axial static unit loads. The two septa, which divided the horn aperture into three rectangular sections, were 0.030-in. thick (0.8-mm) aluminum plates extending 36 in. (91.4 cm) into the horn. The flange of the horn contained one of the mounting flanges and a sleeve that slipped onto the horn. All components of the horn were joined by electron beam welding or dip brazing.

The ALTA weight was specified to be less than or equal to 7 kg (15.4 lb). The machined aluminum antenna weight was 4.54 kg (10 lb).

5.2 The Galileo Antenna System
Mark S. Gatti

Planning for the Galileo mission started almost immediately after the launch of the Voyager spacecraft. Galileo's mission was to place a spacecraft in orbit around Jupiter after the successful Voyager flybys, equipped with the most advanced telecommunications system yet flown on a deep-space mission. The telecommunications system would operate at X-band with 134.4 kilobits per second (kbps) and would require the use of an HGA that was the largest flown of any deep-space mission [6]. As with Voyager, Galileo would operate

at both S- and X-band. Unlike Voyager, however, X-band would be the prime operating frequency for this mission. The telecommunications system would require an LGA for near-Earth and emergency communications. The Space Shuttle would provide the launch, while the direct-to-Jupiter interplanetary trajectory would use the Centaur upper stage. Finally, the Galileo Probe mission, carrying a payload of science instruments, was to relay its signals through the orbiter via an L-band communications system.

In the late 1970s, the typical telemetry antennas used in deep-space missions were solid reflectors ranging in size from 1 m to 3.66 ms [7]. However, due to the growing need for increased data rates, higher antenna gain was required. As a result, during the planning for the mission telecommunications system, much activity was undertaken to determine the most cost effective, reliable, deployable antenna system that could support the Galileo mission [8–10]. After some effort, the "radial-rib" antenna developed by Harris Corporation for the Tracking and Data Relay Satellite System (TDRSS) spacecraft antenna [11] was selected for development to meet Galileo mission requirements.

Between 1981 and 1985, the Galileo antenna system, consisting of the high-gain system and a coaxially mounted low-gain antenna were designed, developed, fabricated, tested, and delivered to the Galileo Project. It was at the end of this period that the Shuttle Challenger was lost during launch with all aboard. Subsequent investigation and return-to-service of the Shuttle fleet required several years, during which it was determined the Centaur upper stage did not meet safety requirements for transport aboard the Shuttle. Instead, the U.S. Air Force Inertial Upper Stage (IUS) was selected for the injection into the interplanetary trajectory between the Earth and Jupiter. As a result of the inability for the IUS to support a direct-to-Jupiter trajectory, the spacecraft would now require the assistance of the planetary gravity of both Venus and the Earth. This trajectory is depicted in Fig. 5-6. The most obvious result of this trajectory is that it required the spacecraft to fly closer to the Sun than it would on a direct trajectory to Jupiter. Many of the systems on the spacecraft had to be redesigned and/or retrofitted in order to survive in the new solar environment. The most significant redesign for the antenna system was the addition of a sunshield mounted on the tip of the central tower structure, behind which the stowed HGA would remain until it was safe to deploy. Since the HGA was designed to be no closer than 0.98 astronomical units (AU) from the Sun, it would be several years after launch before deployment. Furthermore, other Galileo systems required shade from the Sun, provided by a large sunshield below the HGA. For all of the sunshields to perform properly, the spacecraft HGA/LGA axis had to be continuously Sun-pointed. As a result, there were many times in the mission where Earth would be in the aft-facing direction of the spacecraft. In order to maintain communications during these (long)
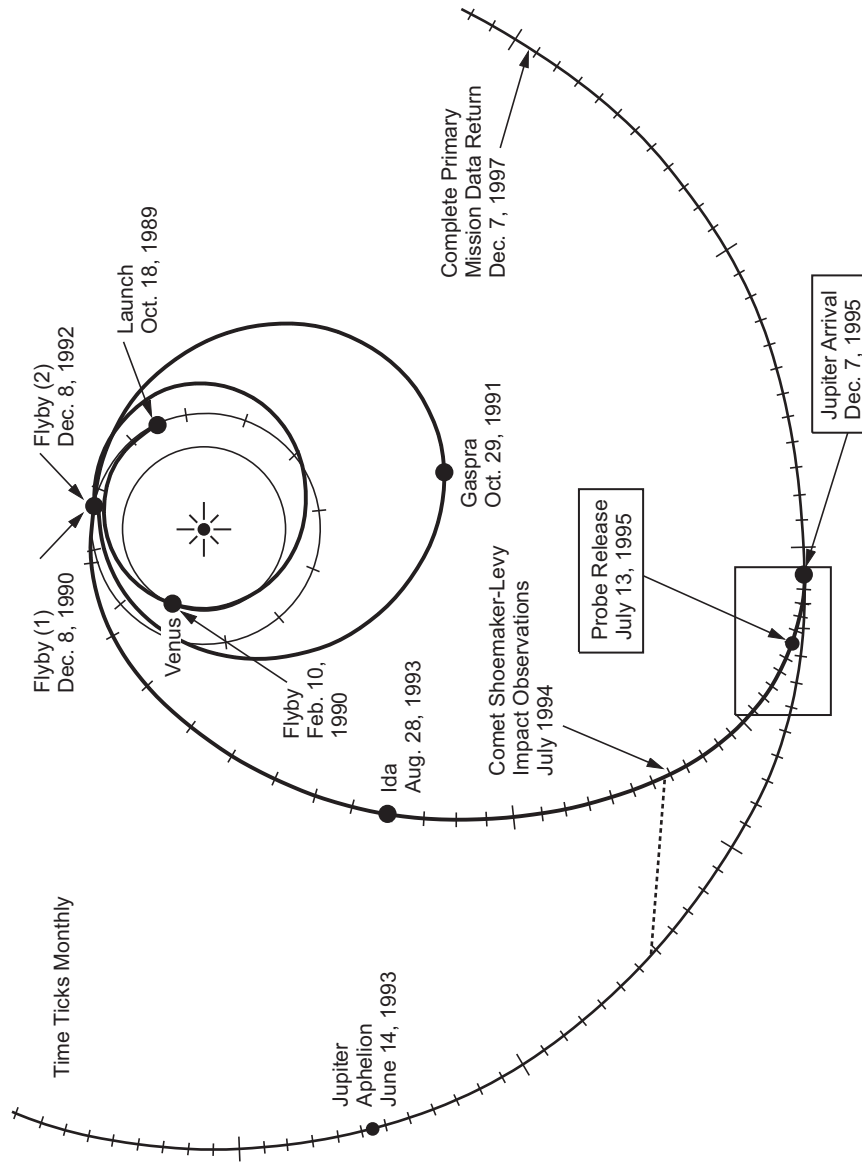
Fig. 5-6. Galileo flight trajectory.

periods, a second aft-facing LGA was added to the telecommunications system. Figure 5-7 shows the spacecraft as configured for the new trajectory that took it to Venus once and Earth twice before finally traveling to Jupiter.

This chapter describes the telecommunications antennas for the Galileo-to-Earth link. The spacecraft had an L-band antenna for relay communications to the probe. The L-band relay antenna was a 1.1-m parabolic reflector with a 21.0-dBi peak gain and a 25-deg half-power beamwidth [6]. The description of the HGA and the two LGAs are provided. Design detail, where available, is also provided. All RF measurements on the HGA that were performed in the JPL Plane-Polar Near-Field Antenna Range are also provided. The HGA was a complex mechanism. A description of its mechanics is also provided. Finally, measurement data for both low gain antennas (LGA1 and LGA2) are also provided.

On April 11, 1991 the deployment of the HGA failed. This chapter will not describe the anomaly or the subsequent investigation. Information regarding these events, as well as recovery attempts, can be found in [12–14]. The mission continued without the use of the HGA. The Galileo mission team developed techniques that utilized the LGAs [15].

5.2.1 Mission Description

The Galileo spacecraft was launched on the Space Shuttle Atlantis (STS-34) on October 18, 1989. Its mission was to conduct long-term observations of the Jovian system (Jupiter and its major moons) and included
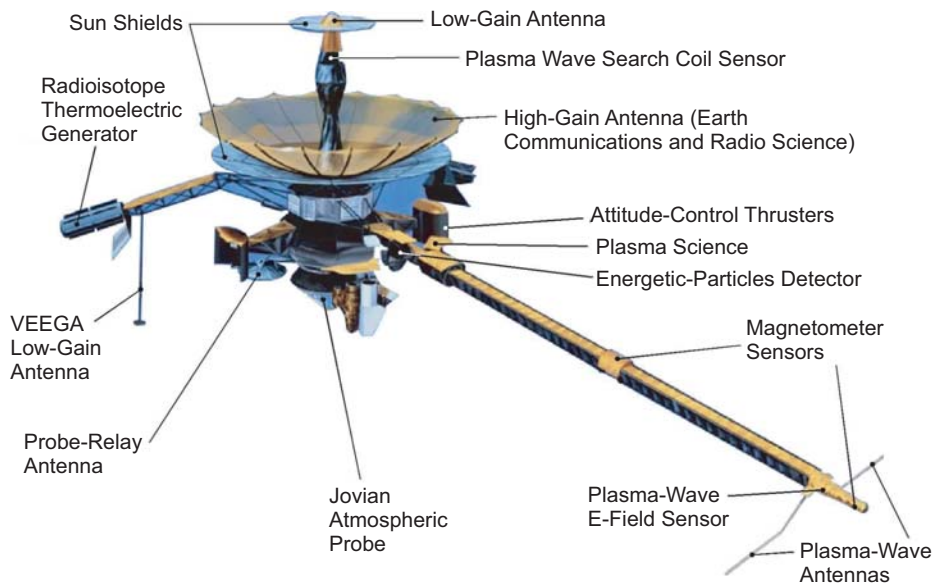

Fig. 5-7. Galileo spacecraft.

the first-ever direct measurements of the atmosphere using a descent probe. The primary mission was a 23-month, 11-orbit tour of the Jovian system, including 10 close encounters of Jupiter's natural satellites, or moons. The mission was extended three times, taking advantage of the spacecraft's durability, with 24 more orbits. The extensions made it possible to encounter all four of Jupiter's major moons: Io, Europa, Ganymede, and Callisto, as well as the small moon Amalthea.

The unique interplanetary trajectory used by the spacecraft in reaching its target is shown in Fig. 5-6. This trajectory used the gravity of both Venus and the Earth to "slingshot" the spacecraft at ever-greater velocity until finally it could begin its cruise to Jupiter. The trajectory was named Venus, Earth, Earth gravity assist (VEEGA), due to its encounters with these planets and the use of the planets' gravity. Of particular note is the duration of the cruise phase of the mission: just over six years from launch to Jupiter orbit insertion in December 1995.

Galileo observed several interesting things during its cruise: the Earth, the Moon, and mid-level clouds at Venus, all of which it mapped. Also, Galileo became the first spacecraft to encounter an asteroid when it passed within 1600 km of Gaspra on October 29, 1991, and an even larger asteroid, Ida, on August 28, 1993. Startlingly, Ida was found to have its own moon, about 1.5 km in diameter, named Dactyl, making it the first asteroid known to have a natural satellite. Finally, in March 1993, as the comet Shoemaker–Levy 9 impacted Jupiter, the Galileo spacecraft was the only observation platform with a direct view of the impact area on Jupiter's far side.

The mission carried a descent probe along with the orbiter during its interplanetary cruise. This probe weighed 339 kg and carried seven science experiments. Probe mission duration was planned for 40–75 minutes. Prior to Jupiter orbit insertion, the probe was released on a ballistic trajectory towards the planet. As the probe entered the atmosphere, and after its rapid deceleration, it deployed a parachute; then it relayed its scientific data through the L-band system on the orbiter and subsequently via the LGA1 communications system to Earth.

Figure 5-7 shows the spacecraft after deployment of the HGA. Also shown are the forward-facing and aft-facing LGAs. The HGA tip-mounted sunshield and the spacecraft bus sunshield, shown just below the HGA, provided protection from the Sun. The gross attitude stability for Galileo was provided by a spinning section of the spacecraft. However, in order to provide a stable platform for the various science instruments and cameras, a despun section was also provided. The HGA was mounted on the spin side of the spacecraft. The orbiter weighed 2223 kg and carried 12 experiments. Two radioisotope thermoelectric generators (RTG) provided spacecraft power. The telecommunications system included a 20-W S-band transmitter with a

maximum 1.2 kbps data rate and a 20-W X-band transmitter with a maximum 134-kbps data rate.

On September 21, 2003, the mission ended after the spacecraft was commanded to plunge into Jupiter's atmosphere, where it burned up after its 14-year mission. The spacecraft, mission, and scientific observations are summarized in *NASA Facts* [16].

5.2.2   Requirements

The communications requirements for the Galileo spacecraft were based on the large amount of data return expected during the mission's launch, interplanetary cruise, and orbital phases. A single antenna would not meet all of the system requirements. Therefore, the spacecraft telecommunications system consisted of three antennas: one HGA and two LGAs. Furthermore, simultaneous operation at both S-band (2115 MHz and 2295 MHz) and X-band (8415 MHz) were required. The entirety of the telecommunications antenna system, including both the HGA and the LGAs, was referred to as the S/X-band Antenna (SXA) System. This section describes all of major requirements for the Galileo SXA. The two classes of requirements described here are the functional and the design.

5.2.2.1 S-/X-Band Antenna Subsystem (SXA) Functional Requirements. The functional requirements were developed in cooperation with the spacecraft system engineer and documented in the project requirements book [17]. The basic antenna functions required were to:

* Deploy the HGA reflector after launch vehicle/spacecraft separation.
* Receive S-band signals from the DSN and conduct them to the RF subsystem (RFS) on the spacecraft).
* Transmit S-band signals from the RFS to the Tracking and Data Relay Satellite (TDRS) and to the DSN.
* Transmit X-band signals from the RFS X-band traveling-wave tube amplifier (TWTA) to the DSN.
* Receive X-band signals from the DSN and conduct them to the X/S downconverter subsystem (XSDC) on the spacecraft.

In order to meet these functions for all phases of the mission, the following equipment was required:

* HGA
* Forward-facing LGA (LGA1)
* Aft-facing LGA (LGA2)
* Transmission lines, including waveguides and associated connectors
* RF power probes located on the HGA main reflector, LGA1, and LGA2 (used for ground test)

- HGA deployment mechanism, including the rib-restraint release device with redundant non-explosive initiators, HGA deploy indicator microswitches, and motors
- HGA tip sunshield

5.2.2.1.1 RF Performance Requirements. Table 5-2 summarizes the polarization, VSWR, and gain requirements for each antenna in both transmit and receive mode. Figure 5-8 illustrates the main antenna components that provide the required functions.

5.2.2.1.2 Mass and Power. The total mass requirement of the HGA/LGA1, including the plasma wave search-coils (PWS), was 36.12 kg. Of this total, the HGA mass, including both the RF and structural components, was 32.46 kg, LGA1 and associated coaxial cable mass was 1.23 kg, and that of the PWS and its support structure was 2.43 kg. The mass of LGA2 and its transmission lines was 2.16 kg. Of that total, the LGA2 was 0.33 kg, and the transmission lines were 1.83 kg.

Prior to the Galileo mission, no other deep-space communications antenna had required input power to become operable. However, with the advent of the decision to use a deployable antenna equipped with dual redundant motors, power would be required to deploy the structure. For this antenna, the nominal voltage was 30 V (+6/–5), current was less than 0.5 amp (A) (with a maximum surge current of 1 A/s), and a nominal power was 3 W (with a 15-W maximum).

5.2.2.2 Design Requirements. The design requirements for the antenna system as derived from the functional requirements follow [18]. Derived requirements included both physical and performance parameters. Physical parameters

Table 5-2. Galileo SXA polarization, VSWR, and gain requirements summary.

Antenna	Mode	Frequency (MHz)	Polarization	VSWR	Gain (dBi)	Gain Tolerance (dBi)
HGA	Receive	2115	Linear	1.54 : 1	35.7	+0.6/-0.8
HGA	Transmit	2295	Linear	1.38 : 1	38.1	+0.6/–0.8
HGA	Receive	7167	RHCP	1.60 : 1	46.0	+0.5/–0.9
HGA	Transmit	8418	RHCP	1.20 : 1	50.1	+0.5/–0.9
HGA	Transmit	8418	LHCP	1.20 : 1	50.1	+0.5/–0.9
LGA1	Receive	2115	RHCP	1.43 : 1	6.8	+2.0/–2.4
LGA1	Transmit	2295	RHCP	1.43 : 1	7.1	+2.0/–2.4
LGA2	Receive	2115	RHCP	1.43 : 1	4.0	±1.5
LGA2	Transmit	2295	RHCP	1.43 : 1	4.5	±1.5

Low-Gain
Antenna 1 (LGA1)

HGA Tip Sunshade

LGA1 Coax Cable

HGA S-Band Feed

HGA Coax Cable

Frequency-Selective
Subreflector

HGA X-Band Feed

Orthomode Transducer/
Polarizer

Right-Hand Circular Polarized
(RHCP) Waveguide

Left-Hand Circular Polarized
(LHCP) Waveguide
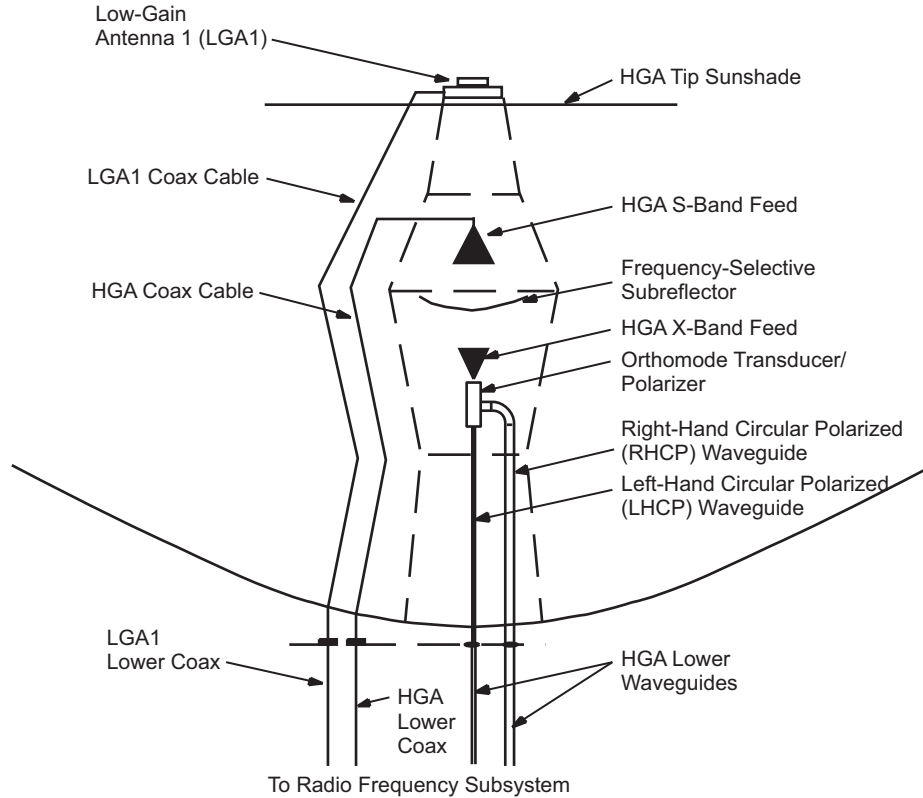
LGA1
Lower Coax

HGA Lower
Waveguides

HGA
Lower
Coax

To Radio Frequency Subsystem

Fig. 5-8. Functional layout of the Galileo antenna system.

included the mass, optical configuration, sunshields, micrometeoroid shields, venting properties, specific connector types, and even specific dimensions such as those for reflector diameters and shapes. Performance parameters included deployment motor power, pointing requirements, power handling requirements, and the apportionment of the system gain into various components, such as the HGA and its transmission lines.

The subsystem mass summary allocations to the components that constitute the SXA are shown in Table 5-3. The antenna system engineer defined these allocations as targets to meet the total functional requirement. A summary of the S- and X-band HGA RF performance requirements is given in Table 5-4. These performance requirements are set higher so that there is margin in meeting the overall functional requirements. The system LGA1 and LGA2 RF performance requirements are given in Table 5-5. Finally, Figs. 5-9 and 5-10 illustrate the minimum required LGA gain patterns for communications to Earth for the uplink and downlink frequencies. Note that these figures represent the required gain, independent of the LGA used. As discussed in Section 5.2.7,

this requirement was met by the use of two antennas, one pointed forward (the LGA1) and the other pointed aft (the LGA2).

The antenna designs that were proposed to meet these requirements are described in the next section. The final selection of the antennas was based on meeting these requirements for all conditions.

5.2.3 High-Gain Antenna Trade-off Studies

The antenna engineering team considered many options [7,8] to meet the mission requirements for the high-data-rate phases of the mission. These

Table 5-3. Galileo SXA mass summary.

Component Description	Mass (kg)
RF Components	
HGA X-band feed	0.94
HGA S-band feed	0.36
HGA frequency selective surface	0.61
HGA S-band cable assembly	0.58
HGA X-band RHCP waveguide assembly	0.50
HGA X-band LHCP waveguide assembly	0.50
LGA1	0.40
LGA1 cable assembly	0.83
LGA2	0.33
LGA2 cable assembly	1.83
RF Component Total	**6.88**
Structural Components	
Hub assembly	6.44
Rib assembly	6.63
Surface assembly	1.80
Support structure	9.37
Thermal control	2.78
Non-RF wiring	0.39
Sunshield	0.59
Micrometeoroid shield	0.97
PWS/LGA1 support structure	1.97
PWS preamp adapter plate	0.17
PWS conduit	0.26
Optical alignment assembly	0.03
Structure Total	**31.40**
High/Low Gain Antenna Assembly Total	**38.28**

Table 5-4. Galileo high-gain RF performance requirements.

Frequency (MHz)	2295 ±5	2115 ±5	8418 ±23
Polarization	Linear	Linear	RHCP, LHCP
Gain (dBi)	37.6	36.4	50.1
3-dB beamwidth (deg)	>1.8	>2.0	>0.45
10-dB beamwidth (deg)	>3.1	>3.4	>0.75
First sidelobe location (deg from peak)	>3.0	>3.2	>0.70
First sidelobe level (dB)	>15	>15	>14
Axial ratio (on axis to –3 dB level, dB)	n/a	n/a	1.5
Axial ratio (–3 dB level to –10 dB level, dB)	n/a	n/a	3.0
Cross-polarized component (dB)	>20	>20	n/a
VSWR	1.38:1	1.54:1	1.2:1
Power handling (W, CW)	120	n/a	100
Isolation (between polarizations, dB)	n/a	n/a	18
RF axis alignment (to mechanical boresight, deg)	0.03	0.03	0.03
System mode of operation	Transmit	Receive	Transmit

considerations included a review of what had been previously flown on JPL/NASA missions, what was currently available from industry, and what could be developed to meet the requirements. The three options at the forefront of consideration, one classical and two deployable, for the HGA are described below.

5.2.3.1 Solid Fixed-Size Reflectors: The Voyager Design/Spare. The use of spare antennas from the Voyager Project was initially considered for the mission. Since Galileo planned on a Space Shuttle launch, a maximum volume was defined that could (barely) be met by Voyager's 3.6-m antenna. Nevertheless, because there were spare Voyager Project HGAs in storage, this option seemed a reasonable way to economically meet requirements. However, in the early stages of project planning, the desired data rate was increased such that it became apparent that an antenna of somewhat larger diameter would be required, eliminating the Voyager option as a solution. (Voyager's spare antenna remained in storage until used by the Magellan mission to Venus years later.)

5.2.3.2 Deployable Antennas: Lockheed Wrap-Rib and the TDRSS Antennas. Since a 3.6-m antenna was the largest antenna that could be fit into the Shuttle cargo bay, it became apparent that some technology for a deployable

Table 5-5. Galileo LGA system RF performance requirements.

	LGA1		LGA2	
Frequency (MHz)	2295 ±5	2115 ±5	2295 ±5	2115 ±5
Polarization	RHCP	RHCP	RHCP	RHCP
Gain (dBi)	7.1	7.1	4.5[†]	4.0[†]
3-dB beamwidth (deg)	>45	>36	>40, <60	>35, <50
10-db beamwidth (deg)	>65	>70	n/a	n/a
Axial ratio (boresight, dB)	2.0	2.0	<8	<10
Axial ratio (45 deg off boresight, dB)	n/a	n/a	<4	<6
Axial ratio (90 deg off boresight, dB)	11	6	<17	<20
VSWR	1.43:1	1.43:1	1.4:1	1.4:1
Power handling (W, CW)	120	n/a	120	n/a
RF axis alignment (to mechanical boresight, deg)	1.0	1.0	1.0	1.0
System mode of operation	Transmit	Receive	Transmit	Receive

[†] Measured at the peak of the gain curve, not coincident with mechanical boresight

antenna would be required. During the early phases of the project, two candidate technologies being developed by industry were investigated. First was a design proposed by Lockheed Space Systems that consisted of a set of flexible ribs that supported a mesh surface and that were wrapped about and constrained to a central hub. The stored energy of the ribs provided for the deployment of the reflector system. Deployment of this antenna would occur in a matter of seconds once the constraint system was released. The second design under consideration was that being developed by Harris Corporation for the orbital element of TDRSS. It consisted of a set of stiff graphite ribs supporting a mesh surface. The deployment of this system required several minutes and is best described as opening much like an umbrella. After careful consideration, the TDRSS configuration was selected and detail design of RF components started.

5.2.4 Post-Challenger Modifications

After the Shuttle Challenger accident, the passage to Jupiter was modified. The new trajectory would require the spacecraft to fly closer to the Sun than originally planned. Whereas the original design margin allowed solar flux at 0.98 AU, the new route was to fly close to Venus. As a result, several hardware modifications and operational changes were required. Operationally, it was determined that the HGA would remain stowed and shielded from the Sun
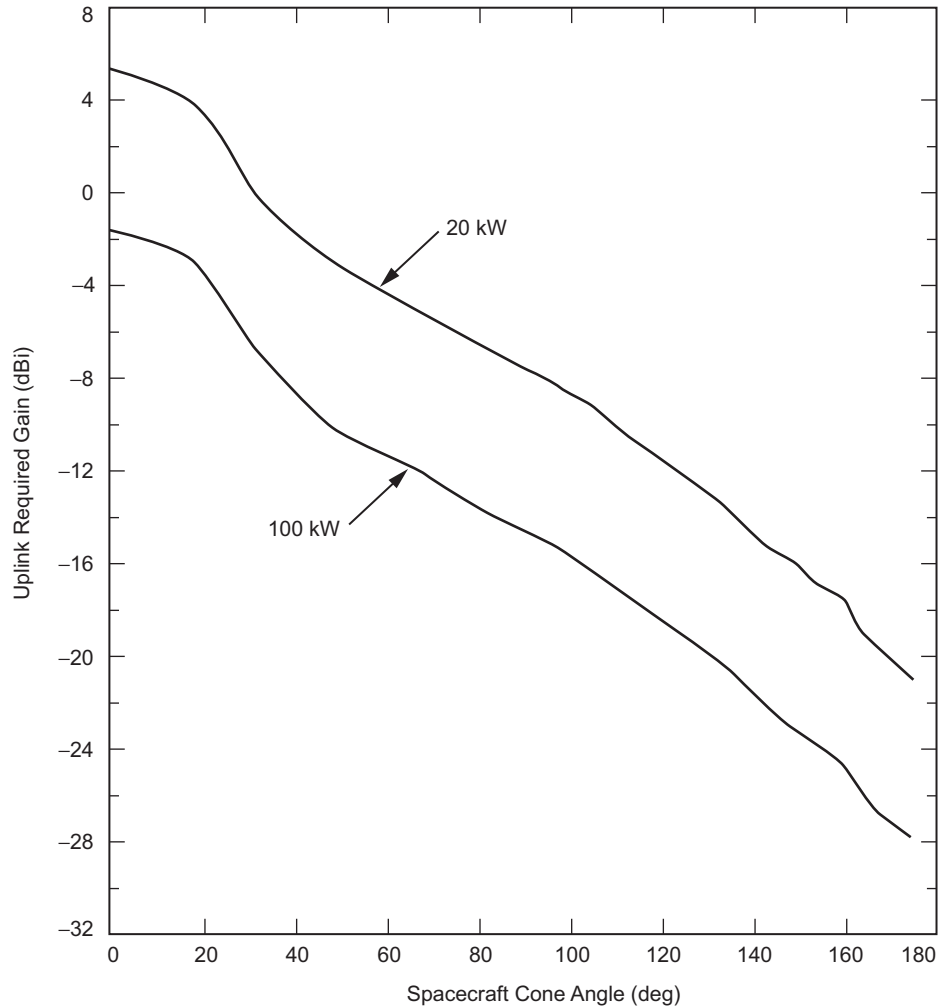
Fig. 5-9. Galileo LGA minimum required gain vs. cone angle, 2115 MHz.

behind a new sunshield placed at the tip of the antenna. In this configuration, the spacecraft could remain Sun-pointed, thus protecting the HGA behind the sunshield. However, the single LGA (LGA1) that was planned to support the mission, and which was already mounted to the HGA, could not support Earth coverage because of the need to have it continuously Sun-pointed. In other words, there would be times in the early phases of the mission that Earth would be in the back lobes of LGA1. The total gain requirement (as illustrated in Figs. 5-9 and 5-10 could not be met by the LGA1 alone. It was determined that a second LGA would be required. Furthermore, this LGA2, pointing in the aft-direction, would require a gain pattern that was peaked at some angle off its
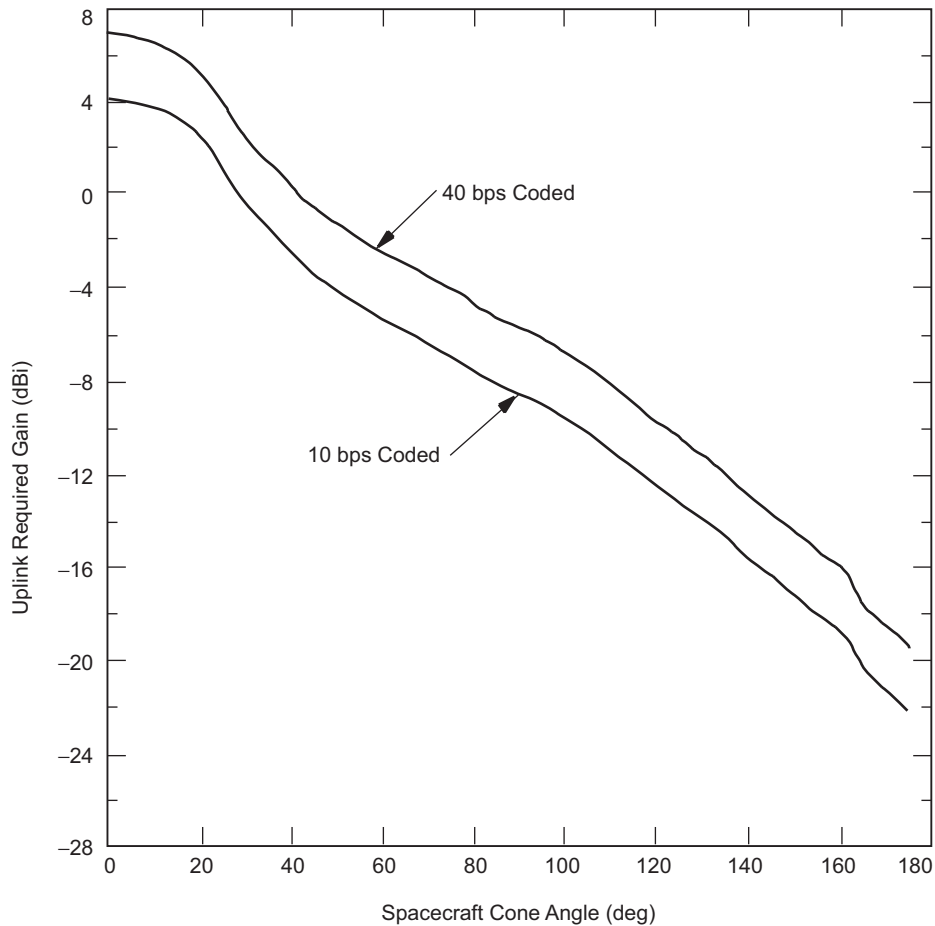
Fig. 5-10. Galileo LGA minimum required gain vs. cone angle, 2295 MHz.

mechanical boresight in order to meet the total system gain requirement. A design effort was undertaken to meet the new requirements.

5.2.4.1 Tip Sunshield. A basic requirement for the tip sunshield was to be transparent to the radio signals sent to and from the HGA. This suggested a nonconductive dielectric material. However, electrostatic discharge (ESD) requirements for spacecraft hardware included a path for charged particles to reach the electrical bus ground. These seemingly conflicting requirements were met because the discharge path was allowed to be through a fairly large resistance, including a dielectric material acceptable to the antenna designers. The sunshield for this function consisted of a carbon-coated Kapton. The material was stretched between a set of radial spokes. made of invar, a

conductive nickel-iron alloy. The shade mounting was designed to fit to the tower structure, using the LGA1 mounting holes, after which LGA1 was mounted to the sunshield. The vibration environment that the tip of the HGA would be exposed to during the Shuttle launch was to exceed 50 g. As a result, it was essential that the total mass be limited. The entire structure and shade material had a total mass of 0.6 kg. The sunshield that provided shelter for the HGA is shown in Fig. 5-11. The picture shows the sag in the sunshield due to gravity. In flight, this sunshield assumes a flat shape. RF measurements of the sunshield showed negligible gain loss [19]. Furthermore, the effect to the LGA1 patterns was also negligible.

5.2.4.2 Aft-Facing Low-Gain Antenna. The new, aft-facing (LGA2) antenna was used during the early mission stages. LGA requirements, shown in Section 5.2.2, included all cone angles for both the uplink and downlink frequencies. Even though the required gain in the region from 90 to 180 deg was low, it was not insignificant. However, it was important that all areas of this curve be met. The design selected is described in Section 5.2.7. Section 5.2.7.3 illustrates the total gain versus the requirements.

Fig. 5-11. Galileo tip sunshield being tested on the lateral vibration fixture.

5.2.5 High-Gain Antenna Design Selected

Armed with the knowledge gained from the industry surveys, the project decided that a selection of the HGA system could be made based on engineering criteria. As mentioned earlier, the Harris Corporation radial-rib design was chosen to meet the Galileo antenna system requirements.

5.2.5.1 High-Level Overview. One of the basic considerations in selecting not only the HGA, but also the feeds and other microwave components, was hardware heritage, or having been flown on previous missions. The initial design for the Galileo SXA was based on that of TDRSS antennas, which had recently been developed for TRW, Inc. However, due to the difference in frequencies from the TDRSS mission, the feeds had to be changed. Furthermore, the optics had to be designed to allow for simultaneous S/X band operation. The successful Voyager mission had just flown, and during its development, an X-band feed and polarizer had been designed. By leveraging the Voyager antenna design, both the cost and the RF performance risk of the Galileo antenna was reduced.

Figs. 5-12, 5-13, and 5-14 illustrate the salient features of the Galileo HGA and LGA1, discussed below, in top-down order. (Missing from these figures is the sunshield added to the structure as a result of the redesign for the VEEGA trajectory). The RF components are all located in the tower structure. LGA1 is atop the plasma wave search-coil support structure. The S-band feed is at the prime focal point of the main reflector, looking downward through the frequency selective subreflector (FSS). The X-band feed is connected to a dual polarization orthomode transducer (OMT). When the antenna is deployed, the graphite ribs support a surface of gold-plated wire mesh that is connected to a set of stand-offs and ties that hold it in the desired shape. The mesh, which is a 0.0013-in. (0.03-mm) gold-plated molybdenum wire, woven into a tricot fabric is discussed in Chapter 1. This weave is exactly the same as that used for nylon stockings, but with a very loose 10 holes per inch (4 holes/cm) weave. The optics design of the fully deployed system is that of a dual-shaped Cassegrain X-band system and a focal feed S-band system.

The mechanical system included the eighteen ribs, the tip restraint used to circumferentially constrain the stowed ribs during launch, the central release mechanism and upper structure, the radome, the truss supports, the hub assembly, the hub carrier, and the dual-drive motors. Deployment was accomplished by the hub being moved upwards by a motor and ballscrew combination, and the deflection of the ribs that are pinned to the hub at the pivot point. The method was very much like opening an umbrella.
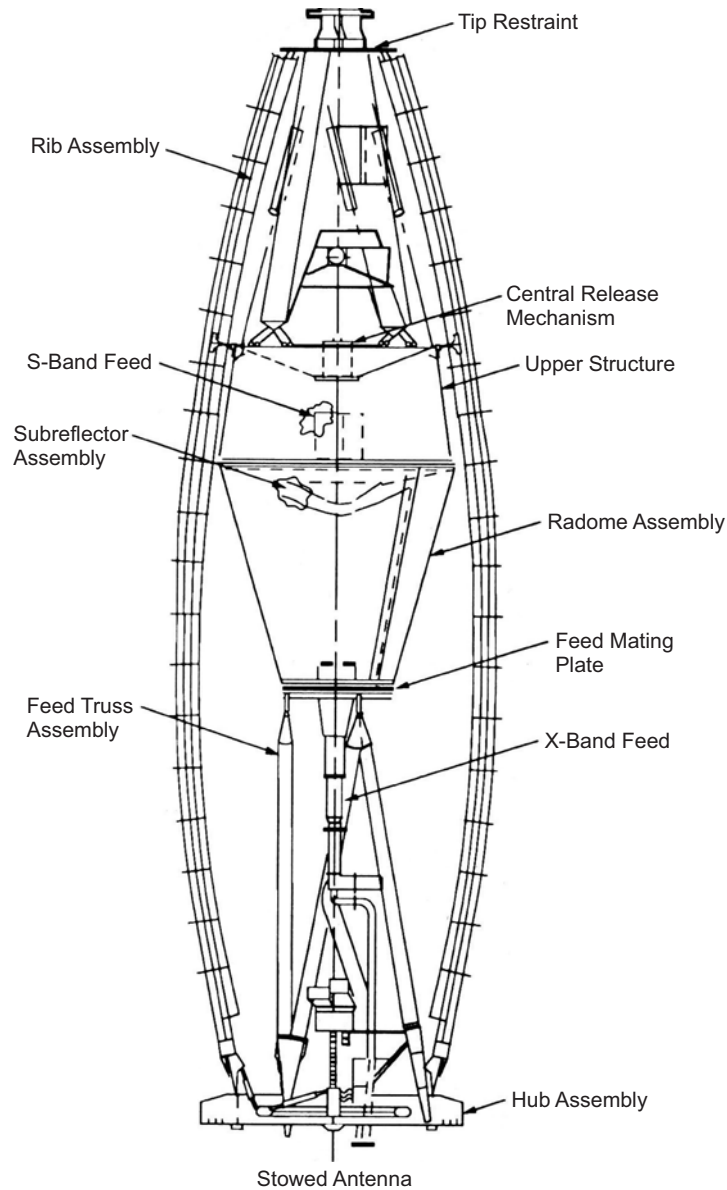
Fig. 5-12. **Galileo HGA stowed configuration.**

5.2.5.2 Mechanical Mechanisms and Structural Components. Although this chapter focuses on the RF and electrical characteristics and design of the Galileo SXA, a brief overview of the mechanical and structural system is useful. At the time of development, this antenna design was clearly the most mechanically complex device flown for deep-space science missions. The
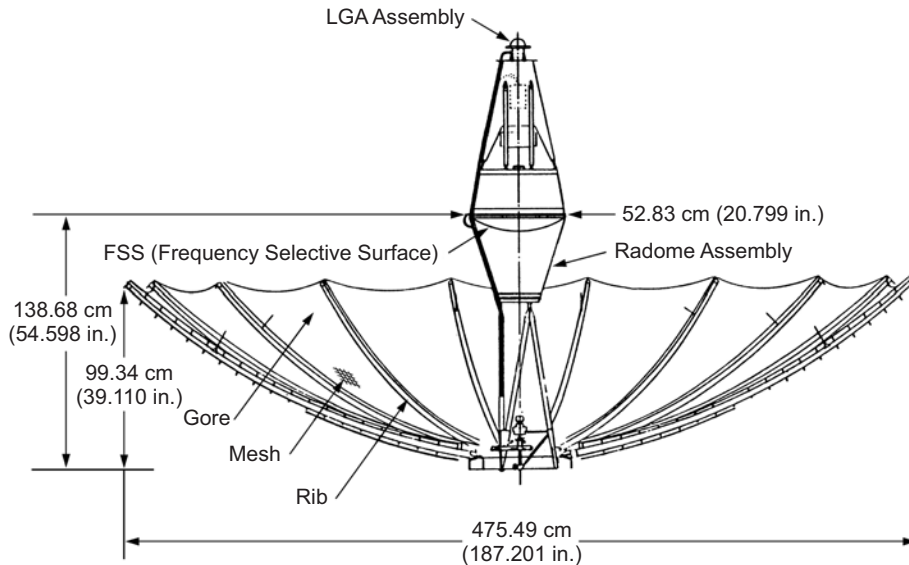
LGA Assembly

52.83 cm (20.799 in.)

FSS (Frequency Selective Surface)

Radome Assembly

138.68 cm (54.598 in.)

99.34 cm (39.110 in.)

Gore

Mesh

Rib

475.49 cm (187.201 in.)

Fig. 5-13. Galileo HGA deployed configuration.

fundamental purpose for the antenna was to act as an RF device to capture RF energy, route it to a focal point and further to the receivers, or vice versa, from the transmitters to the antennas. Nevertheless, because it fit into the Shuttle bay, the Harris design was a mechanical marvel for its time. An excellent description of the mechanical system can be found in the literature on the TDRSS antenna [11].

Construction. The construction of the antenna system differed in several areas from that of the TDRSS antenna. Notwithstanding these differences, the construction of the antenna followed the same process as the many previous TDRSS antennas. The system included 18 carbon fiber ribs curved in approximately the required shape. The gold-wire mesh was supported along the radius of the ribs by a series of stand-offs. Between ribs, a set of circumferential cords at different radial distances was strung below the mesh surface and tied with short wires to the surface of the mesh, forming the required final surface shape.

Non-HGA structure: plasma-wave search-coils. The feed tower was required to support the plasma-wave search-coils (PWS). To accomplish this, a fiberglass A-frame structure was mounted on the subreflector support cone. The other significant changes to the TDRSS design were constrained to the deployment system, and are described below.

Deployment system. By its very nature, a deployable antenna requires a system to bring it to its final state. For the Galileo SXA, the deployment system included the motors required to turn a ballscrew, which in turn moved upward a carrier connected to the ends of 18 ribs. As the carrier moved upwards, the ribs,

Fig. 5-14. Galileo antenna deployed on its ground handling fixture.

which were pinned several inches above the carrier at a fulcrum point, began to rotate outward, deploying the antenna and forming the surface of the reflector. The deployment system also included a mechanism that held the ribs close and tight to the structure in order to withstand the high vibration loads experienced during the launch phase. Finally, because of the addition of the PWS and LGA1 support structure, an anti-snag system was added at the outermost tip, or maximum diameter, of the antenna. A brief description of each of the major elements of the deployment system follows.

Redundant dual-drive motors. The motors used to deploy the Galileo SXA were different than those of the TDRSS system. They were developed at

JPL, specifically to be used in flight missions where high reliability, high torque, and total redundancy were required. The dual-drive motors used included two motors, each of which was connected to the rotating ballscrew. The torque delivered was to be adequate to tear mesh in the event of a mesh snag.

Central release mechanism. Another part of the deployment system that differed from that of TDRSS was the device that held the 18 ribs tightly to the central tower for the launch phase. This device was called the central release mechanism (CRM); it held 18 wires that were connected to each rib of the antenna. The end of each wire was fitted with a swage ball, which fit into the CRM and was held in place until released. The release occurred when a nonexplosive initiator, or burn wire, was activated. (The ultimate nondeployment of the system was traced to the sticking of several ribs to the central tower structure after the nonexplosive initiator released all 18 ribs. See [13,14] on the deployment anomaly.)

Anti-snag system. During the testing of the SXA, it was found that an occasional snag of mesh would occur at the tip of the stowed antenna after launch-load lateral vibration. Accordingly, part of a panel of mesh was added that followed the back of the rib from the tip, down several inches. This cocoon of mesh prohibited the mesh from becoming entangled with either the LGA1 support structure or the tip of the ribs. After installation, no further snags of this nature occurred in test.

5.2.6 Radio Frequency System—High-Gain Antenna

5.2.6.1 HGA Optics. Shaping a reflector system optimizes for the highest frequency of operation and, in the case of Galileo, was done to maximize the gain. Thus, the aperture distribution was very nearly uniform across the face of the deployed dish, with a very sharp fall-off of power at the edges of the dish. The S-band feed, located at the primary focal point of the dish illuminated the reflector by viewing it through the shaped subreflector. The main reflector was shaped by the use of 18 rows of circumferential cords stretching from rib to rib on the back side of the ribs and connecting to the surface of the mesh using ties that were individually set to hold the mesh in its prescribed shape. The importance of this shaping system cannot be overstated. While the project was investigating methods to eliminate these cords as potential snags for antenna deployment, an analysis was done [20] to determine the gain loss. With all the cords removed, the X-band loss would be approximately 5.4 dB while the S-band loss would be approximately 0.5 dB. Alternatively, removing only the outermost four rows of cords would cause a loss of approximately 1 dB [21]. Ultimately, this loss in gain was deemed unacceptable, and the antenna was not modified.

The optics configuration is summarized in Fig. 5-15. The positions of the feed horns with respect to the vertex of the reflector are provided. The surface of the main reflector is defined by a sixth-order polynomial. The coefficients of this polynomial are given in Table 5-6.

5.2.6.2 S-Band. The S-band feed is shown in Figs. 5-16 and 5-17. This feed was an E-plane sectoral horn, and it received and transmitted only linearly

Fig. 5-15. Galileo optics configuration.

**Table 5-6. Equation and coefficients defining shape of the
Galileo HGA main reflector.**

Coefficient	Value	
6	$0.134268864 \times 10^{-10}$	$F(x) = A_6 x^6 + A_5 x^5 + A_4 x^4$
5	$-0.410523382 \times 10^{-8}$	$+ A_3 x^3 + A_2 x^2 + A_1 x + A_0$
4	$0.455319128 \times 10^{-6}$	
3	$-0.24178805 \times 10^{-4}$	
2	$0.522080064 \times 10^{-2}$	
1	$-0.21984271 \times 10^{-2}$	
0	5.583933584	

polarized energy. Note that the horn flared out in only one dimension. This feedhorn was designed to have 37.3 dBi gain at 2115 MHz, 38.1 dBi gain at 2295 MHz, and to be symmetric in the two orthogonal planes. During the design and breadboard phase of the project, it was determined that there was a resonance in the tower structure between the X-band feed and the upper support structure. The presence of the FSS radically changed this resonance at 2295 MHz but had little effect at 2115 MHz. Two shorting plates were fabricated, one to electrically tune the depth of the upper structure around the S-band horn, and the other to electrically match out the center blockage reflections. Figure 5-18 illustrates the configuration of the tuning plates. The precise location of these plates was determined empirically by measuring the system gain as a function of the separation of the plates and the location with respect to the feedhorns. The radiation patterns of this feed in the final configuration, including tuning plates, are shown in Fig. 5-19.

Given the feed and its associated radiation patterns, the performance of the system was measured in a near-field facility constructed specifically for this project [22,23]. The project chose this path for antenna characterization based on the recent advances in near-field calibration techniques at the U.S. National Institute of Standards and Technology (NIST) and at JPL [24,25]. The measured far-field radiation patterns were measured at both the uplink (2115 MHz) and downlink (2295 MHz) frequencies. Figure 5-20 shows the results of these measurements [26].

5.2.6.3 X-Band. The X-band feed design was inherited directly from Voyager. Known as a Potter horn, it was smooth walled, with a launching section that ultimately resulted in a fairly narrow-banded feed that provided very symmetric patterns in any two orthogonal cuts. See Chapter 3 of this book for a detailed description. Note, however, that because of the difference in the ratio of the

HGA S-Band Feed Horn

A   A   B

C

5.46 cm
(2.15 in.)   9.02 cm
                                                                              (3.55 in.)

C

4.32 cm
(1.70 in.)

B

10.03 cm (3.95 in.)

16.26 cm (6.40 in.)

4.70 cm
(1.85 in.)   **View
                                                                              A-A**

                                                                              9.40 cm
                                                                              (3.70 in.)

4.70 cm
(1.85 in.)

View B-B   **Vlew C-C**

9.02 cm
(3.55 in.)

9.40 cm
(3.70 in.)
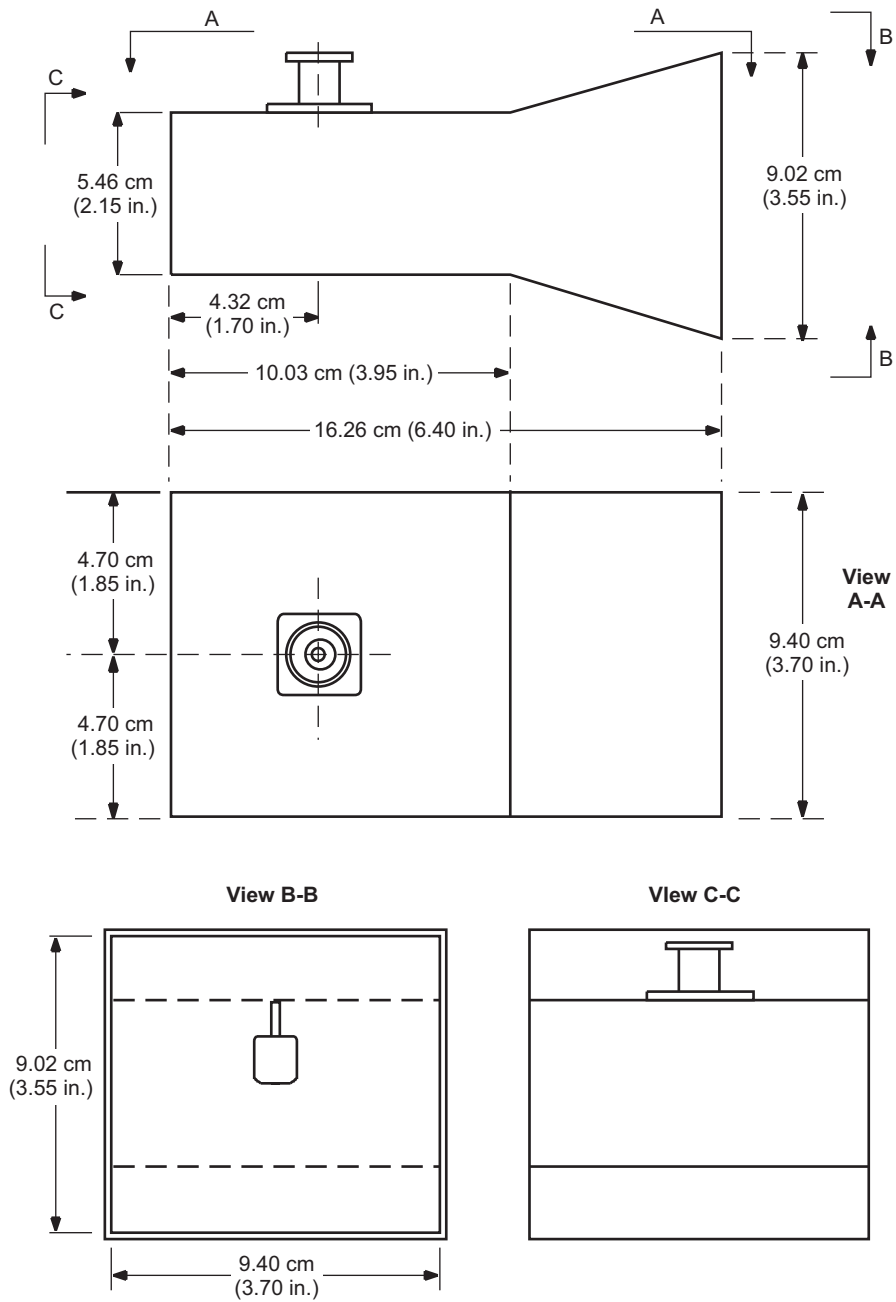
Fig. 5-16. Galileo S-band feed showing three views of the sectoral horn.
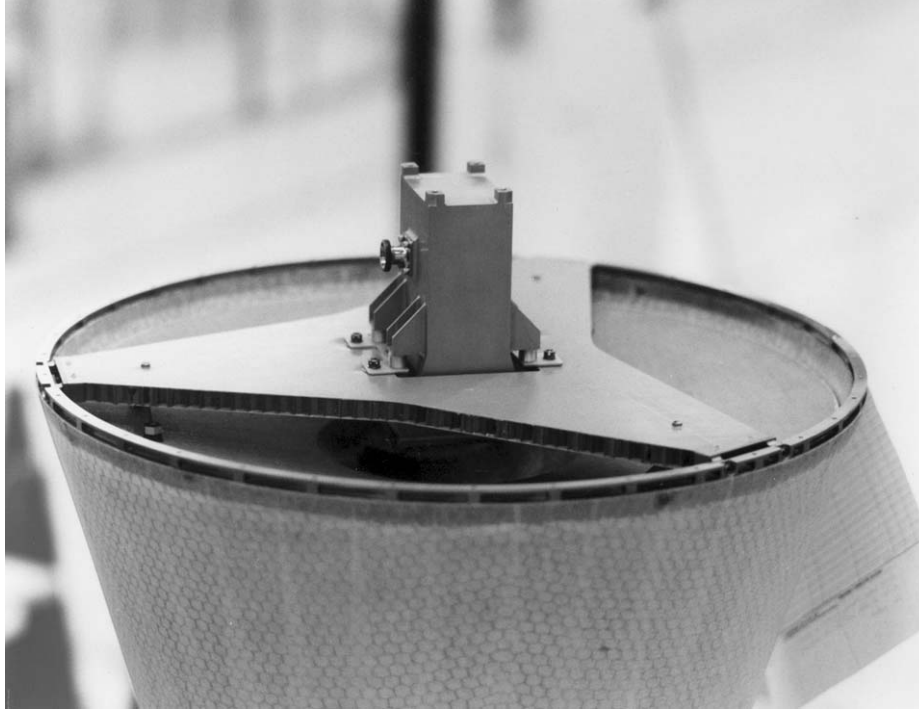
Fig. 5-17. Galileo S-band feed mounted on the top of the radome.

focal length to diameter of the main reflector (f/d), the edge taper had to be different than that of the Voyager feed. This was easily accomplished by using a feed with lower gain. Thus, the Galileo feed, while being *exactly* the same as the Voyager feed from the dual-polarized orthomode transducer and through the phasing section, was shorter by several inches to provide the wider pattern necessary for the different reflector. The radiation patterns of this feed are shown in Fig. 5-21, and the resulting far-field patterns are given in Fig. 5-22.

5.2.6.4 Frequency Selective Subreflector. An FSS was used to enable dual-frequency response to both X- and S-band. It consisted of a series of crossed dipoles that were resonant at the frequencies of interest. In this case, the FSS was invisible to S-band radiation but looked like a solid reflector at X-band. The subreflector was a dual-surfaced fiberglass and NOMEX honeycomb material with copper etched into the surface for the dipoles. During development tests, the X-band gain was measured alternatively with the FSS and with a solid subreflector. The gain loss due to this FSS at X-band was approximately 0.24 dB. This reflector is shown in Fig. 5-23.

111.178 ± 0.635 cm
(43.771 ± 0.250 in.)

Shorting Ring
Around X-Band Horn

112.504 ± 0.953 cm
(44.293 ± 0.375 in.)

153.048 ± 0.559 cm
(60.255 ± 0.220 in.)

154.838 ± 0.254 cm
(60.96 ± 0.10 in.)

Shorting Plate

174.429 ± 0.381 cm
(68.673 ± 0.150 in.)
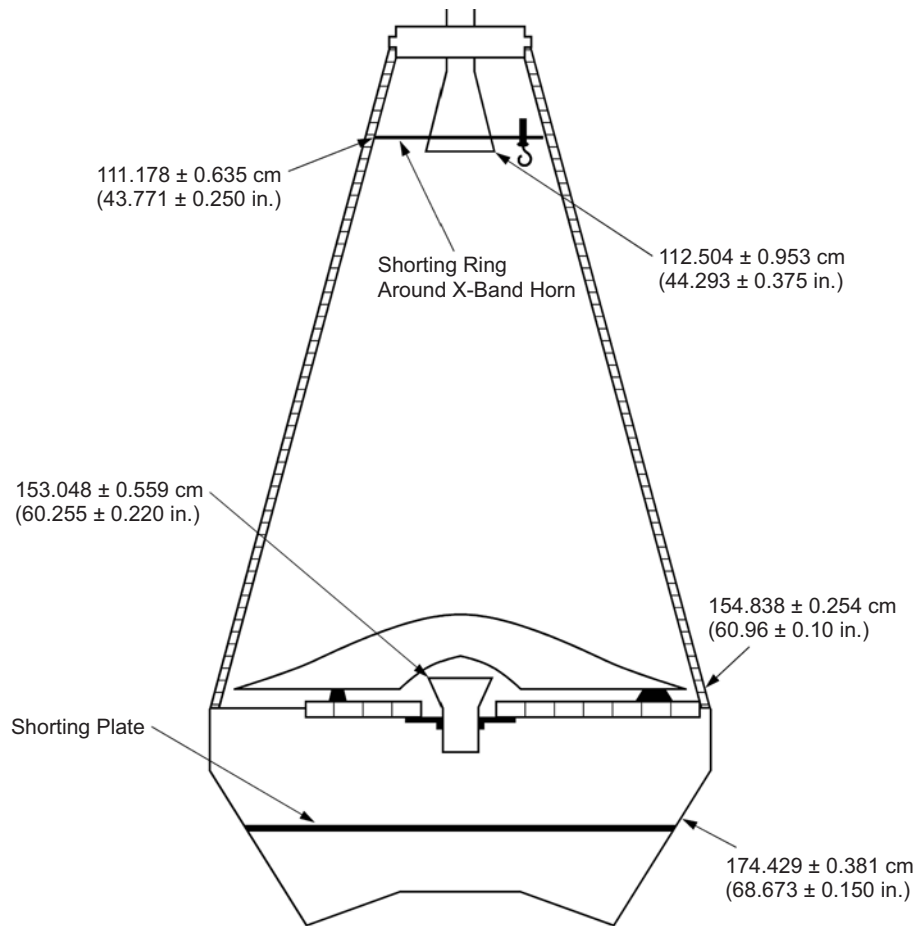
Fig. 5-18. Configuration of the tuning plates in the Galileo upper structure and radome.

5.2.7   Low-Gain Antenna System

The LGA requirements were set such that a communications link could be maintained during all phases of the mission. The original requirements for this mission were for coverage only in the forward direction, which was in the same direction as the main beam of the HGA. When the trajectory was changed later in the mission, the requirements were changed; and, as a result, coverage in both forward and aft directions was included. After much investigation, an LGA system consisting of two antennas was selected. This section describes the design of the two different LGAs and compares their performance to the system requirements.

(a)
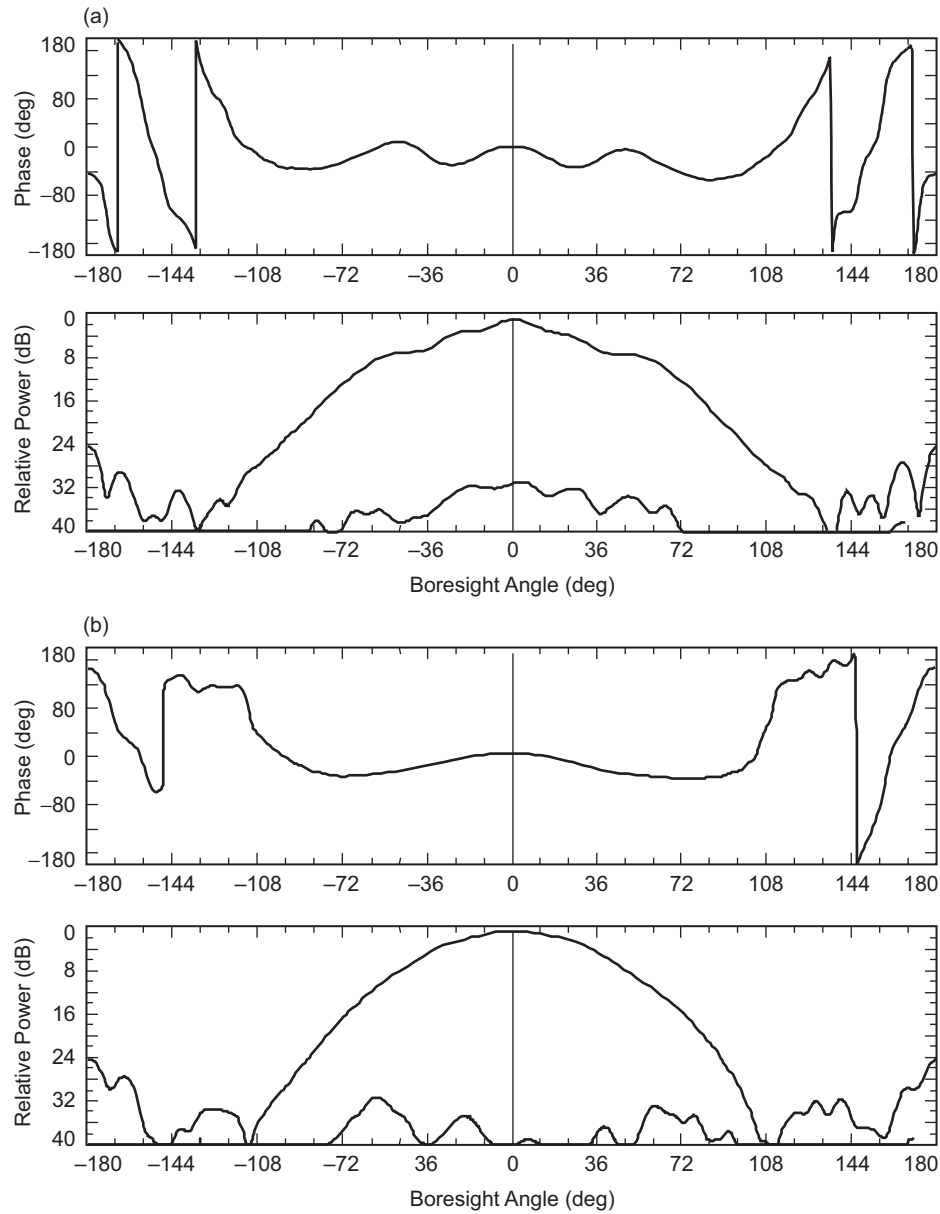
Fig. 5-19. Galileo S-band feed pattern cuts, f = 2295 MHz,
for (a) E-plane and (b) H-plane.

5.2.7.1 LGA1 (Forward Facing) RF Design. The LGA1 for the Galileo
spacecraft was also inherited directly from the Voyager LGA as shown in
Chapter 3. The LGA1 was simply a build-to-print of the Voyager LGA. Its
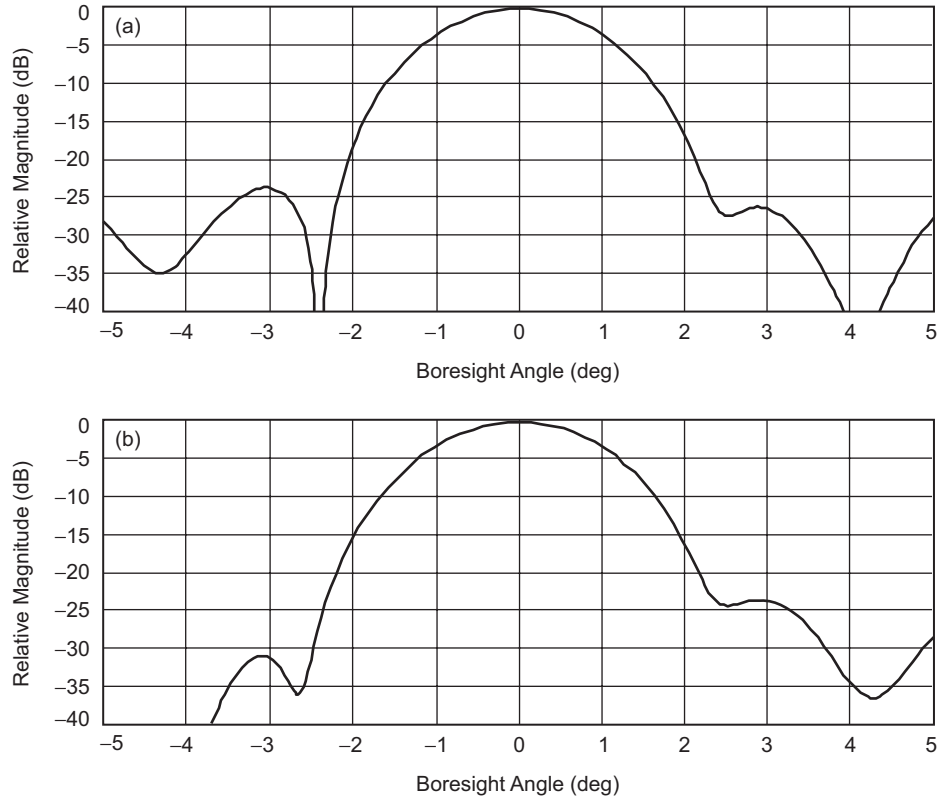
**Fig. 5-20. Far-field patterns of the Galileo HGA, f = 2295 MHz,
for (a) phi = 0 deg and (b) phi > 90 deg.**

mounting position was also similar to that of the Voyager LGA; however, a significant difference was that there was a small ground plane separating the LGA1 aperture from the main reflector behind it. It was expected that there would be considerable currents on the rim of the LGA1 that could, in turn, interact with the main reflector. This may have prevented the LGA1 from meeting requirements. Figure 5-24 show the free-space far-field patterns of the LGA1. These patterns were of just the antenna without the main HGA reflector behind it. In order to put a bound on the problem, a series of far-field measurements of the LGA1 was made where it was placed in front of a 5-m test reflector [27]. Figure 5-25 provides the results of this testing. There is high (spatial) frequency ripple across the pattern, with a predominant peak in the boresight direction. When this pattern is compared to specifications in Section 5.2.3.7, one finds that even with the ripple, the requirements are met.

5.2.7.2 LGA2 (Aft Facing). A review of the LGA system gain requirements (Section 5.2.2) shows that the required gain decreased monotonically as the
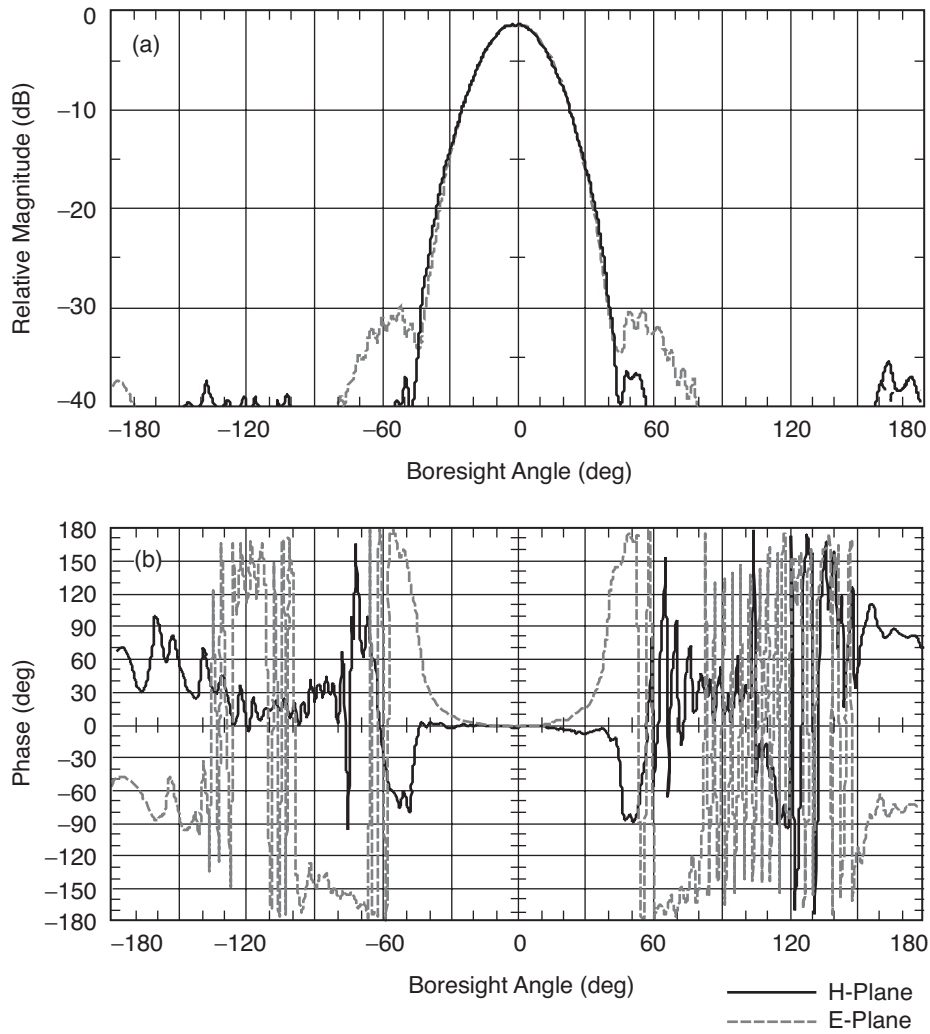
Fig. 5-21. Galileo X-band feed pattern cuts, f = 8415 MHz, with (a) amplitude patterns and (b) phase patterns.

direction angle increased from the forward direction (0-deg spacecraft cone angle) towards the aft direction (180-deg spacecraft cone angle). LGA1 was designed to meet the requirements from 0 deg to 120 deg, while LGA2 was designed to meet the requirements from 120 deg to 180 deg. Note that the requirements were to be met for all azimuth angles at every cone angle. Therefore, since LGA2 was to be mounted so that its mechanical axis was pointed at the spacecraft 180 deg, the design choice was to either provide an antenna with enough boresight gain so that at the antenna's 60-deg angle the requirement was still met; or to provide an antenna with lower gain on its
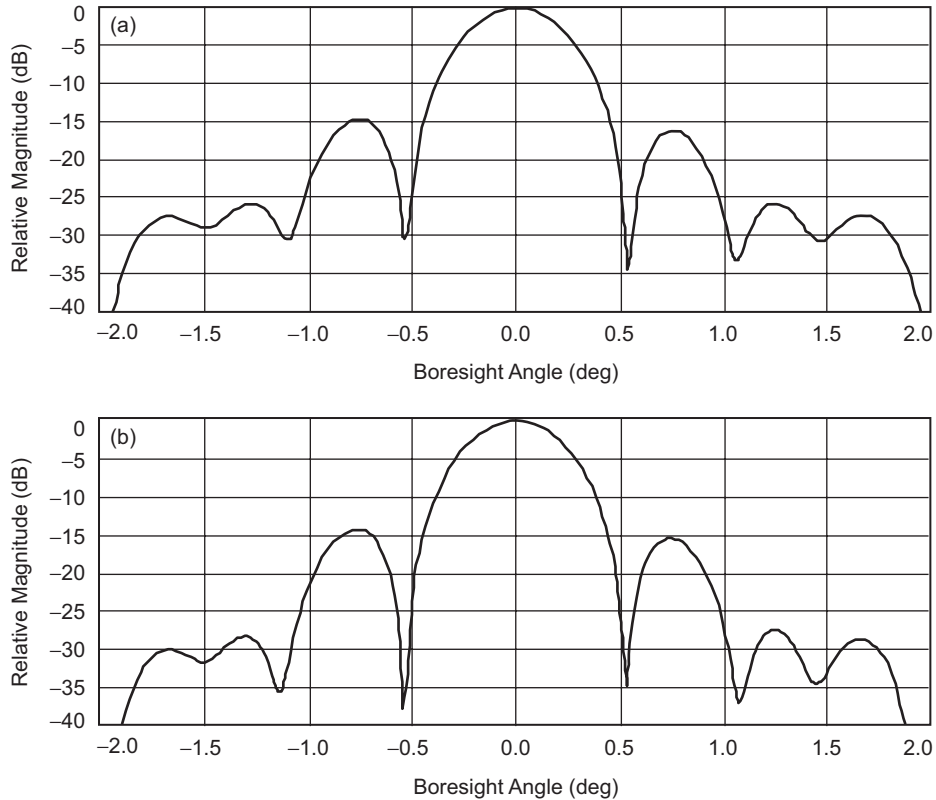
Fig. 5-22. Far-field patterns of Galileo HGA, f = 8415 MHz, with (a) phi = 0 deg and (b) phi = 90 deg.

boresight in order to spread the energy out to a wider angle off of its boresight. The latter design choice was made after it was determined that the gain and beamwidth relationship conspired to make it impossible to meet the requirement with a typical LGA. Specifically, the system gain coverage 60 deg off boresight (at the spacecraft 120-degree cone angle) could not be met since, as the gain of the antenna increased, the beamwidth decreased. This section describes how the system gain requirements for the aft direction were met.

5.2.7.2.1 LGA2 RF Design. As stated above, it was required that the LGA2 be designed such that the gain at some direction away from the mechanical boresight be higher than the gain in the boresight direction. One type of antenna that meets that requirement is a crossed drooping-dipole antenna [28]. This type of antenna consists of crossed dipoles of different lengths, held over a ground plane, drooping with respect to the normal to the ground plane. Finally, the match of the dipoles is obtained by using a split-tube balun [29] between the

(a)

(b)
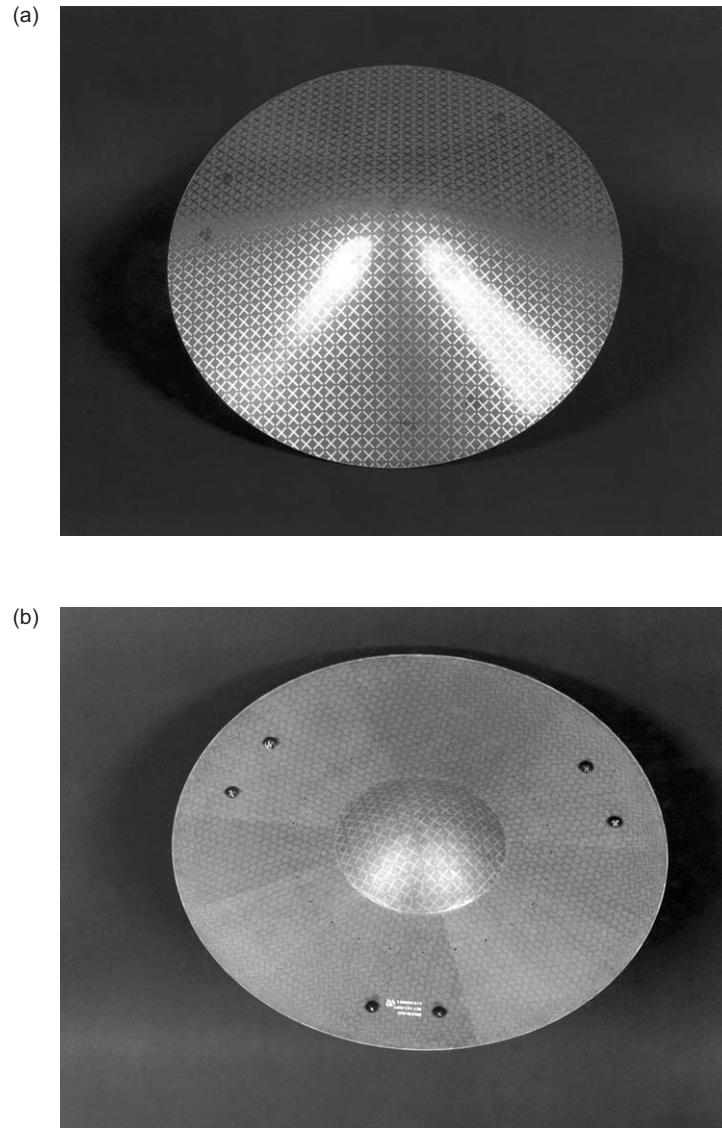
**Fig. 5-23. Galileo frequency selective surface (FSS) subreflector:
(a) front and (b) back.**

inner and outer conductors of the coaxial feeding structure. This antenna type is constructed on the structure of a 0.5-in. (1.26-cm) semi-rigid coaxial cable. This aluminum cable uses a series of Teflon tubes to locate the center conductor. The cap of the LGA2 was soldered to the top of the coaxial cable joining the inner and outer conductors. The balun slots were shorted at the
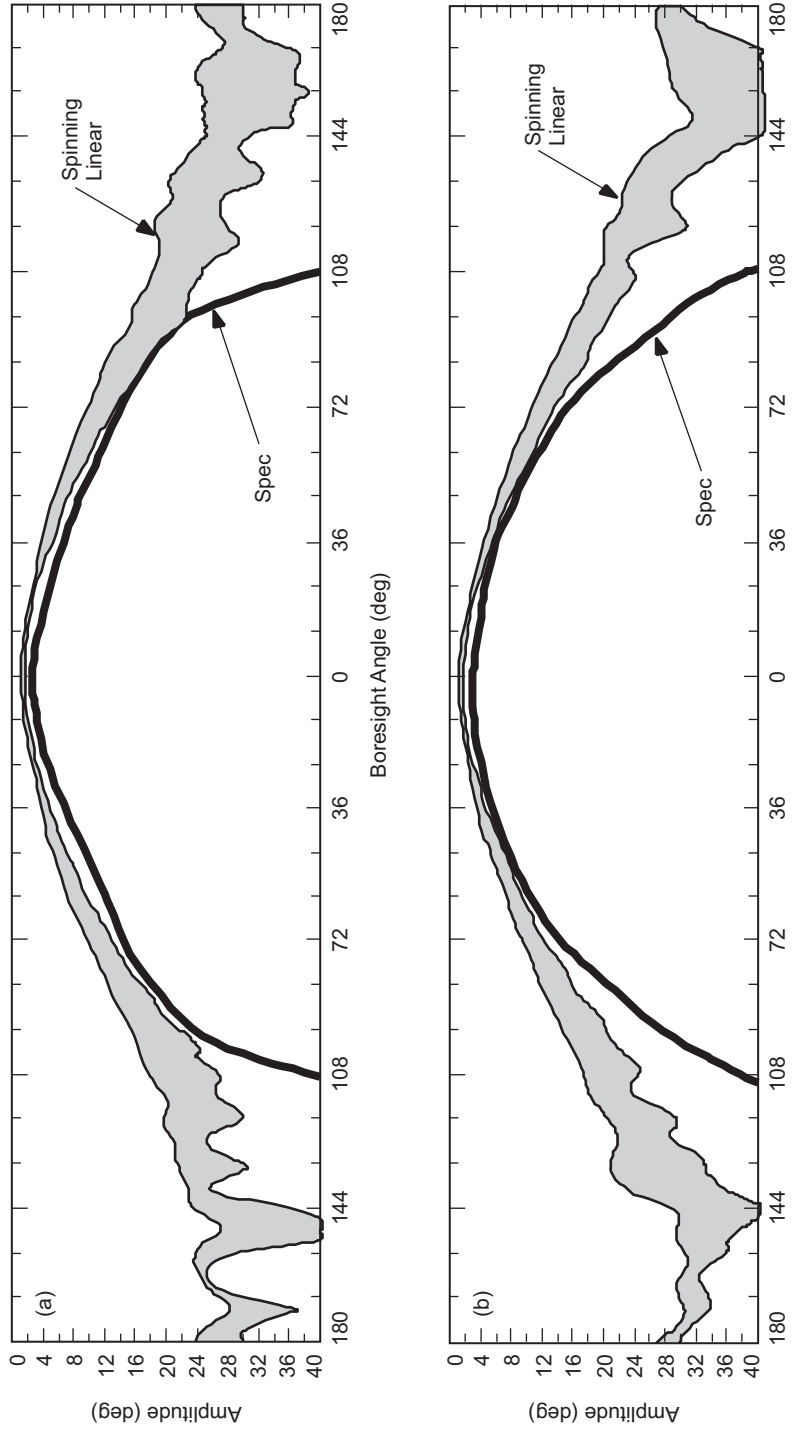
Fig. 5-24. Galileo LGA1 free-space pattern measured with a spinning linear probe compared to the required specification at (a) 2295 MHz and (b) 2115 MHz.

proper length by a ring that was empirically located by measurement of the VSWR and then soldered into place. Other parameters that could have been varied in the design of the antenna are shown in Fig. 5-26, and the parameter values selected after the design and breadboard testing are given in Table 5-7 [30,31]. The resulting far-field patterns are given in Fig. 5-27, and performance values are shown in Table 5-8. Finally, Figs. 5-28(a) and 5-28(b) are photographs of the spacecraft hardware as built.
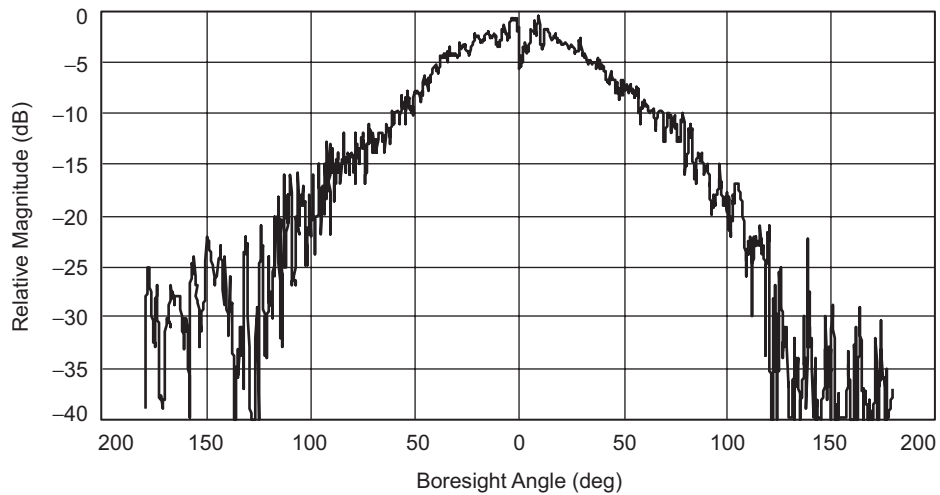
Fig. 5-25. Galileo LGA1 RF pattern in the presence of a 5-m reflector.
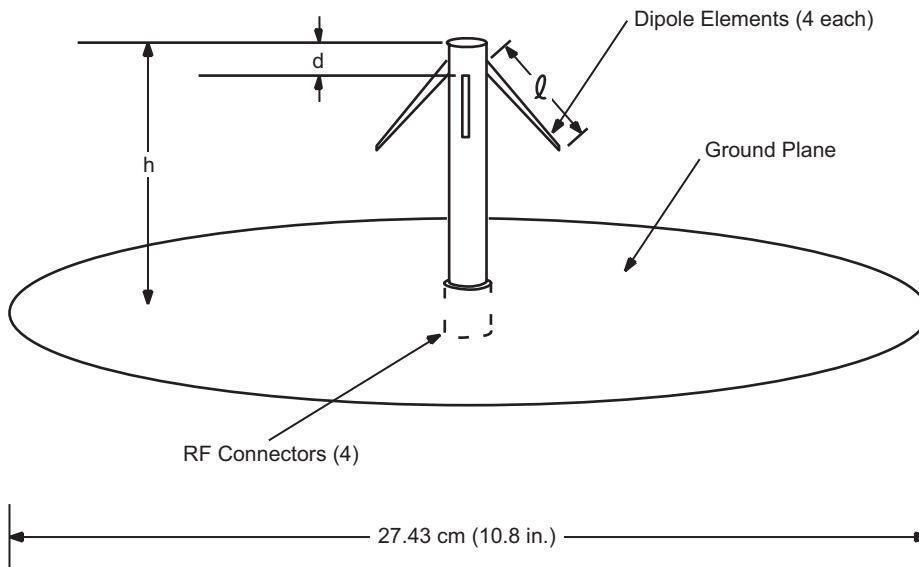
Fig. 5-26. Variable parameters of the Galileo LGA2.

Table 5-7. Values of the design variables for the Galileo LGA2.

Variable	Description	Dimension (in.)	Dimension (cm)
h	Post tip to ground plane	2.9	7.5
d	Post tip to dipole element	0.3	0.8
l_s	Length of short-dipole element	0.8	2.0
l_l	Length of long-dipole element	1.3	3.3

5.2.7.2.2 Articulated Spacecraft Mounting Boom. LGA2 was mounted on a mast that in turn was mounted on one of the RTG booms, as shown in Fig. 5-6. However, during the launch phase, the RTG boom was folded into the body of the spacecraft. Therefore, the LGA2 mast also had to be folded out of the way during launch. This was accomplished by a rotational motorized mechanism that swung from the mast in an arc from its stowed position to one that was pointed directly in the aft direction.

5.2.7.3 Performance of the LGA System Versus Requirements. The performance of the LGA system is illustrated in Fig. 5-29, where the gain patterns of LGA1 and LGA2 are shown relative to each other and to the requirements. It is apparent that the gain requirements were met for all but the very fewest directions centered about the 90-deg spacecraft angle. The spacecraft system engineering team analyzed the results, estimated the expected number of days that Earth would be in that direction, and determined that the results were satisfactory.

5.2.8   Conclusions

The 14-year Galileo mission came to an end at 11:57 a.m. Pacific Daylight Time (PDT) on Sunday, September 21, 2003, when the spacecraft was intentionally commanded to plunge into the atmosphere of Jupiter. (The reason for this action was because the onboard fuel was nearly expended and mission planners did not want to risk an unwanted impact with Jupiter's moon Europa. During its mission, the spacecraft received more than four times the cumulative dose of radiation that it was designed to withstand.) The DSN at Goldstone, California, received the last signal from the spacecraft at 12:23:14 a.m. PDT.

The Galileo spacecraft traveled approximately 4.7 billion kilometers, orbited Jupiter 35 times, and conducted the first long-term observations of the Jovian system. During this time, Galileo made the first observations of ammonia clouds in another planet's atmosphere; observed moon Io's volcanic activity, which may be 100 times greater than that of Earth; provided evidence

supporting a theory that a liquid ocean exists under Europa's icy surface; and showed that Europa, Ganymede, and Callisto each have a thin atmospheric layer [32].
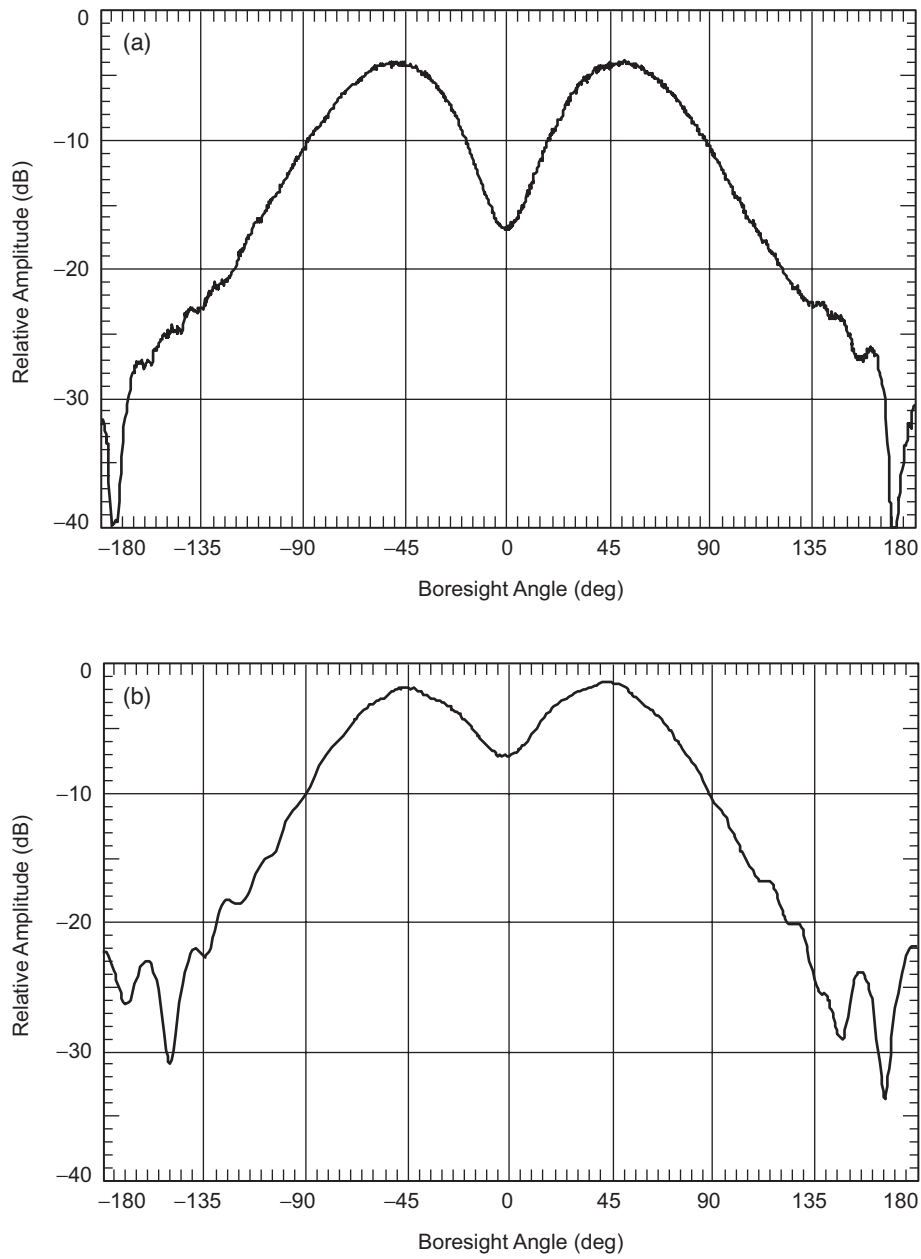
Fig. 5-27. Free-space far-field patterns of Galileo LGA2 at (a) 2295 MHz and (b) 2115 MHz.

Table 5-8. Galileo LGA2 performance measurements.

Parameter	Frequency = 2295 MHz		Frequency = 2115 MHz	
	Requirement	Measurement	Requirement	Measurement
Gain	≥4.5 dBi	5.3 dBi	≥4.0 dBi	5.3 dBi
Axial ratio	≤8 dB	≤11 dB	≤8 dB	≤7 dB
VSWR	≤1.30:1	1.23:1	≤1.30:1	1.22:1
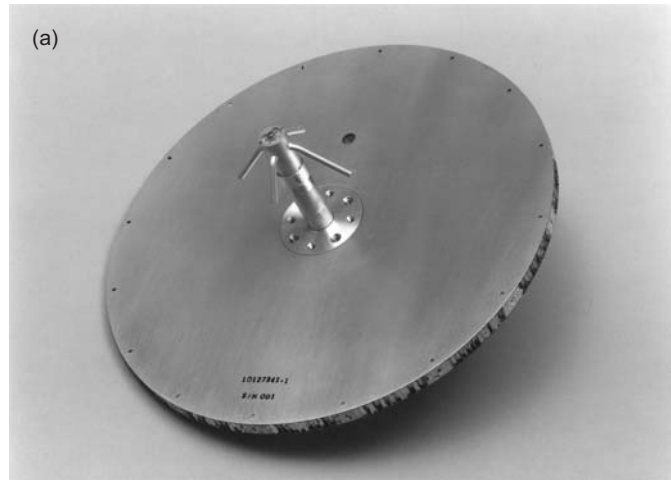
Fig. 5-28. Galileo aft-facing LGA2 for (a) front and (b) back.
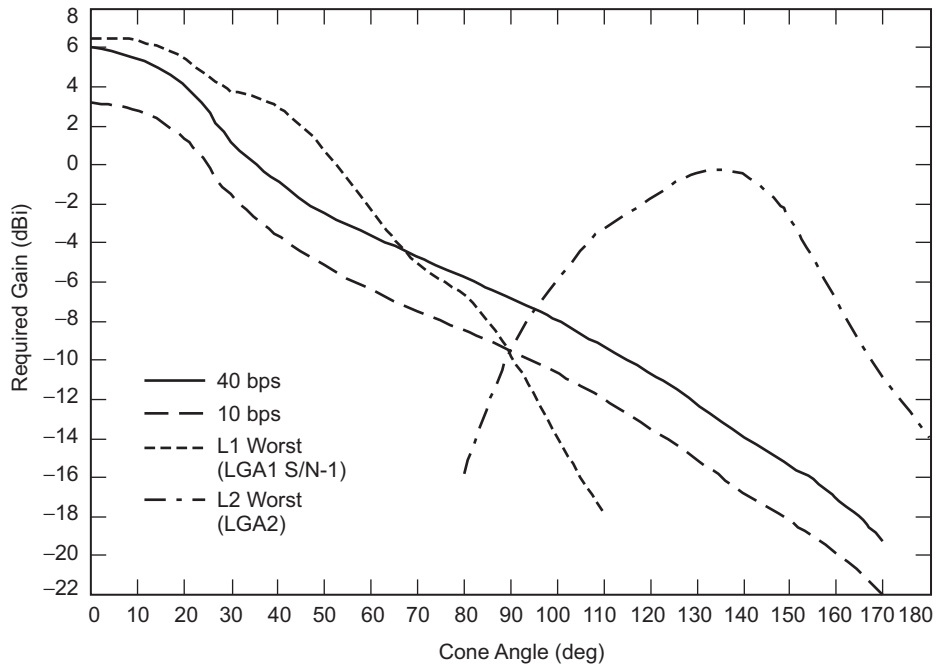
Fig. 5-29. Galileo LGA system performance vs. requirements.

During its entire life cycle, Galileo telecommunications were supported by only the LGA system of antennas. Had the HGA deployed as planned, the amount of discoveries might not have been greater, but the volume and quality of data would have no doubt been awe inspiring, given the more than 40 dB of gain between the HGA and LGA systems. The lessons learned from this project will be used in the development of future large deployable antennas that will be required in order for future missions to achieve the extremely high data rates that will be used to return scientific data.

5.3 The Cassini High-Gain Antenna Subsystem

Roberto Mizzoni, Alenia Spazio S.p.A, Rome, Italy

The Cassini-Huygens deep-space mission is a U.S.–European science program having as primary objective the exploration of Saturn and its largest moon, Titan [33]. The orbiter probe, launched in October 1997, arrived at the Saturnian system in July 1, 2004. Cassini's 4-year scientific mission at Saturn is dual: to complete a multispectral orbital surveillance of Saturn, and to investigate Titan. The U.S. Cassini orbiter, during its 74-orbit tour of the Saturnian system, will measure the planet's magnetosphere, atmosphere, and rings, and will observe some of its icy satellites and Titan during close flybys.

The Cassini's investigation of Titan was augmented by an instrumented European probe, called the Huygens Probe, which dropped through Titan's dense atmosphere on January 14, 2005. The Huygens probe reached the surface of Titan and transmitted data from there for 1 hour and 10 minutes before shutting down.

The Cassini data will be a major contribution to our scientific modeling of planetary atmospheres, important to our understanding of the evolution of Earth's own atmosphere. Cassini's multiple close flybys of Saturn's icy satellites also will provide insight into the nature of the population of small planet-like bodies that may once have been prevalent in the outer Solar System.

The mission, managed by NASA, is fully international in scope. The Huygens probe was provided by the European Space Agency, and elements of three of Cassini's science instruments were provided by the Italian Space Agency, along with the orbiter's HGA [34].

Cassini's orbit is shown in Fig. 5-30, and the spacecraft, at an intermediate integration phase at JPL, is shown in Fig. 5-31. The HGA (top) and the Huygens probe (side) can be seen on the spacecraft. The Cassini mission benefited from the gravity-assisted swing-bys of Venus, Earth, and Jupiter, without which it would be impossible to reach Saturn.

Cassini–Huygens is a three-axis stabilized spacecraft equipped for 27 diverse science investigations. The Cassini orbiter has 12 instruments, and the Huygens probe has six. The instruments often have multiple functions, equipped to thoroughly investigate all the important elements that the Saturn system may uncover. The spacecraft communicates through one HGA and two LGAs. It is only in the event of a power failure or other such emergency situation however, that the spacecraft will communicate through one of its LGAs, known as LGA1. This section describes the most important RF subsystem: the HGA.

5.3.1   High-Gain Antenna Requirements and Constraints

Table 5-9 summarizes the HGA–LGA1 modes and functions. Radio science experiments and radio relay linkage to the Huygens probe were allocated to S-band. Telecommunication is provided at X-band while radar imaging to Titan and altimetry of Titan are implemented at Ku-band. Precision Doppler experiments are done at Ka-band, to search for gravitational waves and measure relativistic bending of solar rays. Dual circular polarization is required at all bands except Ku, which is linear vertical (aligned with spacecraft motion). The HGA subsystem has a total of 11 physical ports, 5 of them diplexed at payload level, providing a total number of 16 input/output ports, while the LGA1 has got two Tx/Rx lines.

The top-level electrical parameters are summarized in Table 5-10, according to the operating frequencies detailed in Table 5-9.
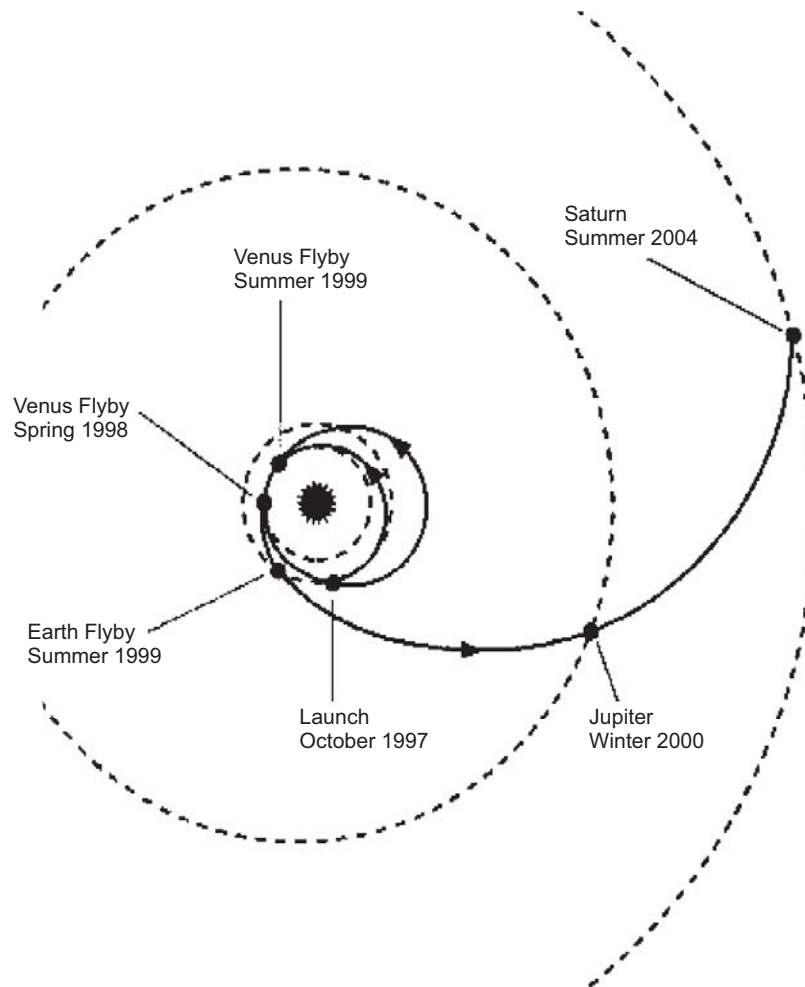
Fig. 5-30. Cassini journey to Saturn.

On-axis pencil beams are required at all bands, according to the beam scenario depicted in Fig. 5-32.

In addition, four fan beams (with five-to-one beamwidth ratio) are required for the radar imaging mode at Ku-band. Those beams form, together with the center pencil beam, a whole coverage line of about 5.8 deg along the range plane. Good cross polarization discrimination (<–20 dB), relatively low peak sidelobes (<–15 dB), a regular 3-dB contour (0.35 deg ±0.05 deg) in the along-track direction, and minimum gain along the range plane line (MGL) are important to SAR operation.

As an appropriate compromise between peak gain and spacecraft attitude control capability, the 3-dB beamwidth at Ka-band was required to be
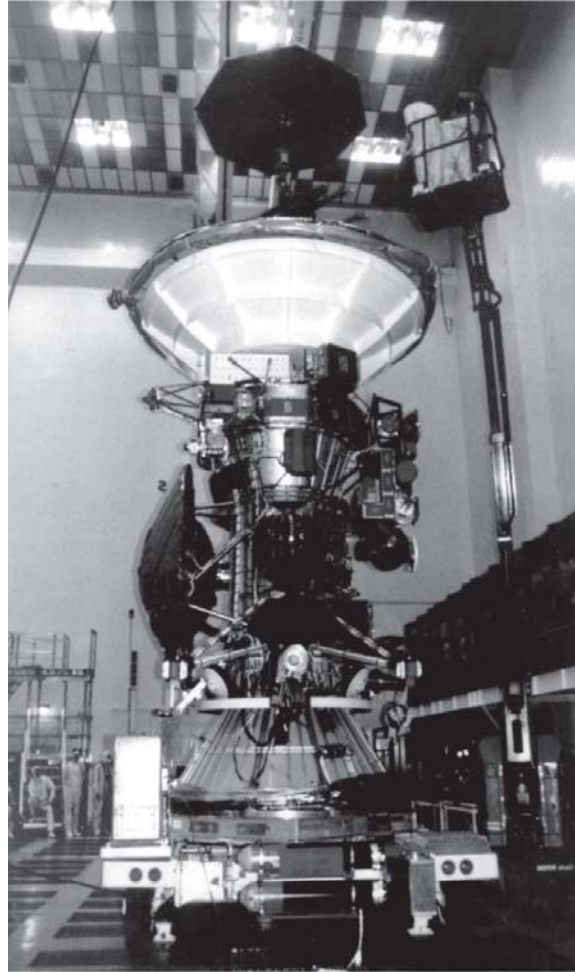
Fig. 5-31. Cassini spacecraft.

approximately 1.6 times larger that what is typical for the given aperture size. This then requires some form of beam-broadening at Ka-band. Maximum gain at the X-band downlink frequency is a priority in antenna configuration since the communication link is at the limit of feasibility.

The electrical design was heavily constrained by the launch vehicle envelope and the severe mechanical and thermal design requirements. This led to a symmetric dual-reflector antenna with a 4-m maximum reflector diameter and a focal length to diameter ratio lower than 0.33. Additionally, six thick struts were placed well inside the main reflector, to survive the dynamic loads at launch. The mechanical constraints and potential solutions are summarized in Table 5-11.

Table 5-9. Cassini HGA/LGA1 functions.

Antenna	Frequency (MHz)	Mode (*)	Function	Polarization
HGA	2040 ±5	R	Probe relay antenna	Circular, left hand
HGA	2098 ±5	R	Probe relay antenna	Circular, right hand
HGA	2298 ±5	T	Radio science	Circular, right hand
HGA	7175 ±25	R	Telecommunications	Dual circular
HGA	8425 ±25	T	Telecommunications	Dual circular
HGA	13776.5 ±100	T,R	Radar-SAR	Linear, vertical
HGA	32028 ±100	T	Radio science	Dual circular
HGA	34316 ±100	R	Radio science	Dual circular
LGA1	7175 ±25	R	Telecommunications	Dual circular
LGA1	8425 ±25	T	Telecommunications	Dual circular

* T–Transmit,   R–Receive

Table 5-10. Cassini HGA driving electrical requirements.

S-Band	X-Band	Ku-Band	Ka-Band
On-axis beam	On-axis beam	On-axis and off-axis beams	On-axis beam
Maximize peak gain	Maximize peak gain	Maximize MGL gain	Beamwidth 1.6 times larger than the physical aperture
Beam circularity	Dual CP operation	Minimize SLL	Dual CP operation
Dual CP operation		Minimize ISLR	
		Fan beam requirements	
		Linear polarization	

CP = circular polarization

ISLR = integrated sidelobe ratio

SLL = sidelobe level

5.3.2   Configuration Selection

The selected antenna configuration is shown in Fig. 5-33. The X-, Ku- and Ka-band subsystems are located at the Cassegrain focus of the dual-reflector system while the S-band feed system is located at the prime focus. The
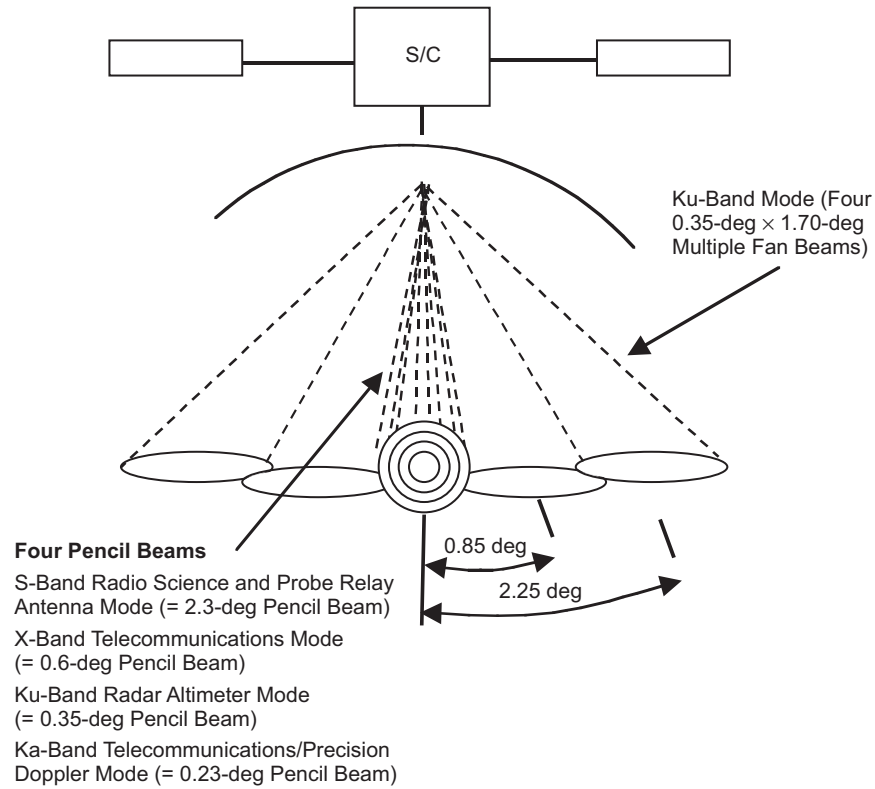
Fig. 5-32. Cassini HGA beam scenario.

Table 5-11. Cassini HGA mechanical/configuration constraints.

Parameter	Impact
Overall envelope	D <4.0 m, F/D <0.33
Spacecraft survivability	at 0.625 AU (Venus flyby), HGA Sun pointed (T_{ant} = + 160 deg C)
Antenna operation at 10 AU	Close to Saturn, T_{ant} = −210 deg C
Spacecraft/launcher envelope, interfaces, and loads	Center-fed antenna with 6-strut tripod inside main dish
Priority to X-band	X Cassegrain
Multiple-band operation	Wideband reflectors profiles, front feeds, Cassegrain feeds, FSS subreflector

T_{ant} = antenna temperature
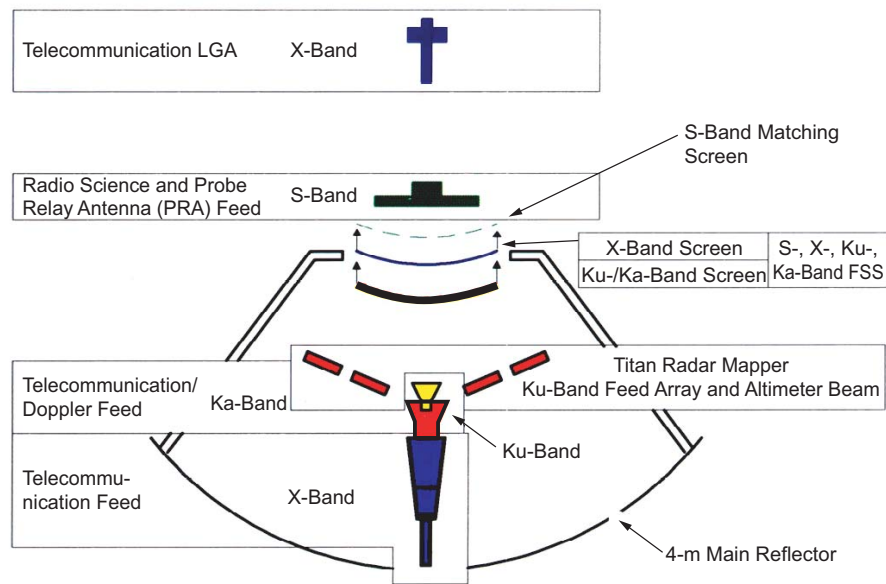
Fig. 5-33. Cassini selected HGA electrical/functional block diagram.

subreflector consists of a cascade of three frequency-selective surfaces separated by air. The first subreflector reflects Ku- and Ka-bands and is transparent at X-band. The second subreflector reflects X-band; the third subreflector is used as a matching screen to improve the overall transparency at S-band. A triple-band (X, Ku, and Ka) feed horn and 20 subarrays of slots grouped into four feed arrays of five elements each, operating at Ku-band, are arranged in the Cassegrain focal plane. For maximum coverage, the LGA1 antenna is on the top of the FSS deck.

Band allocation is dictated by the following considerations:

- X-band was Cassegrain located for maximum efficiency and minimal transmission line losses.
- Ka-band was Cassegrain located in order to avoid grating lobes from the FSS subreflector appearing in the visible space. This problem would be unavoidable if Ka-band operations were at the prime focus, considering the multiband operations. In addition, the high transmission line losses associated with a 3-m waveguide would not be tolerable at these frequencies.
- Ku-band was Cassegrain located after an extensive trade-off between a prime focus and a Cassegrain design. It was concluded that the scanning aberrations introduced by a prime focus configuration were not compatible with the sidelobe and beam-efficiency requirements for the

SAR beams (the most scanned element beam is about nine beamwidths displaced off-axis).

- S-band was located at the prime focus because the subreflector is less than four wavelengths at these frequencies and its feed aperture, of the same dimension, would be in conflict with all the other subsystems.

The selected optics geometry is shown in Fig. 5-34. It consists of a parabolic main reflector, a hyperbolic subreflector operating at Ku- and Ka-bands, and a shaped subreflector designed for X-band. Accordingly, two distinct foci are available at the X- and Ku/Ka-bands. The optics parameters are a good compromise between mechanical and technological requirements like the limited-feed axial extension and aperture dimension in the focal plane and a reasonable subreflector curvature for FSS manufacturing feasibility, as will be discussed later on.

Reflector profiles and the subreflector dimensions are constrained because the requirement for multifrequency operations. Thus, maximum performance at all the bands is not possible (see Table 5-12).
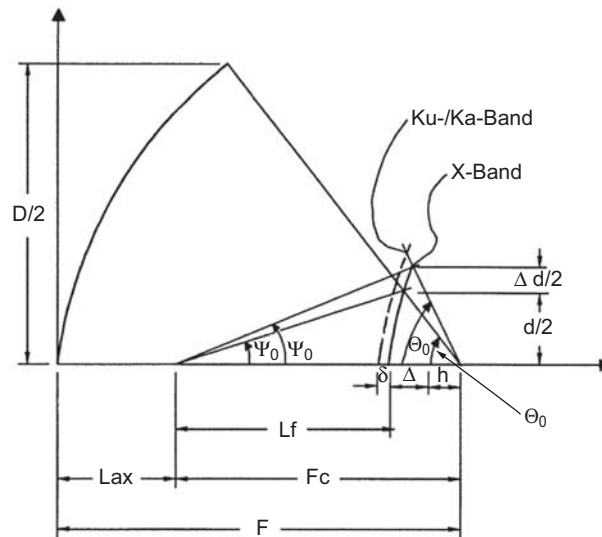
X-Band			**Ku-/Ka-Band**
F	=	1315 mm	1315 mm
D	=	4000 mm	4000 mm
d	=	463.5 mm	500 mm
$\Delta d/2$	=	53.4 mm	35.6 mm
$d + \Delta d$	=	571.2 mm	571.2 mm
Ψ'_0	=	16.15 deg	17.44 deg
Ψ'_0	=	18.9 deg	19.3 deg
Θ_0	=	74.5 deg	74.5 deg

Fig. 5-34. Selected Cassini HGA optics geometry.

Table 5-12. Cassini Optimum reflectors profiles vs. frequency band requirements.

Frequency Band	X	Ku	Ka	S
Best optical system	Dual shaped	Dual shaped	Dual shaped or equiv. 2.5-m reflector	Parabolic main
Viable alternative(s)	Hybrid (sub shaped, main parabola)	Canonical (hyperbola/ parabola)	• Smaller (or shaped) subreflector • Defocusing 4-m canonical optics	Main with any shaping
Main characteristics	• Deep (amplitude and phase) shaping • Recovery of feed taper on aperture • Frequency (feed) dependent	• Light (phase) shaping for homogeneous patterns in different beam directions. • Oversized sub-reflector	• Light shaping • Phase error for beam broadening and/or main reflector under-illumination at ka-band	• Front-fed • Back screen FSS profiled for optimum transparency • Oversized sub-reflector
Comment/ purpose	• Highest efficiency • Uniform aperture distribution	• Good η and scan performances • Low sidelobes	• 1.6:1 beam broadening	• Highest efficiency • Avoids sub-reflector scattering at edges

In particular, X-band would ideally use dual-shaped optics [35,36] for a nearly uniform aperture field distribution. Additionally, the feed/subreflector geometry would be dimensioned to satisfy the minimum blockage condition [37], for maximum antenna efficiency.

Ku-band optics is driven by the large scan of the fan beams (up to nine beamwidths of the element beam diffraction bounded by the aperture). The idealized optics would be a multifocal dual-shaped reflector system able to minimize beam aberrations due to scan within ±9 beamwidths along the range plane. As a good compromise, a canonical hyperbola and parabola dual reflector performs much better than the dual-shaped system required at X-band. At Ku-band, the subreflector has to be adequately sized in order to provide an efficient aperture illumination even for the most displaced feed element in the Cassegrain focal plane. To this end, the subreflector edges must lie well above the optical geometrical boundaries.

The Ka-band optics require a smaller subreflector than X- or Ku-band in order to under illuminate the main reflector, to yield a useful reflector diameter on the order of 2.5 m if a focused primary illuminator is used, since a beamwidth 1.6 times that physically achievable from the 4-m aperture is

requested. Alternatively, a dual-shaped system or shaped subreflector is required at Ka-band for beam broadening. In any case, the main reflector shape is not compatible with the X-band reflector shape while the subreflector shaping degrades Ku-band performance. The bottom-line alternative consists of a defocused approach realized by a proper axial displacement of the Ka-band feed phase center with respect to the canonical (hyperbola/parabola) optics. Although two distinct foci are available at the X- and Ku/Ka-bands, an independent optimization of the triple-band feed axial position within the optics, for the requested Ka-band beam broadening and the simultaneous optimization of the Ku-band altimeter beam, is not possible because the independent subreflectors relative displacements and shapes must be consistent with a stacked layout. Additionally, the phase center of the feed at Ku-band is between the X- and Ka-band phase center, and the fan-beam feed array should not to be obscured by the triple-band feed aperture. The net result is a small degradation of the Ku-band altimeter beam peak gain.

Finally, a prime-focus S-band feed would ideally require a parabolic main reflector, even if the RF performance were only second-order sensitive to the main reflector deviations, for any shaping of the main reflector or subreflector(s). For correct prime focus operation, the subreflector(s) should be dimensioned with boundary limits well above the optical geometrical boundary in order to minimize diffraction from the edges. Advantages of subreflector over sizing have also been illustrated for Cassegrain operations [38].

Considering all those arguments, the subreflectors have been properly sized above the geometrical boundaries (see Fig. 5-34) since only Ka-band would not benefit from this solution.

A careful assessment of the degrees of freedom of the optics was carried out considering additional options provided by the capability of FSS reflection bands. In particular, X-band in conjunction with a Ku-band reflection was investigated as a potential viable alternative to the present solution. This led to analyzing the performance capabilities at X- and Ku-band of dual shaped systems versus hybrid (only subshaped) and canonical hyperbola/parabola dual reflectors [39–41]. Efficiency enhancement for the on-axis pencil beam at X-band ranged within 0.6 dB (in comparison with a canonical system), but this spreading was sensibly reduced when the constraints on the maximum feed aperture size were imposed, owing to the SAR feed array [42]. For the selected design at X-band, the hybrid optics provides a peak gain improvement of 0.25 dB at the critical downlink frequency.

5.3.3   Antenna Modeling and Subsystems Design

A photo of the HGA/LGA1 flight model (FM) is shown in Fig. 5-35. The antenna is a carbon fiber composite structure with a thin sandwich reflector and back reinforcement ribs and rings (Fig. 5-35). The reflector shell is made by a

Fig. 5-35. Cassini HGA/LGA1 flight model.

lightweight sandwich, whereas the stiffening structure is a thicker sandwich. The tripod consists of six carbon-fiber-reinforced plastic (CFRP) struts having titanium end fittings connected to a Kevlar plate where the FSS subassembly, the S-band feed, and the LGA1 are mounted. The antenna mass including all RF subsystems is 103 kg, while the temperature range designed to was +160 deg C through –215 deg C.

As already anticipated, the antenna contains many complex RF subsystems, such as the FSS, a triple-band feed, and a slot-type array of 20 elements displaced in the Cassegrain focal plane.

Antenna design and performance prediction were complicated by several blocking structures inside the main reflector, including the six supporting struts of the FSS deck, the center blockage of the subreflector itself, and the asymmetrical blockage of the Cassegrain located feed assembly.

The computed main reflector geometrical optics (GO) shadow for a focused feed is illustrated in Fig. 5-36(a). It compares well to the experimental optical masking shown in Fig. 5-36(b).
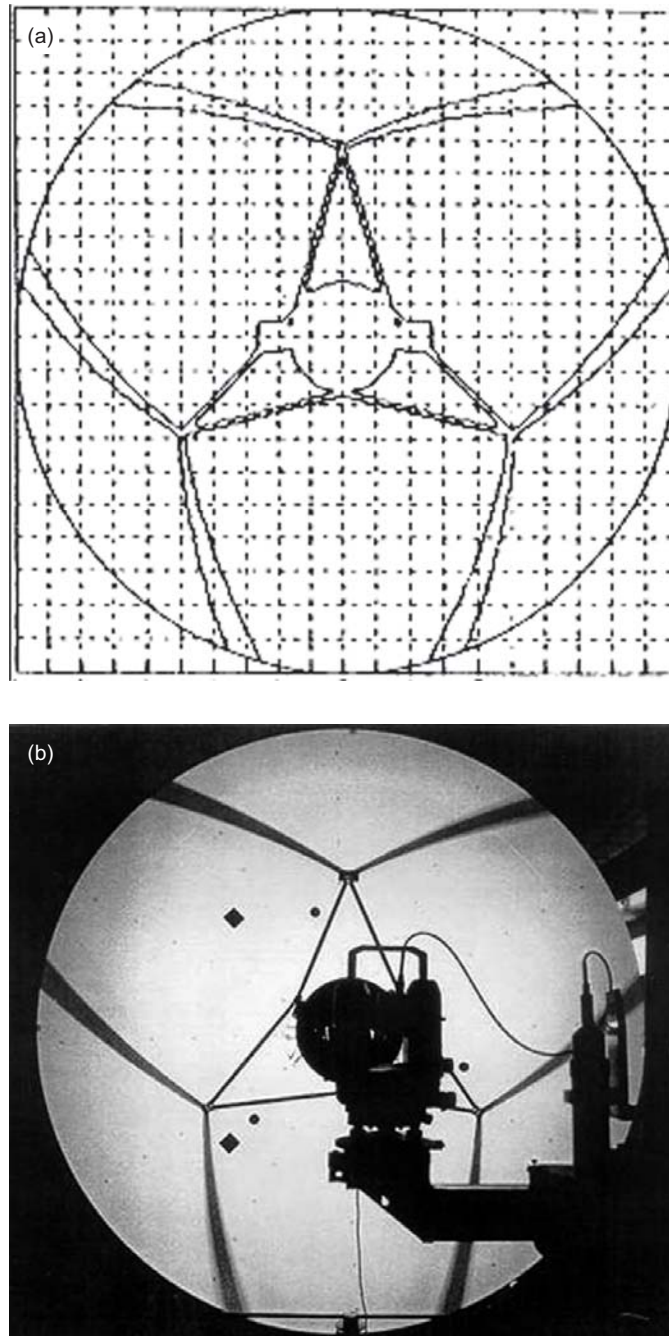
Fig. 5-36. GO shadowing of the Cassini main reflector aperture with (a) computed GO shadowing and (b) experimental optical masking.

The blockage mechanisms may be grouped into two main categories. The first—spherical-wave blockage (SWB)—is the blockage of the primary ray fields emanating from the prime-focus feed as well as from the virtual feeds. The second—plane-wave blockage (PWB)—is the blockage of the secondary ray fields reflected from the main reflector. At the time of design, the effects associated with PWB were already included in most of available reflector antenna software, such as GRASP [43], but no applications were available that dealt with SWB. SWB arises typically from the Cassegrain feeds and from the struts, which fall well inside the main reflector.

To compensate for this significant impact, customized electromagnetic (EM) software using the null-field approach [44], and a high-frequency description of the scattered field from the struts was developed [45] and validated [46]. The induced currents predicted in the physical optics (PO) approximation, were determined by the magnetic field $\mathbf{H}$ that effectively impinges on the main reflector surface. The field $\mathbf{H}$ is represented as the sum of the unperturbed field $\mathbf{H}^{\mathbf{i}}$ from the feeder plus the scattered field $\mathbf{H}^{\mathbf{s}}$ from the strut, so that, at any point, P, on the main reflector, the PO currents can be described as

$$J^{po}(P) = J^{poi}(P) + J^{pos}(P) \qquad (5.3\text{-}1)$$

where $J^{pos}(P)$ represents the current perturbation due to the struts, and $J^{poi}(P)$ are the currents that would ideally be induced by the feeder in the absence of the struts. In the null-field approach, the estimation of $J^{pos}(P)$ has been simply evaluated imposing $J^{pos}(P) = -J^{poi}(P)$ in the optically shadowed region, and zero elsewhere. The more accurate high-frequency (HF) formulation is detailed in [46].

The gain loss introduced by all the blockage impacts ranged between 0.4 and 0.8 dB at worst, moving from S- to Ka-band. The antenna model is also complicated by the FSS cascade, particularly at X-band, considering that a double passage through the first (Ku/Ka) screen is experienced, as schematically represented in Fig. 5-37.

At S-band, the subreflector is only a few wavelengths, and its dimensions are comparable to those of the feed aperture. As detailed below, the FSS cascade and the antenna analyses, including analysis of the dichroic subreflector were carried out using customized in-house software [47,48]. The modeling was based on accurate in-house data on the properties of RF materials (e.g., Kapton, Kevlar, adhesive). Accurate modal analysis for the evaluation of the scattering parameters of the dichroic structure was used. For the reflection bands, the radiation performance analysis of the curved surface was based on PO integration of the equivalent currents computed from the scattering
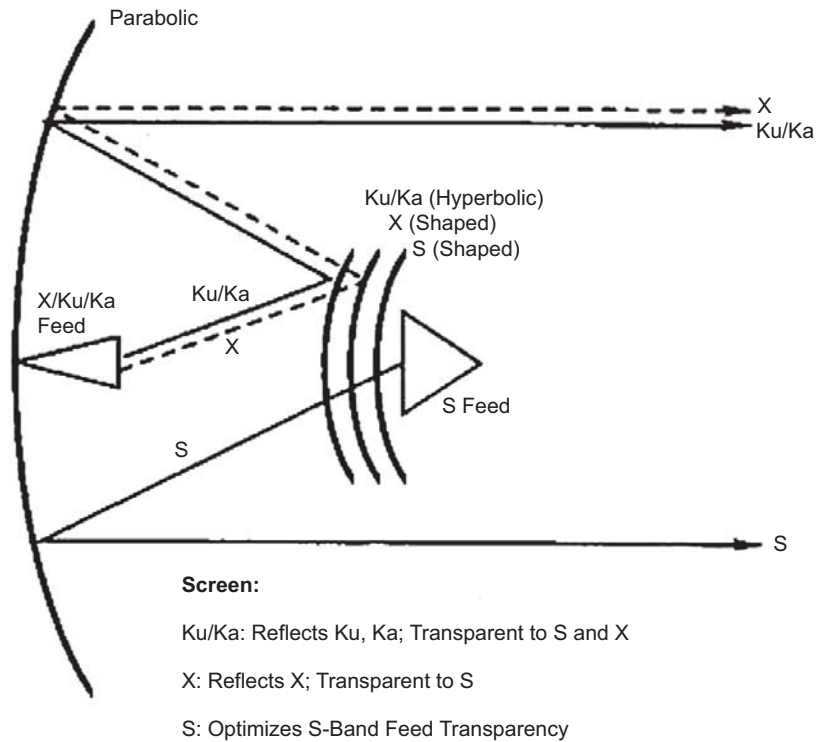
**Fig. 5-37. Schematic of double passage through
Cassini FSS cascade at X-band.**

parameters of the dichroic cascade, making use of the scattering coefficients evaluated at the Ku-/Ka-band front screen.

The development of all the RF subsystems, including that of the complete antenna itself, was experimentally supported by customized breadboards, as detailed below.

5.3.3.1 The Four-Band Subreflector. The subreflector, designed to be reflective at X-, Ku-, and Ka-bands and transparent at S-band, is composed of three mechanically independent surfaces (screens) mounted one behind the other at precise intervals (see Fig. 5-38) so that the required reflection and transmission bands are met [49]. Each FSS screen is separated and supported by a Kevlar honeycomb structure that provides rigidity. The Ku-/Ka-band screen, mounted topmost, is composed of a double periodic array of two concentric conducting ring elements etched onto a Kapton substrate. One element is designed to be closely resonant at Ku-band, and the other at Ka-band. The exposed surface is painted with a thermal protective layer that also acts as a ground. Single-ring resonating elements are employed on the

Fig. 5-38. Cassini FSS subreflector deck on HGA FM.

X-and S-band surfaces. This integration scheme was preferred to an alternative solution based on a Ka-band reflective front surface backed with an X-/Ku-band subreflector because it exhibited the lowest ohmic losses associated with the possibility of independently shaping the X-band subreflector in order to maximize the antenna gain at X-band.

From the structural point of view, the sandwich configuration forming each FSS had to be symmetrical, and each screen had to have an overall thickness greater than 4.5 mm [50]. Since the subreflector has a high curvature, a conformal transformation of the resonant elements was required. This implied the use of a regular square lattice since it had to be possible to cut the Kapton film containing these elements along parallel strips to allow forging them onto each mold, as illustrated in Fig. 5-39, where the Ku-/Ka-band screen on the assembly mold is shown.

Figure 5-40 shows the FSS computed transverse electric/transverse magnetic (TE/TM) reflection amplitude vs. frequency at 0-deg and 30-deg
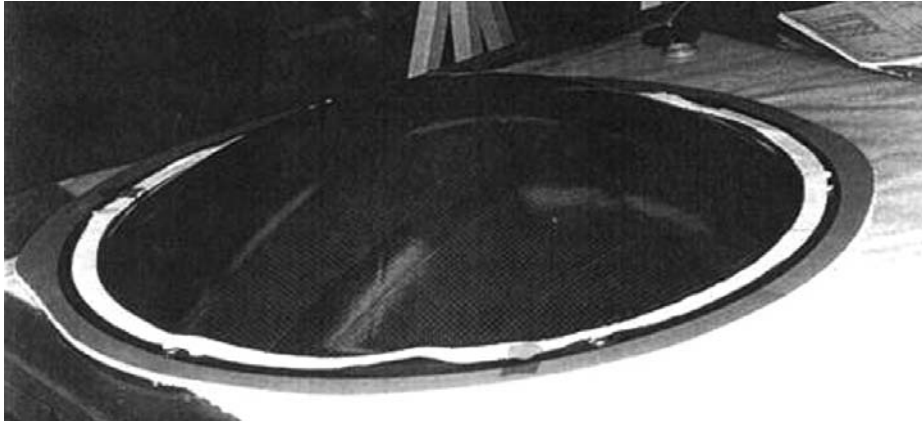
Fig. 5-39. Cassini Ku-/Ka-band FSS engineering breadboard on mold.
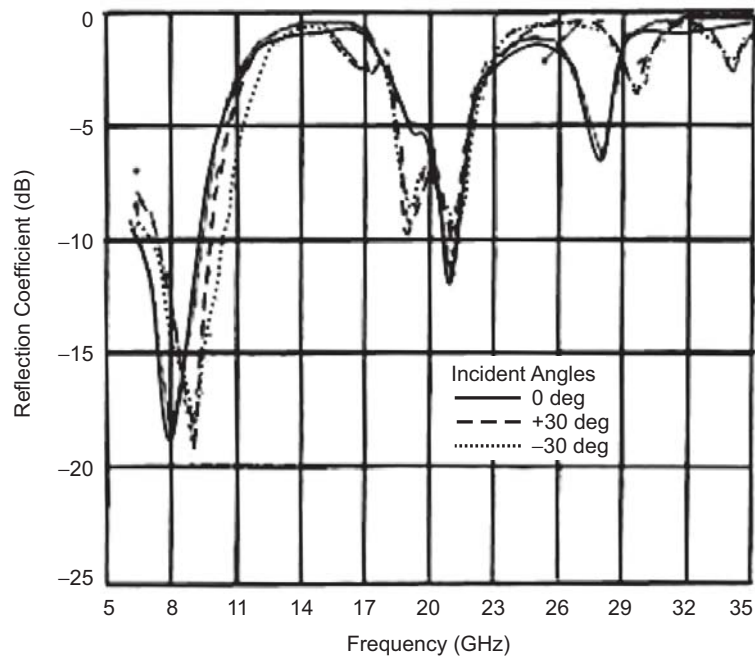
**Fig. 5-40. Cassini Ku-/Ka-band FSS TE/TM reflection performance
vs. frequency at 0-deg and 30-deg incidence angles.**

incidence angles, referred to the Ku-/Ka-band front screen. A good transparency at X-band downlink frequency was obtained.

Although the whole subreflector is composed of the three independent reflectors, their design is not independent. At X-band, the response is a result of the constructive interference between the signal reflected by the back X-band

screen, after having been transmitted through the front Ku-/Ka-band screen, combined with the residual reflection caused by the Ku-/Ka-band screen. The ideal X-FSS would be profiled to optimize its distance from the Ku-/Ka-band FSS so as to achieve this interference as close as possible to the nominal shape dictated by the idealized shaped metallic subreflector relevant to the nominal optics. The method, which led to the definition of the optimum X-band screen shape, involved first calculating the TE/TM response of each individual screen and then cascading them to obtain the performance versus separation response of the two screens for a given incident angle. The analysis at X-band makes use of the scattering coefficients equated at the Ku-/Ka-band screen surface. The unified scattering matrix (USM) obtained using the cascading process mentioned took into account the actual separation between the Ku-/Ka- and X-band screens for each incident angle analyzed. Figure 5-41 shows the calculated S_{12} amplitude of TE/TM modes vs. X-/Ku-band, Ka-band screen separation at 0-, 30-, and 45-deg incidence angle at the downlink frequency of 8.425 GHz. From the figure it is evident that an optimum separation between the two screens, close to 4 mm at 0 deg is the best choice, but at 45 deg their separation must be doubled.

At S-band, the transmission was not optimal because the Ku-/Ka- and X-band screens were not completely transparent. For this reason, an S-band screen was used to impedance-match the response of the whole structure. This
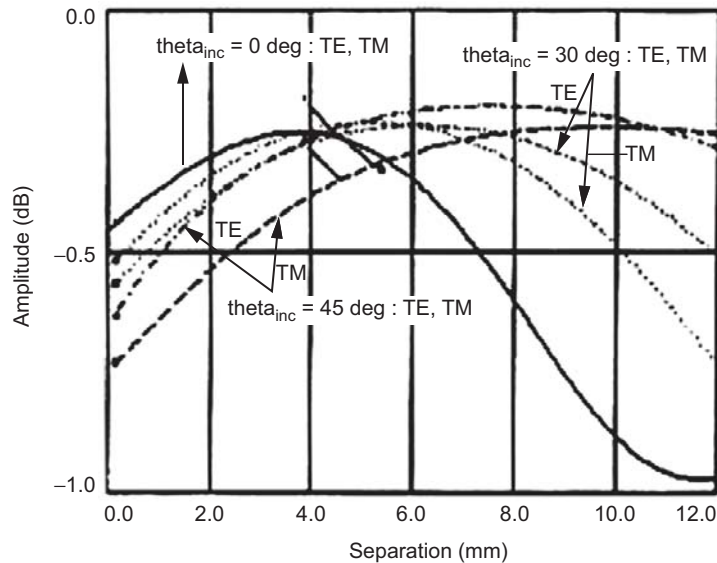
**Fig. 5-41. Computed combined transmission vs. separation between Cassini X-band screen and Ku-/Ka-band screen at 0-, 30-, and 45-deg incidence angles (F = 8.425 GHz).**

was achieved in the same way as for the X-band transmission although this time, of course, all three screens were cascaded to obtain the S-band screen shape that best optimized the transmission at S-band for radio science. The design curves at 2.3 GHz are illustrated in Fig. 5-42, where the S_{11} amplitude of TE/TM modes at 0-, 15-, and 45-deg incidence angles relevant to the three frequency selective subreflector cascade, is displayed. Figure 5-43 shows the final optimum subreflector profiles where, for practical reasons, the idealized spacing had to be compromised. Figure 5-44 shows the computed vs. measured amplitude and phase at the feed subreflector level.

FSS performance at ambient temperature was verified by (1) flat waveguide sample tests (S-parameter tests), (2) subassembly feed-subreflector tests (radiation performance and pattern integration), and (3) complete antenna tests (pattern and gain with regard to a metallic (for complete reflection) or no (for complete transmission) subreflector. The results, including losses due to the white paint, are summarized in Table 5-13.

In this table, the amplitude and phase-loss data, caused by the FSS subsystem, refers to the complete antenna. The losses were derived by using the experimental pattern of the subreflector subassembly in the antenna analysis at
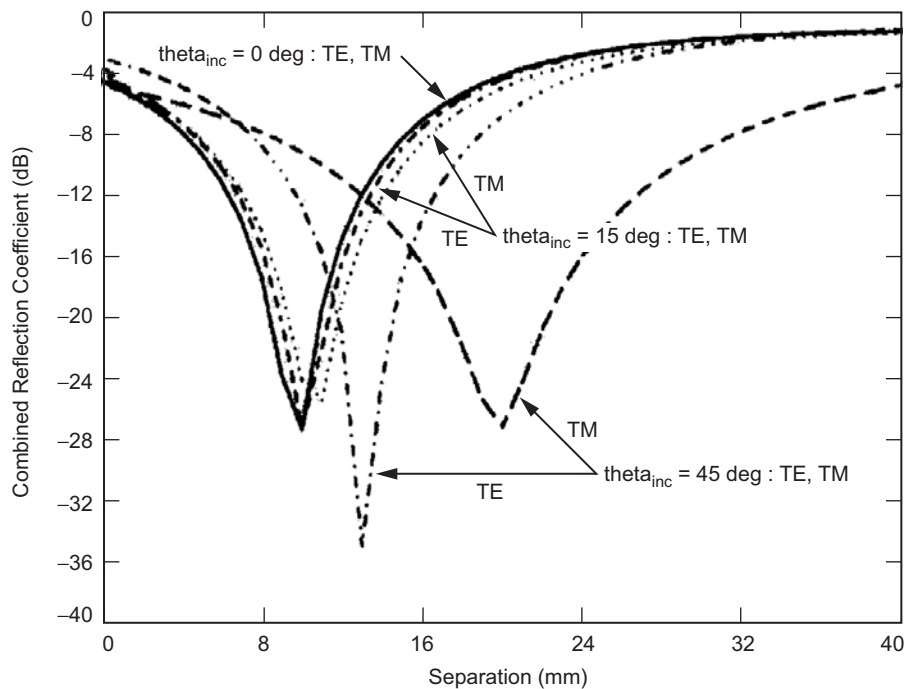
Fig. 5-42. Computed combined reflection vs. separation between Cassini S-band screen and combined X+Ku-/Ka-band screens at 0-deg, 15-deg, and 45-deg incidence angles (F = 2.298 GHz).
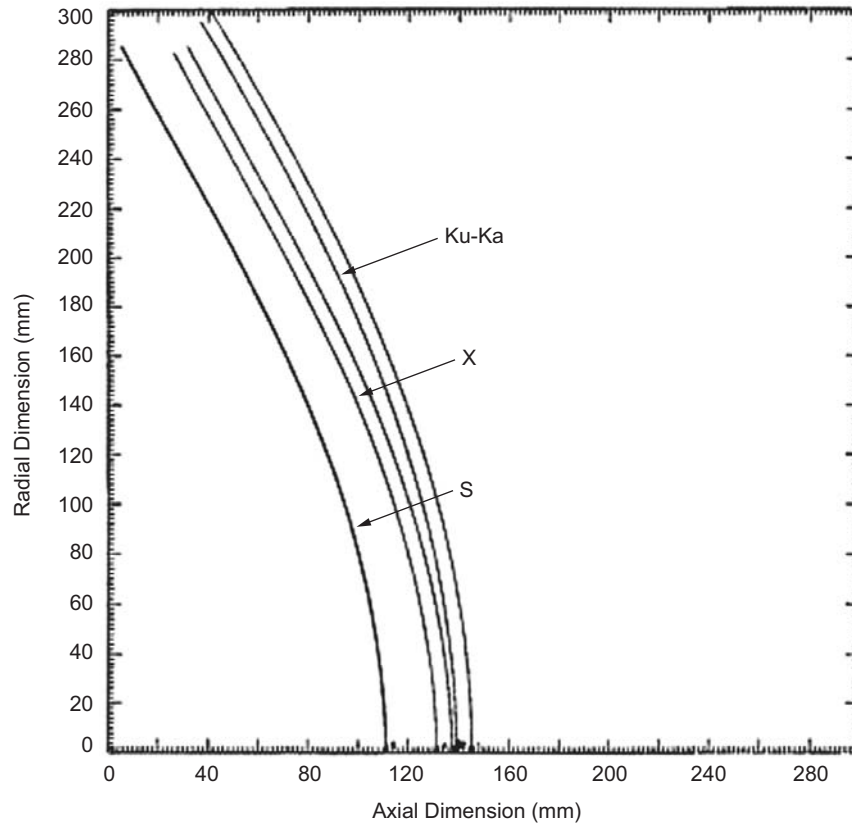
Fig. 5-43. Cassini subreflector profile (front and back layers for X-band and Ku-/Ka-band).

the secondary level. The ohmic losses were evaluated by pattern integration. The discrepancy between the results at subsystem level with regard to the tests at antenna level were consistent with the measurement accuracy.

FSS verification at cryogenic temperature (<-180 deg C) was conducted using innovative-waveguide [51] and free-space radiation [42] test methods that allowed the setup calibration and the relative measurement with respect to ideal samples in the thermal-vacuum environment. Figure 5-45(a) shows a schematic of the radiation setup.

Tests were performed using an ellipsoidal subreflector to produce a locally plane wave front to minimize the reflections from the environment. The radiating feed was placed at one of the foci. A specially designed rotating turret allowed a metallic plate and the FSS sample to be positioned at the other focus. Switching from the metallic to the FSS sample could be done at the measurement temperature since the entire assembly was placed within the thermal vacuum chamber. Considering the relative phase length between the
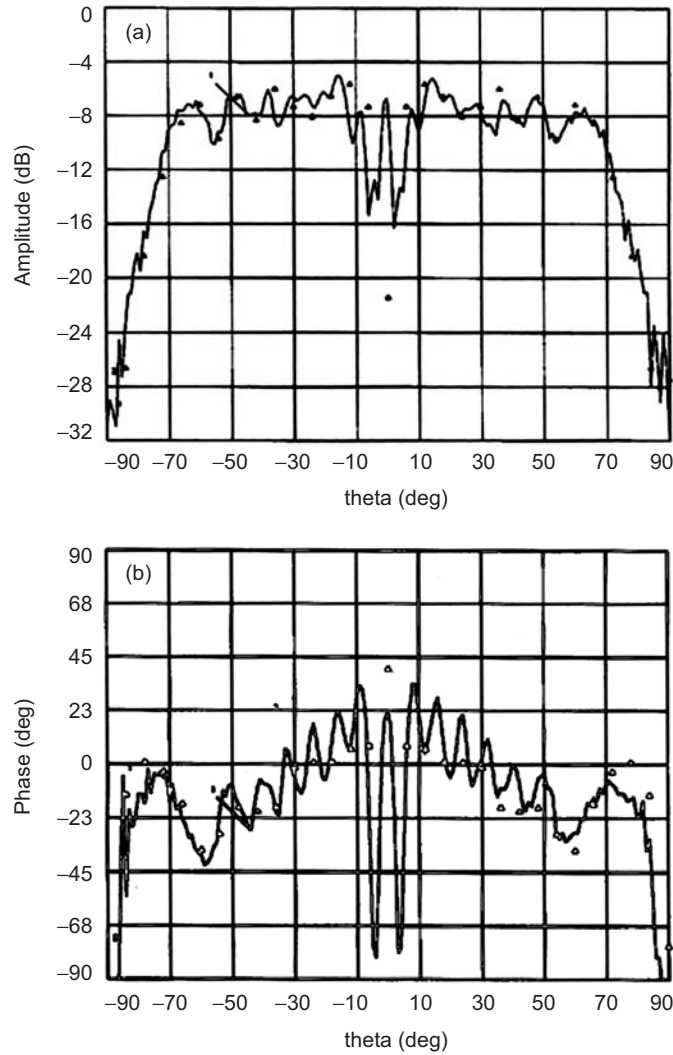
Fig. 5-44. Cassini computed (lines) vs. measured (dots) patterns at X-band of FSS subreflector cascade for (a) amplitude and (b) phase.

sample and the feed, time gating could be efficiently used to improve the measurement accuracy.

The experimental radiation setup is shown in Fig. 5-45(b). Results show a reduction in the ohmic loss of the substrate material and a decrease in the resistivity of the metallic resonant elements. The loss reduction can be explained by both a reduction in the loss tangent of the sandwich material (Kevlar and glue) and to an increased conductivity of the metals used as resonating elements.

Table 5-13. Measured Cassini FSS cascade performance relative to ideal subreflector(s).

Frequency (GHz)	At Subsystem Level		On Antenna Level	Discrepancy (dB)
	Ohmic + T/R* Loss (dB)	A & φ Loss (dB)	Total Loss (dB)	
2.040	0.26	0.14	0.5	+0.10
2.298	0.16	0.0	0.2	+0.04
7.175	0.51	0.08	0.8	+0.21
8.425	0.23	0.16	0.6	+0.11
13.7765	0.65	-	0.6	–0.05
32.028	0.55	-	0.6	+0.05
34.316	0.89	-	0.8	–0.1

*T/R transmission/reflection

This causes a marked improvement in the overall performance of the FSS at operative temperature (–200 deg C). Figure 5-46 shows the results of the radiated test on flat-panel samples (X + Ku/Ka FSS) at ambient and –180 deg C. The reduction in the loss of the FSS (–0.4 dB), with respect to the metallic reference at –180 deg C, is clearly visible.

This loss reduction is particularly evident at X-band, where the double passage through the K-band screen is experienced. At the highest frequencies (Ku- and Ka-bands) that involved only the first screen, the loss reduction is less (0.2 dB to 0.1 dB, respectively). The FSS structure was also seen to be reasonably stable in response to variation in the material and element tolerances.

5.3.3.2 The Triple-Band Feed. The triple-band feed is a dual-depth corrugated horn operating in dual circular polarization at X- and Ka-band and in linear polarization at Ku-band. The feed provides a Gaussian-like primary pattern for the generation of on-axis pencil beams at X-, Ku-, and Ka-bands [52]. The feed aperture is limited by the feed arrays of the Ku-band fan beams (see next section). The internal layout of the feed is shown in Fig. 5-47(a).

Tapered and suitably designed dual-depth corrugated sections of circular waveguides compose the main transmission line. X- and Ku-band signals are introduced at appropriate cross-sections of this line by a set of four transverse slot-coupled rectangular branch waveguides. The four branches are symmetrically arranged on the circumference of the line, thus permitting any state of polarization to be achieved through a suitable external network. Ka-band is end-launched into the line while the other end gradually flares into a dual-depth corrugated horn.
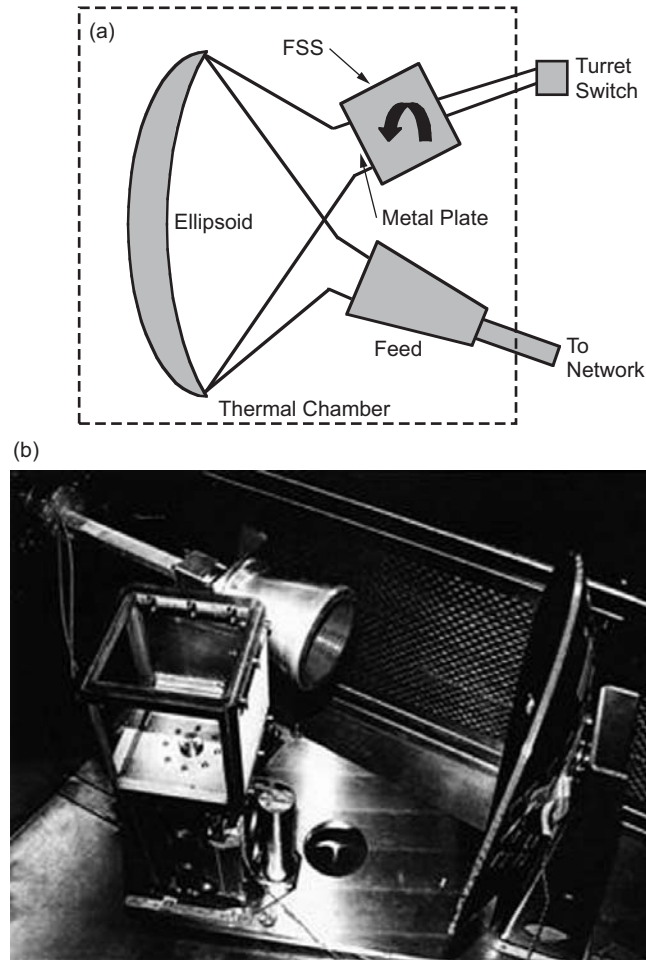
Fig. 5-45. Cassini FSS samples radiation set-up:
(a) schematic and (b) photograph.

To achieve optimum simultaneous performance in three widely separated bands important design considerations are:

1) Suitable dual-depth corrugations to meet balanced hybrid boundary conditions simultaneously for Ka-, Ku-, and X-bands.

2) Radial line chokes in the X- and Ku-band transducers to isolate Ka-band as well as to minimize overmoding in the main transmission line at Ka-band.

3) Tapered sections to provide appropriate phasing of the signals at the X- and Ku-band transducers, as required for optimum coupling.

4) Independent tuning parameters in the form of step discontinuities in the rectangular branch waveguides of the X- and Ku-band transducers.
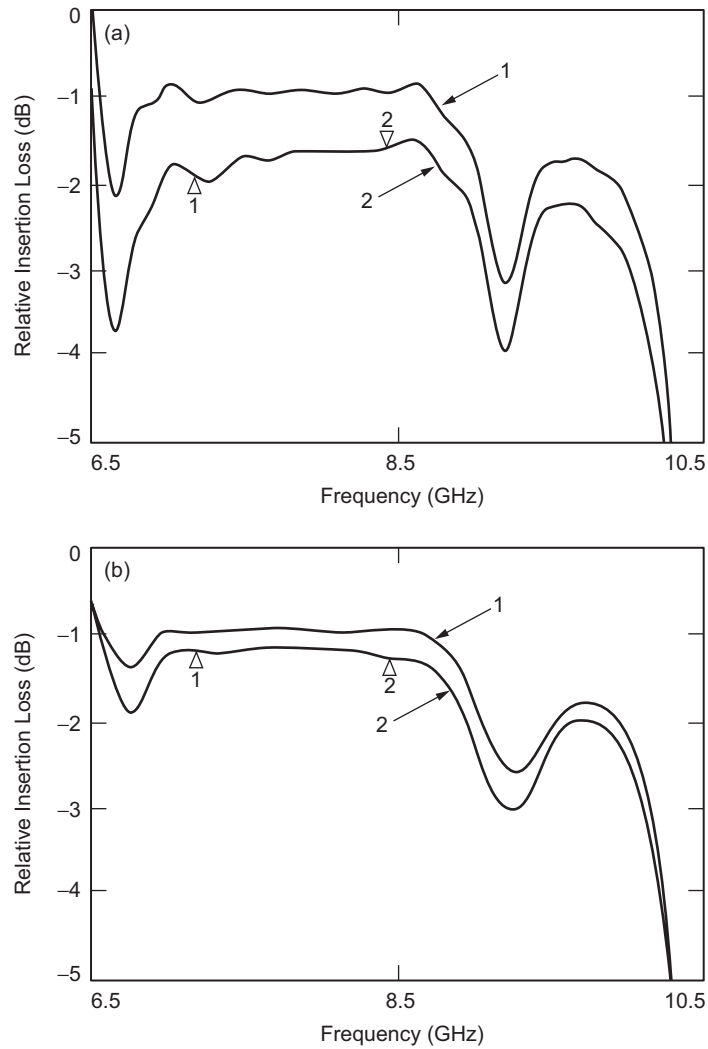
Fig. 5-46. Cassini FSS radiated test showing differential insertion loss at X-band: (a) ambient temperature and (b) at −180 deg C. Trace 1: metallic sample; Trace 2: FSS sample.

Analysis of the entire feed was done by following proper segmentation and cascading procedures. Efficient and accurate moment-method codes were used to compute the generalized scattering matrices of the segmented discontinuity modules, which were then connected in tandem by the cascading procedure to obtain the final scattering response of the integrated feed system. Radiation patterns were computed from the modal field amplitudes at the feed aperture after accounting for the fringe currents on external feed geometry whenever appropriate [52].
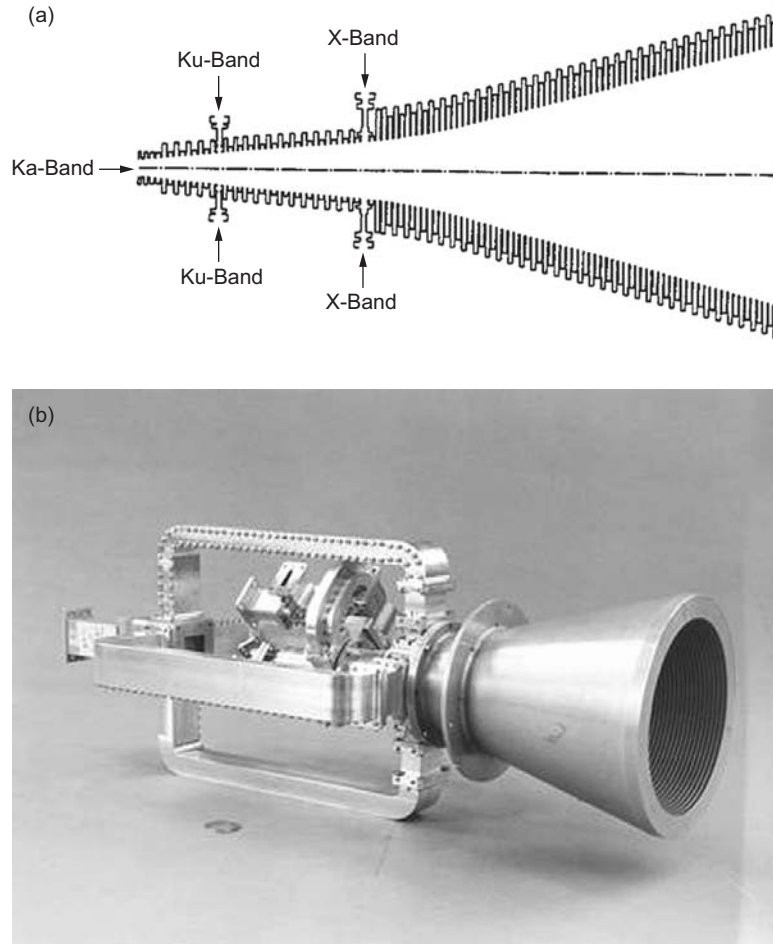
**Fig. 5-47. Cassini X-/Ku-/Ka-band self-diplexed feed system
(a) schematic view and (b) engineering breadboard model.**

The complete feed breadboard model is shown in Fig. 5-47(b). The external microwave network at X-band consists of a septum polarizer in cascade with a radial four-port orthomode transducer (OMT). The four output arms of the OMT are connected to the four branches of the X-band feed diplexer. The Ku-band network required a 0–180-deg feeding hybrid, which was achieved by configuring a 3-dB (H-type) branch guide coupler in cascade with a 90-deg stub-type phase shifter. Ka-band dual circular polarization was achieved at the end-launched feed interface by adding an appropriate polarizer. The hardware selected for the external microwave networks guaranteed the minimum envelope in combination with the lowest insertion loss at the three bands. The feed electrical characteristics were evaluated using test setups calibrated with a

Hewlett Packard HP8510 automatic vector network analyzer for the return loss and RF isolation characteristics, and a well-equipped near- and far-field anechoic chamber for the radiation pattern measurements.

The feed exhibited high diplexing capability (>40 dB). An excellent agreement between experimental and computed RF performance was found, as illustrated in Fig. 5-48, where the primary patterns are shown.

5.3.3.3 Ku-Band Fan-Beam Subsystem. The four fan beams are generated by 20 shunt-slot subarrays grouped into 4 feed arrays each containing 5 subarrays. Each subarray was axially moved toward the subreflector in order to optimize gain and minimize scan aberrations at the element-beam level. The staircase arrangement of the slot subarrays can be seen in Figs. 5-49(a) and (b), which show the entire feed subassembly, including the triple band feed of the flight model (FM) unit and the standalone slot array on the support prior to its integration.

The 20 identical subarrays consist of five waveguides of two slots each [53]. Each waveguide is series slot fed at the center of the waveguide. In order to maximize the overlap among the adjacent element beams, a uniform distribution was synthesized along the H-plane while a Chebycheff 30-dB level sidelobe was specified along the E-plane for a minimum primary spillover and optimum far-out sidelobe level.

The subarray synthesis was carried out by using an accurate modal analysis code [54]. A detailed experimental/theoretical iteration was necessary in order to converge toward the desired sidelobe level. Corrections to the feed slot geometry were achieved with the aid of a self-impedance chart of the feeding network slot. The radiation pattern performance of the subarray was evaluated taking into account the edge effects through a geometrical theory of diffraction (GTD) model of the planar array.

Subarray performance in the feed array environment could be altered by mutual coupling and scattering among adjacent elements. Considering the aperture dimension and the relative staircase arrangement, this latter factor was recognized to be very important. In particular, a first-order impact arises from the adjacent front displaced subarray since it is in the direct radiation field of view of the back subarray. Therefore, a GTD model of this geometry was simulated. Since the subarrays had different axial displacements, this analysis was repeated for each subarray.

In Fig. 5-50, a comparison of one typical experimental pattern is overlaid on the computed one. These primary patterns were used in the fan-beam synthesis. Regarding the beam-forming network behind each feed array, a compact layout was realized by corporate feeding of the five subarrays using an integrated 10-port divider of branch-guide type to minimize mass and losses. The pattern synthesis was based on an accurate software modeling analysis; and therefore, no experimental tuning was required [55].
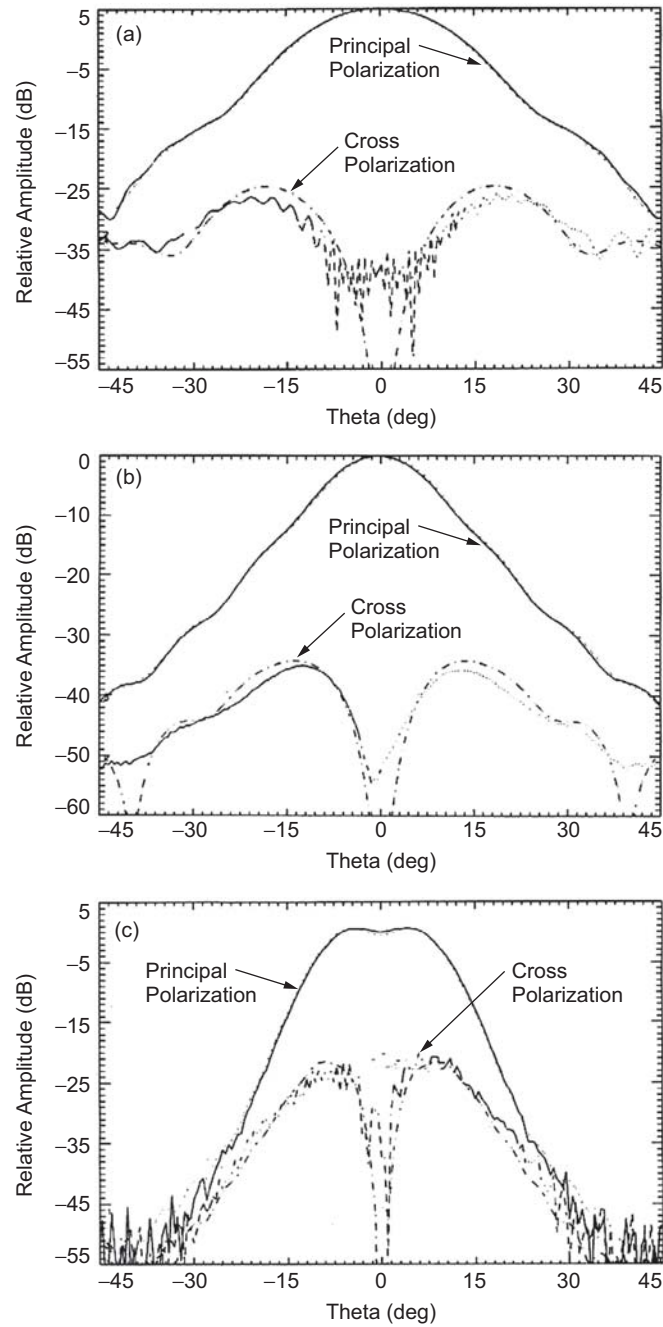
Fig. 5-48. Cassini computed (dotted line) vs. measured (continuous line) radiation patterns: (a) 8.425 GHz, (b) 13.8 GHz, and (c) 32.0 GHz.
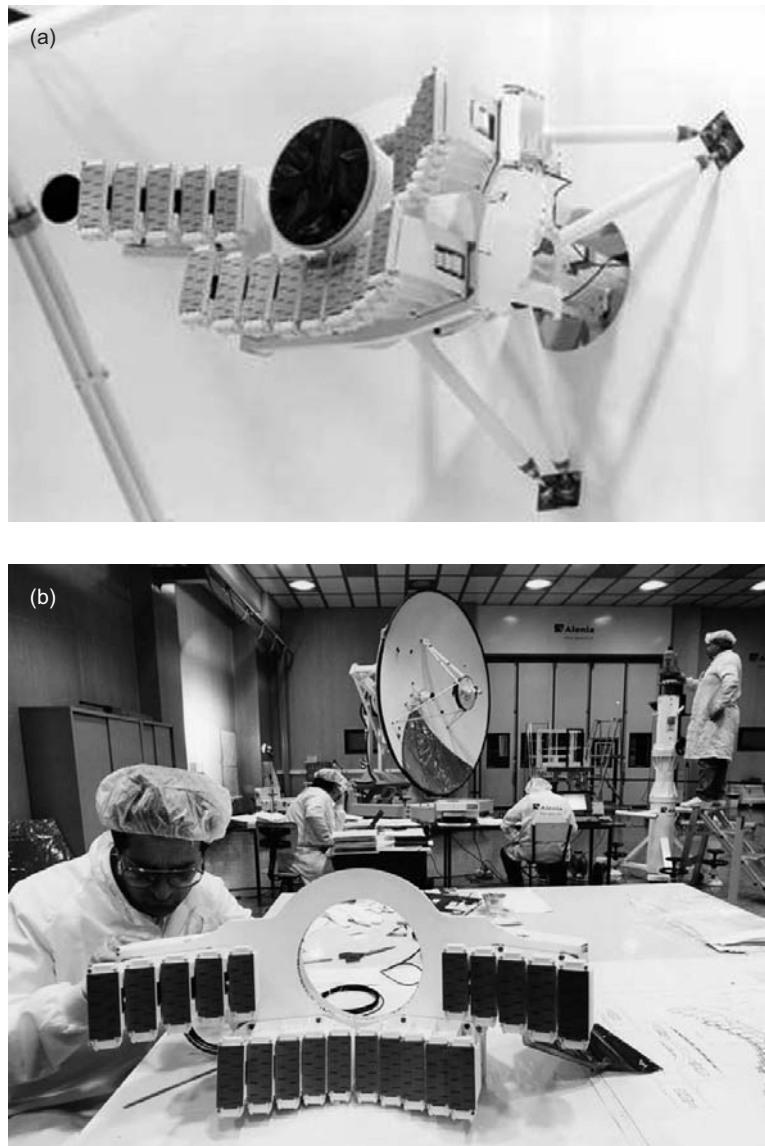
Fig. 5-49. Cassini feed system: (a) complete X-/Ku-/Ka-band feed system in the Cassegrain focal plane and (b) details of the Ku-band slot feed arrays.

5.3.3.4 S-Band Feed. The S-band feed was designed to provide a secant-squared radiation pattern in order to enhance the antenna efficiency for the short focal-length design [56]. The feed is a coaxial horn with a cylindrical waveguide and two external parasitic rings (Fig. 5-51(a)). The feed network and
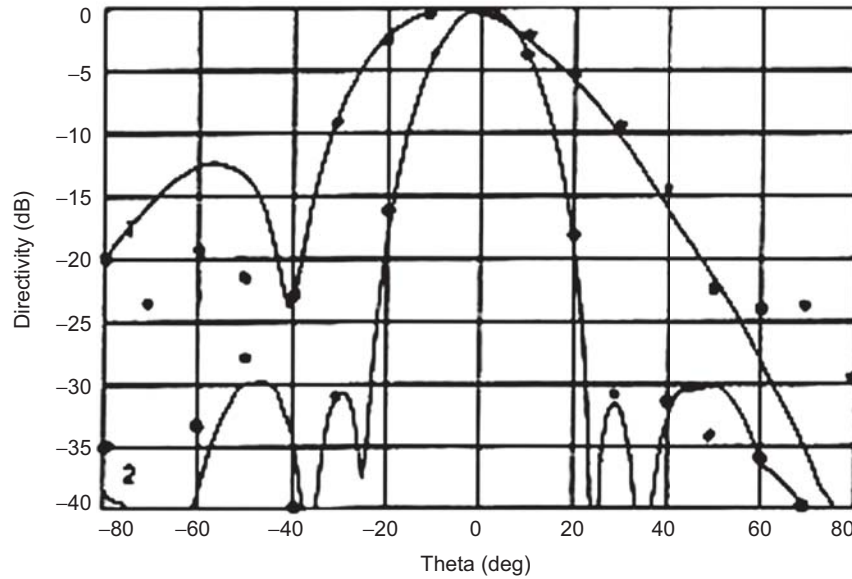
Fig. 5-50. Cassini Ku-band sub-array pattern in the feed-array environment (center element of B1/B5). E-, H-planes: ▬ experimental ● theoretical.

probes were made using bar-line technology (see Fig. 5-51(b)). Radiation pattern performance at the radio science frequency is shown in Fig. 5-52.

5.3.3.5 Low-Gain Antenna 1. LGA1 consists of a cylindrical waveguide with several external corrugations shaped and profiled to minimize back radiation. In Fig. 5-53, several options are illustrated. The selected configuration is shown in Fig. 5-54. The LGA1 pattern measure on the FM HGA–LGA1 antenna assembly, installed on the top of the FSS deck, for maximum coverage extension, is shown in Fig. 5-55.

5.3.4   Antenna Performance at S-Band

The S-band feed is in a prime focus configuration and has a relatively wide bandwidth. Computer modeling at feed-subreflector level showed that in order to maximize the gain throughout the bandwidth, the back FSS screen needed a thickness that varied according to incidence angle; however, variability in thickness has not been implemented in this configuration. Additionally, the parasitic coaxial feed was band-limited because, in the selected design, priority was assigned to the radio science frequency (2.3 GHz). The optimum design at 2.3 GHz was confirmed by differential on-axis gain measurements (with and without FSS), which exhibited an overall loss of about 0.2 dB at 2.3 GHz and 0.5 dB at 2.040 GHz.
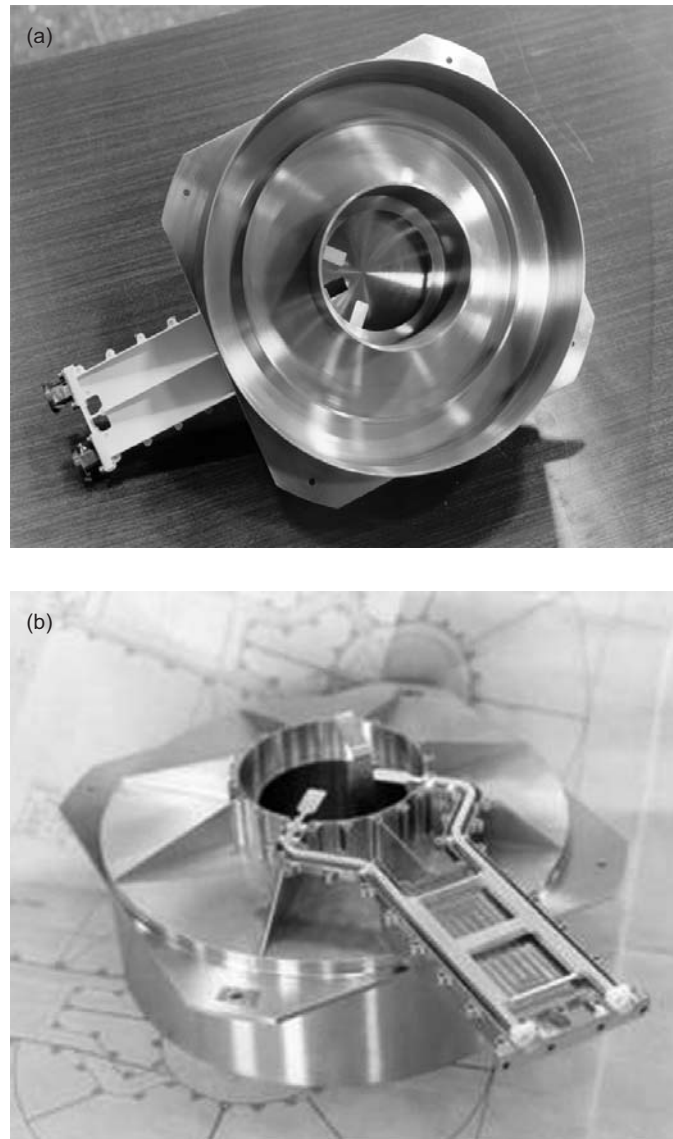
**Fig. 5-51. Cassini S-band feed aperture and feeding network
(a) front view and (b) rear view.**

Measurements of the FM unit showed a peak gain at radio science frequency of 36.3 dBi ±0.3 dB, which corresponds to an overall antenna efficiency of 46.2 percent. At the lowest frequency, the measured peak gain was 35.0 dBi ±0.3 dB (which corresponds to an antenna efficiency of 43.1 percent).
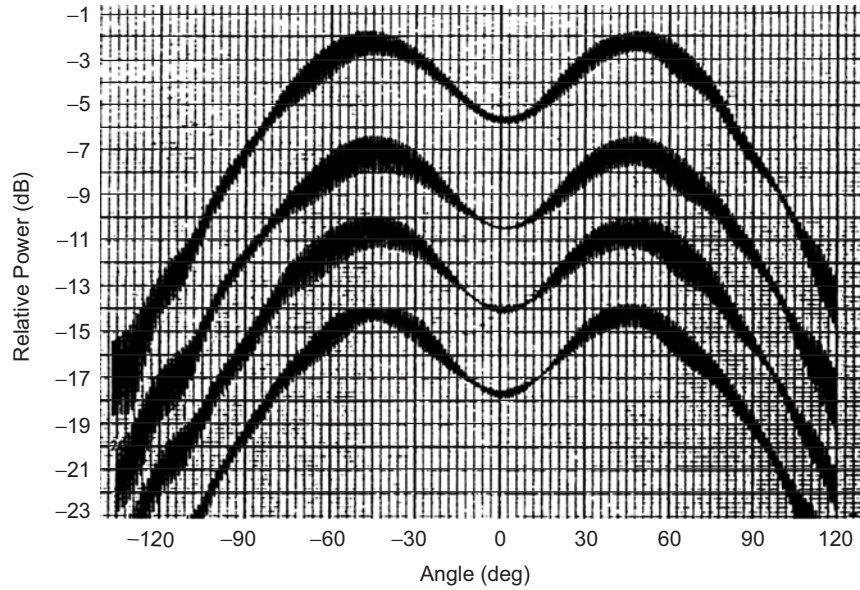
Fig. 5-52. Cassini S-band feed radiation pattern at 2298 MHz
(spinning linear, four Ludwig cuts at 90 deg).

The measured antenna performance on the FM unit at 2.298 GHz (Fig. 5-56(a)) compares well with the computed pattern (Fig. 5-56(b)). Although the 2.04–2.1 GHz spectrum was not so favorable with respect to the science mission (at 2.3 GHz), excellent RF performance in terms of gain and polarization discrimination (>20 dB) have been measured on orbit at this frequency also.

5.3.5 Antenna Performance at X-Band

The requirement for multiple-frequency operation heavily constrained X-band performance, not allowing gain maximization. X-band efficiency was limited by the parabolic main reflector profile in combination with the limited feed aperture of the triple-band feed. Furthermore, a double passage through the Ku-/Ka-front screen occurred on the FSS. It was believed that if the antenna were designed to support only X-band and S-band, as for Voyager, a dual-shaped system in combination with a larger feed aperture would be able to provide a gain improvement on the order of 0.6 dB.

Additionally, a single screen FSS could be implemented in this case, producing a net improvement on the order of 0.4 dB compared with the then-current X-band design, which exhibited an overall gain loss of 0.65 dB at downlink, taking into account the double passage and the (lossy) white paint on the Ku-/Ka-band screen.
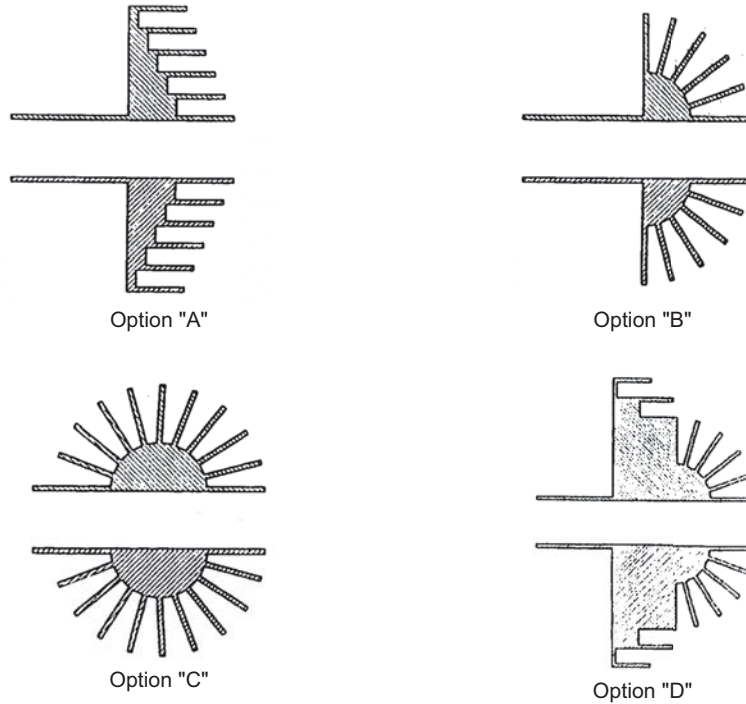
Fig. 5-53. Cassini LGA1 viable layouts.

Measurements of the FM unit showed a peak gain at a downlink frequency of 47.2 dBi ±0.3 dB (which corresponds to an overall antenna efficiency of 42.1 percent). At the uplink frequency, the measured peak gain was 45.3 dBi ±0.3 dB (which corresponds to an antenna efficiency of 37.6 percent).

A very good correlation of the computed antenna patterns with the measured patterns was obtained, as can be seen in Figs. 5-57(a) and (b), which give the experimental performance on ground and the theoretical computations. The EM analysis included an accurate primary field expansion of the triple band feed in the subreflector region, the FSS scattering through the Ku-/Ka-screen, and the blockage effects due to the struts, the feeds in the Cassegrain focal plane, and the FSS deck. A polarization discrimination better than 33 dB was also measured on orbit at the Goldstone tracking station.

5.3.6 Antenna Performance at Ku-Band

The on-axis beam efficiency of the pencil beam (B3) was limited by the integrated triple-band feed design (defocusing and non-optimum taper at subreflector edge caused a peak gain loss of 0.4 dB). Measurements of the FM unit showed a peak gain at center frequency of 50.75 dBi ±0.3 dB (which corresponds to an overall antenna efficiency of 35.6 percent).

Fig. 5-54. Cassini LGA1 engineering breadboard model.

The measured on-orbit antenna performance of the FM unit (Fig. 5-58(a)) compares well with respect to the pattern measured on ground (Fig. 5-58(b)) and the computed (Fig. 5-58(c)), demonstrating the soundness of the thermo-mechanical design.

The design of the SAR beams was based on beam contouring using a focal-fed multifeed system. The secondary pattern synthesis was carried out modeling the spherical wave component of the blockage with a null-field approach, which was then applied to each subarray. Accordingly, the projected shadowing on the antenna aperture was different for each subarray.

In order to obtain an adequate definition of the shadow boundaries, the main reflector aperture was divided into 17,762 elementary patches. The plane-wave component of the struts blockage was considered too.

Software successfully modeled the FSS subreflector as well, at analysis level. In Figs. 5-59 and 5-60, there is remarkable agreement between the measured on-orbit pattern, the measured on-ground pattern, and the computed far-field pattern at the secondary level of the two fan beams. The on-orbit patterns, processed by JPL, were measured using the radiometer mode and scanning the Sun from beyond Jupiter.

The FSS differential insertion loss (with respect to a perfectly reflective surface) is close to 0.5 dB. A peak sidelobe less than 13 dB with respect to MGL was measured on each fan beam, while the integrated sidelobe ratio figures were 8.7 dB (B2/B4), 9.3 dB (B2/B4), and 6.6 dB (B3) respectively.
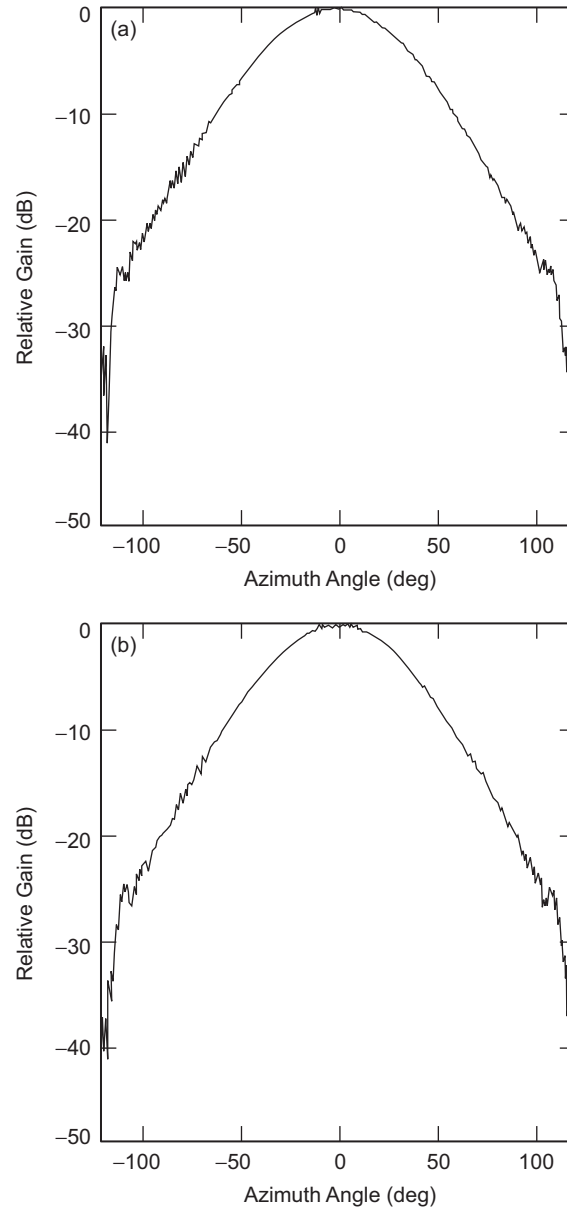
Fig. 5-55. Cassini HGA-LGA1 FM assembly. LGA1 radiation performance at (a) uplink and (b) downlink frequency.
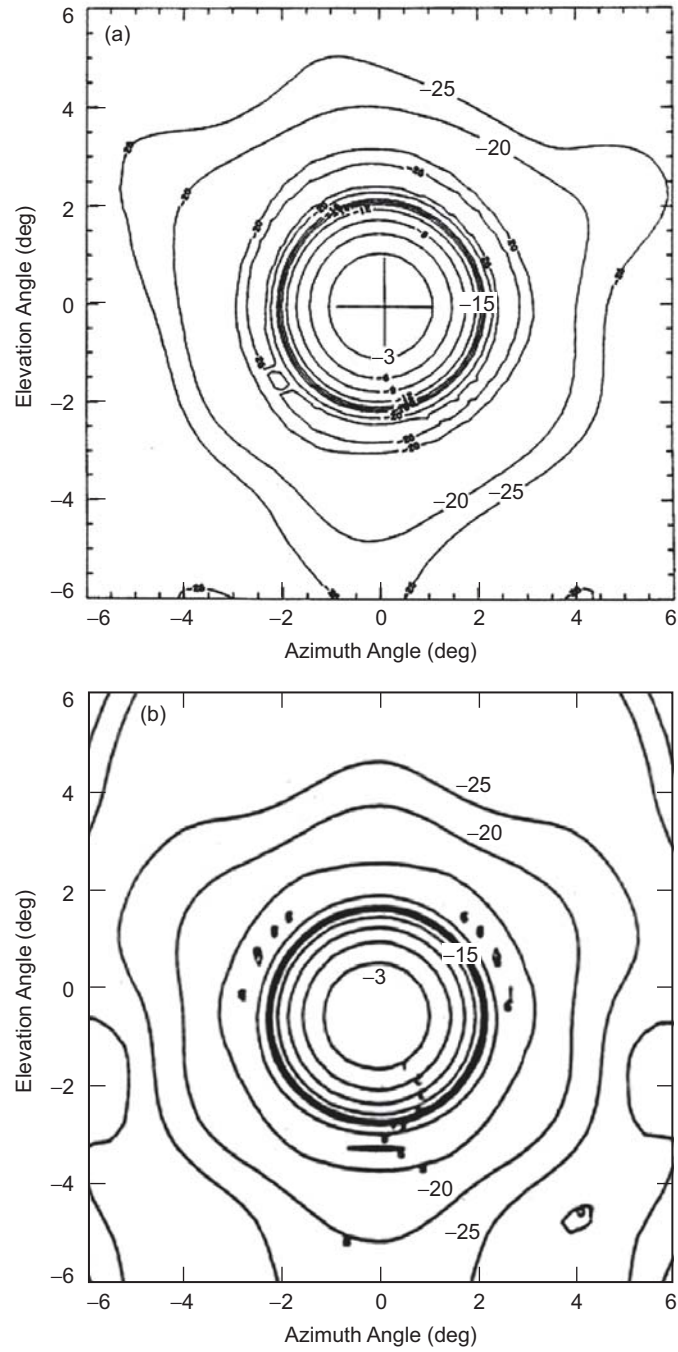
Fig. 5-56.   Cassini HGA-LGA1 FM assembly of S-band radiation performance (F = 2.298 GHz): (a) measured and (b) computed.
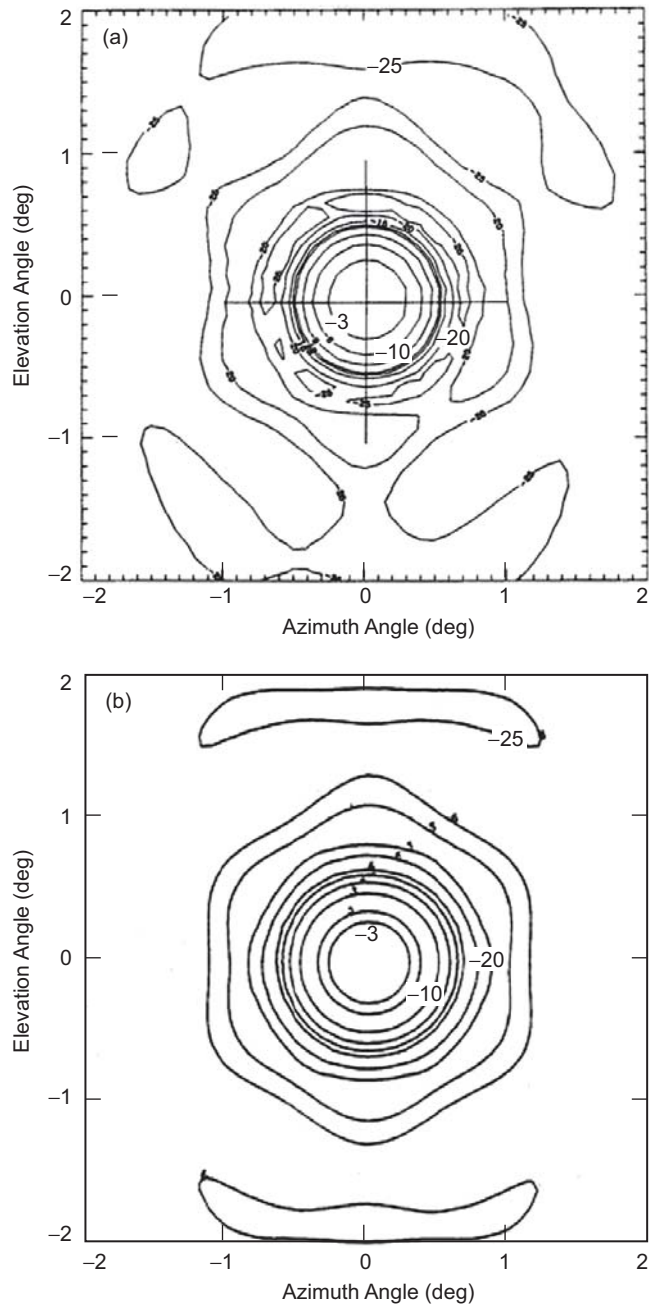
Fig. 5-57. Cassini HGA-LGA1 FM assembly X-band radiation performance (F = 8.425 GHz): (a) measured and (b) computed.
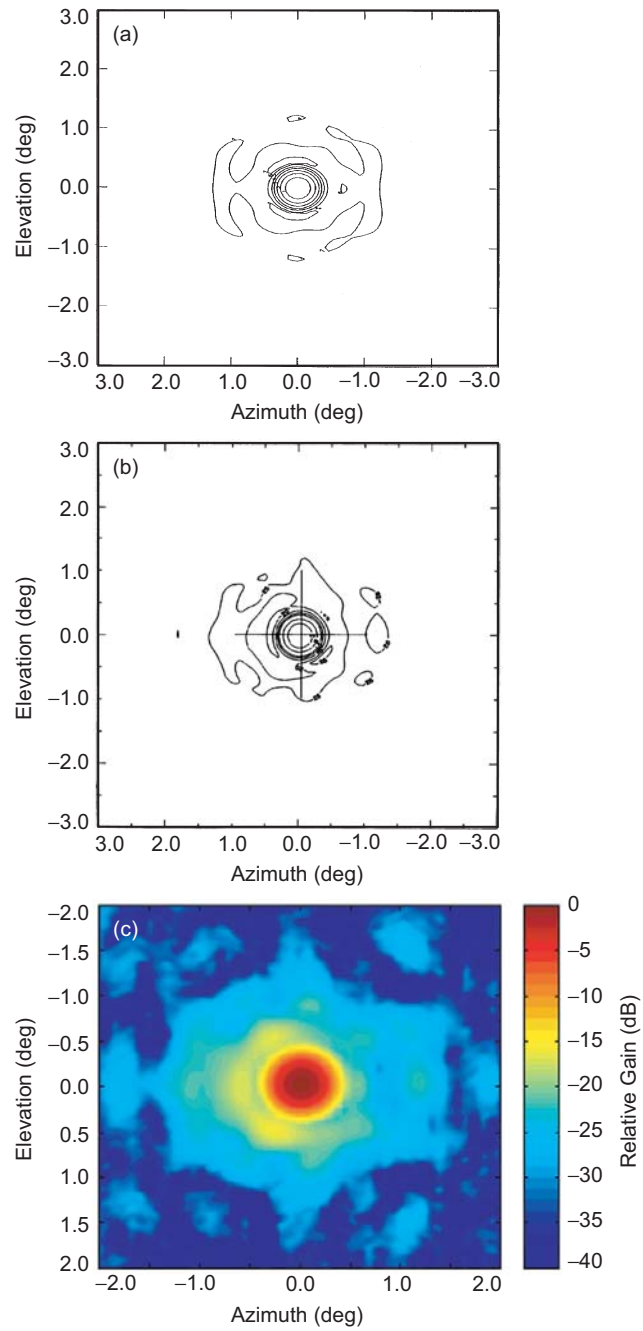
Fig. 5-58. Cassini HGA-LGA1 FM assembly B3 beam Ku-band (B3) radiation performance: (a) computed, (b) measured on ground, and (c) measured on orbit.
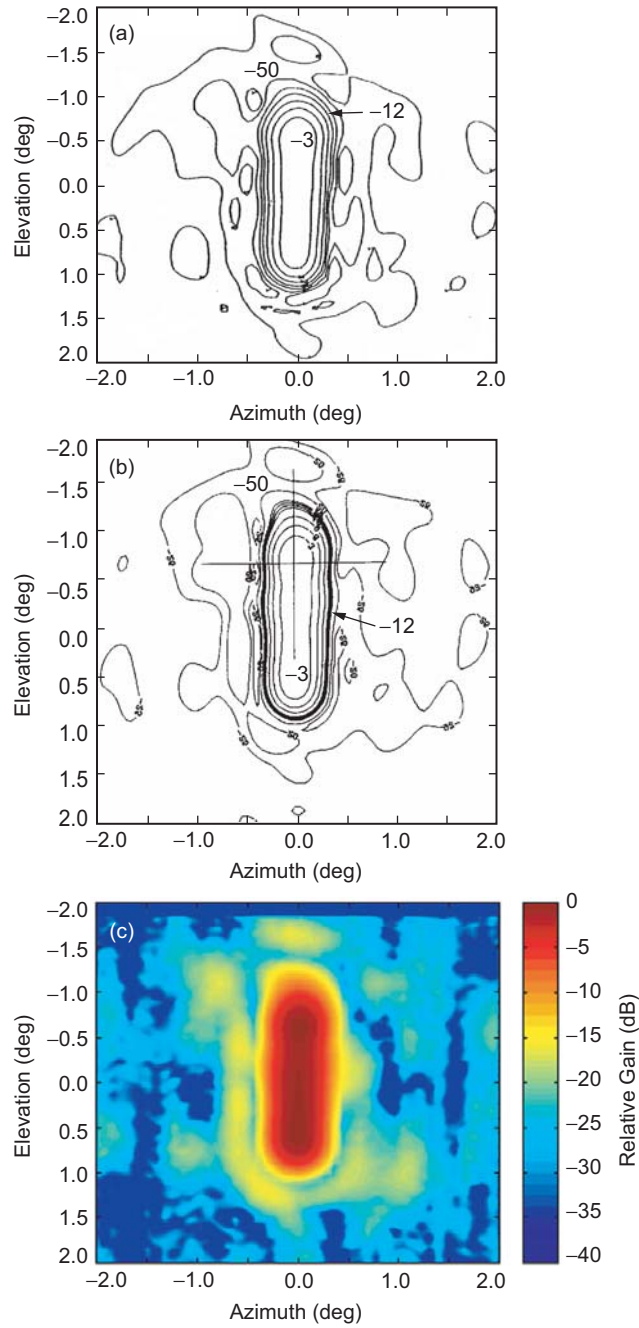
Fig. 5-59. Cassini HGA-LGA1 FM assembly B5 beam Ku-band (B3) radiation performance: (a) computed, (b) measured on ground, and (c) measured on orbit.
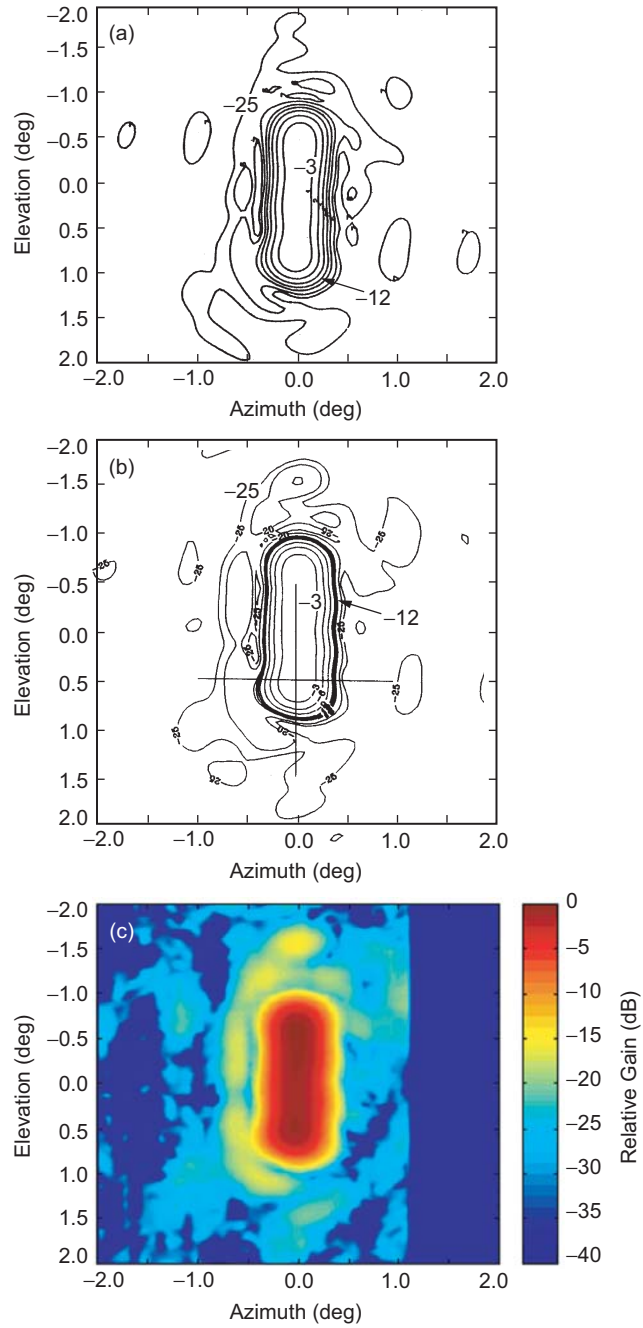
Fig. 5-60. Cassini HGA-LGA1 FM assembly B4 beam Ku-band (B3) radiation performance: (a) computed, (b) measured on ground, and (c) measured on orbit.

5.3.7   Antenna Performance at Ka-Band

Ka-band design was constrained by the parabolic main reflector profile and the hyperbolic subreflector. In the initial design, the beam broadening was achieved by defocusing the feed with respect to the optics phase center. The feed axial position was also limited by the relative interference with the Ku-band feed arrays in the focal plane and the integrated triple-band feed design. A further review of the Ka-band beamwidth requirement occurred on the FM unit, thanks to the improved spacecraft attitude control capability achieved during development. This led to reconsidering a narrower beamwidth of 0.19 deg ±0.02 deg, instead of the nominal 0.23 deg ±0.02 deg. This ultimate beam narrowing, which had a negligible impact on the other bands, was implemented through a slight axial translation of the FSS subreflector.

The final RF performance was successfully modeled (including all the blockage effects, the FSS subreflector, and an accurate reconstruction of the primary field of the triple-band feed in the near field) by means of a spherical-wave harmonics expansion. Figure 5-61 shows a typical agreement between the measured pattern at secondary level and the computed result. To achieve such a correlation, the real main reflector surface was included in the model, based on about two thousand experimental data points measured with an accurate three-dimension (3D) machine.

Figure 5-62 shows the measured downlink pattern of the FM antenna unit after the final subreflector adjustment. The measured peak gain was 56.7 dBi ±0.5 dB; this low antenna efficiency (26 percent) was caused by the desired beam broadening.

5.3.8   Conclusions

The design and performance of the Cassini multifrequency antenna has been presented. Performance estimates were validated by accurate software, able to adequately model such a complex electromagnetic environment.

In particular, modeling was successfully performed for a four-frequency-band FSS subreflector; a complex triple-band feed, and the severe scattering mechanisms due to slot arrays and struts inside the reflector (including additional blocking structures like the FSS deck).

Performance was verified using a full-scale electrical model. The agreement between the computed and the experimental results was satisfactory, confirming the validity of the assumptions. The results on the flight model (FM) unit and the correlation with the on-orbit data, demonstrated full compliance with the requirements and the validity of the electrical and thermo-mechanical design.

To date (October 2005), the Cassini spacecraft is operating superbly. It entered Saturn orbit on July 1, 2004, beginning a four-year tour of the ringed
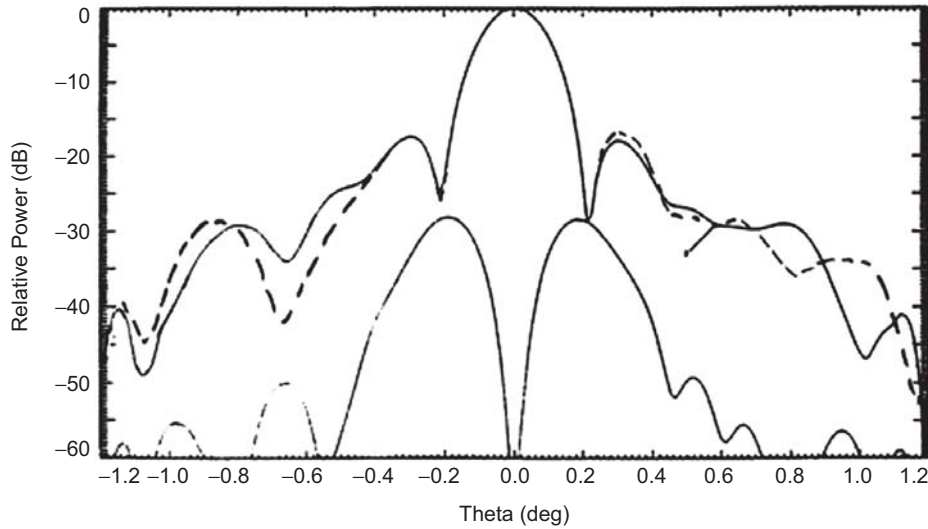
Fig. 5-61. Cassini HGA-LGA1 EBB assembly. Overlay of measured (continuous line) vs. computed (dotted line) Ka-band radiation performance at downlink (32 GHz).

planet, its mysterious moons, stunning rings, and complex magnetic environment. During the tour, Cassini will complete 74 orbits of Saturn, 44 close flybys of the mysterious moon Titan, and numerous flybys of Saturn's other icy moons. Six months after arriving at Saturn, the satellite released its piggybacked Huygens probe for descent through the thick atmosphere of Titan. The probe transmitted data from the surface of Titan.

During the transfer orbit cruise, the antenna subsystem was used several times. In particular, during the two Venus flybys, which occurred in April 1998 and June 1999, the antenna was used as thermal shield for the spacecraft. It reached a temperature of +180 deg C without any failure (in fact, all the RF subsystems operated perfectly).

By combining the multiple-frequency HGA capability with other sophisticated equipment, Cassini began its achievements even before it arrived at Saturn. One important achievement occurred in December 2000, during Cassini's passage close to Jupiter. The scientific community took advantage of Cassini's proximity to the planet by pointing its radiometer towards Jupiter, to measure cosmic synchrotron radiation, which is caused by the high-speed electrons accelerated by the intense magnetic field of the planet. The results were featured in *Nature* [57].

Additionally, Jupiter, our Solar System's most massive planet, was captured in the most detailed global color view ever seen, courtesy of NASA's high-resolution camera. Cassini acquired the views during its closest approach to the gas giant while en route to its final destination.
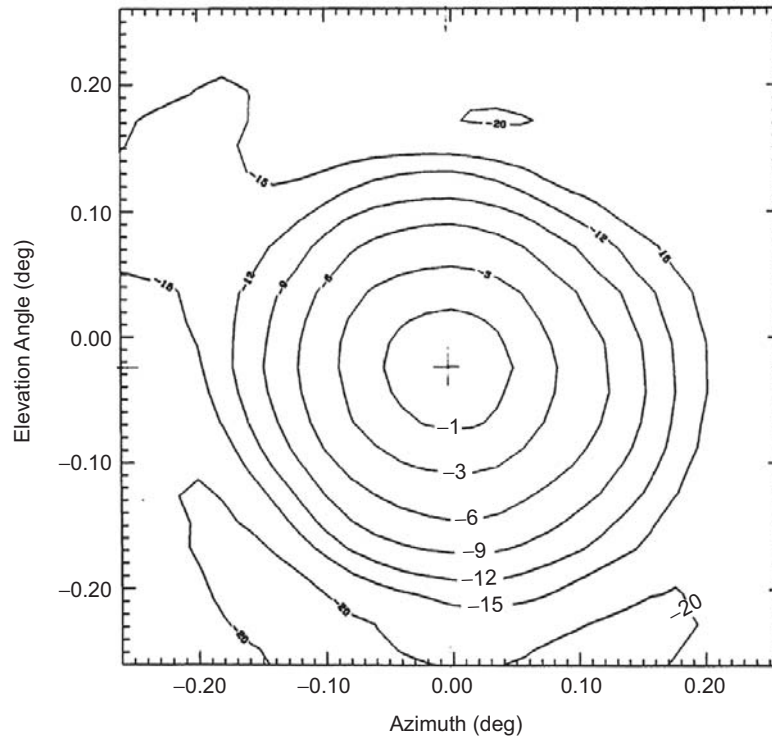
Fig. 5-62. Cassini HGA-LGA1 FM assembly measured Ka-band downlink radiation performance (after ultimate beam narrowing).

Further, a recent experiment by Italian scientists using data from Cassini, confirmed Einstein's theory of general relativity with a precision 50 times greater than that of previous measurements [58]. Past tests of general relativity had confirmed Einstein's prediction to an accuracy of one part per thousand. This accuracy was achieved in 1979 using the Viking landers on Mars. The Cassini experiment confirmed it to an accuracy of 20 parts per million.

The experiment could not have been conducted to this level of accuracy in the past because of noise on the radio link introduced by the solar corona. With the Cassini experiment, this hindrance was overcome by equipping the spacecraft communications system with multiple links at different frequencies. This new capability on the spacecraft and on the 34-m (112-ft.) diameter antenna at Goldstone allowed scientists to remove the effects of the interplanetary and solar plasma from the radio data. In addition, the noise from Earth's atmosphere was strongly reduced by a water vapor radiometer-based calibration system installed at the Goldstone complex.

References

[1]   *Magellan Mission to Venus*, web site at Jet Propulsion Laboratory, Pasadena, California, accessed July 18, 2005.
        http://www2.jpl.nasa.gov/magellan

[2]   "Synthetic Aperture Radar," *Wikipedia* web site, accessed July 18, 2005.
        http://en.wikipedia.org/wiki/Synthetic_aperture_radar

[3]   *Venus Radar Mapper HGA-LGA Incremental Review*, Martin Marietta, Denver, Colorado, October 29, 1985.

[4]   *Venus Radar Mapper Spacecraft Medium Gain Antenna PDR*, VRM-RA-004-014, Martin Marietta, Denver, Colorado, June 1985.

[5]   *Venus Radar Mapper Altimeter Antenna Design Description*, DRD No. SE 014, Hughes Aircraft Company, Los Angeles, California, February 1984.

[6]   J. Taylor, K.-M. Cheung, and D. Seo, *Galileo Telecommunications*, Article 5, The Deep Space Communications and Navigation Systems Center of Excellence (DESCANSO) Design and Performance Summary Series, Jet Propulsion Laboratory, Pasadena, California, July 2002 (also available at web site, accessed July 18, 2005).
        http://descanso.jpl.nasa.gov/DPSummary/Descanso5--Galileo_new.pdf

[7]   A. G. Brejcha and C. A. Smith, "Telemetry Antennas for Deep Space Probes," *Proceedings, ITC/USA, The International Telemetry Conference* (Los Angeles, California, October 18–20, 1977), 77-06-6, p. 9, 1977.

[8]   R. E. Freeland, *Industry Capability for Large Space Antenna Structures*, 710-12 (JPL internal document), Jet Propulsion Laboratory, Pasadena, California, May 25, 1978.

[9]   J. C. Kievit, *Deployable High Gain Antenna Reflector Survey*, JPL D-32835 (JPL internal document), Jet Propulsion Laboratory, Pasadena, California, February 8, 1978.

[10]   C. A. Smith, *Galileo SXA Deployable HGA Technology Industry Visit Summary Report*, JPL D-32836 (JPL internal document), Jet Propulsion Laboratory, Pasadena, California, April 5, 1978.

[11]   W. A. Imbriale, "Phased Arrays for Satellites and the TDRSS Antennas," *Satellite Communication Antenna Technology, Proceedings of the Summer School University of Technology* (Eindhoven, The Netherlands, August 23–27, 1982), R. Mittra, W. A. Imbriale, and E. J. Maanders, editors, Elsevier Science Publishers, North-Holland, Amsterdam, the Netherlands, pp. 431–486, 1983.

[12] G. C. Levanas and M. R. Johnson, *High Gain Antenna Deploy Failure Extended Investigation: Final Report for the Galileo Mission*, JPL D-15345 (internal document), Jet Propulsion Laboratory, Pasadena, California, December 31, 1997

[13] M. R. Johnson, "The Galileo High Gain Antenna Deployment Anomaly," *The 28th Aerospace Mechanisms Symposium* (Lewis Research Center, Cleveland, Ohio), NASA-CP-3260, National Aeronautics and Space Administration, Washington District of Columbia, pp. 359–377, May 1, 1994.

[14] R. Gounley and E. Nilsen, "The Galileo High-Gain Antenna Anomaly: An Overview of the Recovery Efforts," *Third International Symposium on Space Mission Operations and Ground Data Systems* (Greenbelt, Maryland, November 14–18, 1994), Technical Report 94-0227, Jet Propulsion Laboratory, Pasadena, California, 1994.

[15] J. L. Statman, L. J. Deutsch, P. E. Beyer, D. E. Hardi, and R. L. Ticker, "Galileo Telecom Link and its Application to Future Missions," *47th International Astronautical Congress* (Beijing, China, October 7–11, 1996), IAF Paper 96-Q50, International Astronautical Federation, Paris, France.

[16] "Galileo Mission to Jupiter," *NASA Facts*, web page, Jet Propulsion Laboratory, Pasadena, California, accessed September 9, 2005.

http://www.jpl.nasa.gov/news/fact_sheets/galileo0309.pdf

[17] *Galileo Orbiter Functional Requirements Book*, JPL Document 625-205, *Functional Requirement for Galileo Orbiter Flight Equipment S/X-Band Antenna Subsystem*, GLL-4-2017, Rev E (one document in the set of internal documents), Jet Propulsion Laboratory, Pasadena, California, June 9, 1989.

[18] *Design Requirement, Project Galileo Flight Equipment S/X-band Antenna Subsystem*, GLL-2017-1 Rev E (JPL internal document), Jet Propulsion Laboratory, Pasadena, California, July 21, 1981.

[19] M. Gatti, *Galileo HGA Tip Sunshade RF Measurements*, JPL D-32837 (JPL internal document), Jet Propulsion Laboratory, Pasadena, California, December 29, 1987.

[20] Y. Rahmat-Samii, *Gain Loss Estimate for the Galileo High-Gain Antenna with Disconnected Surface Contouring Cords*, JPL D-32838 (JPL internal document), Jet Propulsion Laboratory, Pasadena, California, July 18, 1984

[21] Y. Rahmat-Samii, *Preliminary Estimate for the Effects of 4-cord Removal on the Performance of the Galileo High-Gain Antenna at X-band*, JPL D-32839 (JPL internal document), Jet Propulsion Laboratory, Pasadena, California, August 15, 1984.

[22] Y. Rahmat-Samii and M. Gatti, "Far-Field Patterns of Spaceborne Antennas from Plane-Polar Near-Field Measurements," *IEEE Transactions on Antennas and Propagation*, vol. AP-33, no. 6, pp. 638–648, June 1985.

[23] M. Gatti and Y. Rahmat-Samii, "FFT Applications to Plane-Polar Near-Field Antenna Measurements," *IEEE Transactions on Antennas and Propagation*, vol. AP-36, no. 6, pp. 781–791, June 1988.

[24] D. M. Kerns, *Plane-Wave Scattering-matrix Theory of Antennas and Antenna-Antenna Interactions*, Monograph 162, U.S. Department of Commerce/National Bureau of Standards, June 1981.

[25] Y. Rahmat-Samii, V. Galindo-Israel, and R. Mittra, "A Plane-Polar Approach for Far-Field Construction from Near-Field Measurements," *IEEE Transactions on Antennas and Propagation*, vol. AP-28, pp. 216–230, March 1980.

[26] M. Gatti, *Post-Environmental Test Results of the Galileo SXA S/N 002*, JPL D-32840 (JPL internal document), Jet Propulsion Laboratory, Pasadena, California, August 14, 1985.

[27] M. Gatti, *Galileo LGA Far Field Testing–S/N 002*, JPL D-32841 (JPL internal document), Jet Propulsion Laboratory, Pasadena, California, August 30, 1985.

[28] M. S. Gatti and D. J. Nybakken, "A Circularly Polarized Crossed Drooping Dipole Antenna," *Proceedings of the Joint Antennas and Propagation and Microwave Theory and Techniques International Symposium, and URSI Radio Science Meeting,* IEEE, pp. 254–257, May 7–11, 1990.

[29] H. Jasik, *Antenna Engineering Handbook*, First Ed., McGraw-Hill, New York, New York, pp. 31-23 to 31-25, 1961.

[30] M. Gatti, *LGA2 Engineering Model Test Data*, JPL D-32842 (JPL internal document), Jet Propulsion Laboratory, Pasadena, California, November 2, 1987.

[31] M. Gatti, *LGA2 Engineering Model Test Data–Uplink Frequency 2115 MHz*, JPL D-32843 (JPL internal document), Jet Propulsion Laboratory, Pasadena, California, January 27, 1988.

[32] "Galileo End of Mission Status," web page, Jet propulsion Laboratory, Pasadena, California, September 17, 2003, site accessed August 30, 2005. http://www2.jpl.nasa.gov.galileo/news/release/press030921.html

[33] E. H. Maize, "The Cassini-Huygens Mission to Saturn and Titan," *Space Technology and Applications International Forum—STAIF 2005*, vol. AIP Conference Proceedings 746, American Institute of Physics, Melville, New York, pp. 223–231, 2005.

[34] R. Mizzoni, "The Cassini High Gain Antenna (HGA): A Survey on Electrical Requirements, Design and Performance," *IEE Seminar on Spacecraft Antennas*, Institution of Electrical Engineers, London, England, pp. 6/1–6/10, May 9, 1994.

[35] V. Galindo, "Design of Dual Reflector Antenna with Arbitrary Phase and Amplitude Distribution," *IEEE Transactions on Antennas and Propagation*, vol. AP-12, p. 403, 1964.

[36] W. F. Williams, "High Efficiency Antenna Reflector," *Microwave Journal*, vol. 8, no. 7 p. 79, 1965.

[37] P. J. Wood, "Reflector Profiles for Pencil Beam Cassegrain Antenna," *Marconi Review*, vol. 34, no. 182, p. 121, 1972.

[38] Y. Rahmat-Samii, "Subreflector Extension for Improved Efficiencies in Cassegrain Antenna GTD/PO Analysis," *IEEE Transactions on Antennas and Propagation*, vol. AP-34, p. 1266, 1986.

[39] P. J. Wood, *Reflector Antenna Analysis and Design*, 1980, Peter Peregrims LTD, London, England.

[40] P. J. B. Clarricoats and G. T. Poulton, "High-Efficiency Microwave Reflector Antennas–A Review," *Proceeding of the IEEE*, vol. 65, no. 10, pp. 1470–1504, October 1977.

[41] D.-W. Duan, Y. Rahmat-Samii, "A Generalized Diffraction Synthesis Technique for High Performance Reflector Antennas," *IEEE Transactions on Antennas and Propagation*, vol. 43, pp. 27–40, January 1995.

[42] HGA R.F. Team (approved by R. Mizzoni), HGA-LGA1 *Electrical Design Report, Cassini Program*, Alenia Spazio, Rome, Italy, May 7, 1995.

[43] W. V. T. Rush, O. Sorensen, and J. W. M. Baars, "Radiation Cones from Feed-Support Struts of Symmetrical Paraboloidal Antenna," *IEEE Transactions on Antennas and Propagation*, vol. AP-30, no. 4, pp. 786–790, 1982.

[44] Y. C. Chang, H. V. Morrison, and R. C. Rudduck "A Hybrid Approach for the Strut Analysis of Reflector Antennas," *1986 IEEE AP-S Symposium*, Philadelphia, Pennsylvania, pp. 523–526, 1986.

[45]   S. Maci, R. Mizzoni, E. Pelaca, R. Tiberio, and A. Toccafondi, "An Investigation on Blockage Effects in the Multiband Reflector Antenna for Cassini Spacecraft," *3rd ESA European Workshop* (Pisa, Italy), October 26–28, 1993.

[46]   A. Toccafondi, B. Romani, R. Mizzoni, S. Maci, and R. Tiberio, "Spherical Wave Blockage in Reflector Antennas," *IEEE Transactions on Antennas and Propagation*, vol. 45, no. 5, pp. 851–857, May 1997.

[47]   D. Bresciani and S. Contu, "Scattering Analysis of Dichroic Sub-Reflectors," *Electromagnetics*, vol. 5, no. 4, pp. 375–407, 1985.

[48]   D. Bresciani, "A Unified Approach to the Characterization of Frequency and Polarization Selective Surfaces," *Proceedings of the IEEE-AP Symposium*, Ann Arbor, Michigan, pp. 1960–1963, 1993.

[49]   G. Mascolo, S. Contu, R. Mizzoni, and S. Borchi, "A Double Dichroic Sub-Reflector Reflective at X, Ku, Ka Bands and Transparent at S-Band," *8 Journèes Internationales de Nice sur les Antennes Jina 94*, November 8–10 Nice, France, 1994.

[50]   C. Bruno, S. Contu, D. Marzi, and G. Mascolo, "Design, Manufacturing and Testing of a Ku/Ka Dichroic Sub-Reflector for Space Communications," *Antennas and Propagation, Proceedings of the 8th International Conference on Antenna and Propagation* (Edinburgh, United Kingdom), Oxford University Press, Oxford, United Kingdom, pp. 178–181, March 1993.

[51]   G. Mascolo and R. Flamini, "Dielectric Constant Measurements of Dielectric Substrates at Cryogenic Temperatures," *Antennas and Propagation Society International Symposium 1995 Digest* (June 1995, Newport Beach, California), vol. 4, pp. 1848–1851, 1995.

[52]   K. Mahadevan, S. Ghosh, R. Mizzoni, and G. Martirano "Precision Analysis and Design of a Triple Band Feed for the High Gain Antenna of Cassini Deep Space Mission to Saturn," to appear in *JINA 94*, November 8–10, 2005, Nice, France.

[53]   G. Martirano, R. Mizzoni, M. Lori, and A. Spizzichino, "The Ku-Band sub-System of the Cassini High Gain Antenna (HGA)," presented at *Progress in Electromagnetic Research (PIERS 94)*, Noordwijk, Netherlands, July 11–15, 1994.

[54]   N. C. Albertsen, *Electromagnetic Modelling for Multi-Beam Slotted Waveguide Array Antennas, Final Report*, Ticra Report S-498-02, Ticra Engineering Consultants, Copenhagen, Denmark, 1992.

[55]   F. Alessandri, G. Bartolucci, and R. Sorrentino, "Admittance-Matrix Formulation of Waveguide Discontinuity Problems, Application to the

Design of Branch-Guide Couplers," *IEEE Transactions on Microwave Theory and Techniques*, vol. MTT-36, pp. 394–403, February 1988.

[56] G. F. Koch, "Coaxial Feeds for High Aperture Efficiency and Low Spillover of Paraboloidal Reflector Antennas," *IEEE Transactions on Antennas and Propagation*, AP-21 no. 2, pp. 164–169, March 1973.

[57] T. W. Hill, "Magnetic Moments at Jupiter," *Nature*, vol. 415, no. 6875, pp. 965–966, February 28, 2002.

[58] B. Bertotti, L. Less, and P. Tortora, "A Test of General Relativity Using Radio Links with the Cassini Spacecraft," *Nature*, vol. 25, no. 6956, pp. 374–376, September 25, 2003.